InSAR Detection of Ground Deformation in Megalopolises of Pearl River Delta

ZHAO, Qing

A Thesis Submitted in Partial Fulfillment of the Requirements for the Degree of Doctor of Philosophy in Geoinformation Science

The Chinese University of Hong Kong

May 2010

ProQuest LLC
789 East Eisenhower Parkway
P.O. Box 1346
Ann Arbor, MI 48106-1346

Thesis Committee

Professor FUNG, Tung (Chair)

Professor LIN, Hui (Thesis Supervisor)

Professor ZHANG, Yuanzhi (Co-supervisor)

Professor CHIU, Longsang (Committee Member)

Professor GE, Linlin (External Examiner)

论文评审委员会

冯通 教授 （主席）

林珲 教授 （论文导师）

张渊智 教授 （论文导师）

赵朗生 教授（委员）

葛林林 教授 （校外委员）

ACKNOWLEDGEMENTS

The research is supported by the scholarship of the Chinese University of Hong Kong for Ph.D. student.

Firstly, I would like to express my thanks to my supervisors, Professor LIN Hui, for his instructive guidance, kind criticism and tireless encouragement. Particularly, I appreciate his support and encouragement to initiate my own views in this dissertation and keep going to finish this work. Without his devoted supervision, the completion of this work could not be achieved.

I am also grateful to my co-supervisor, Professor ZHANG Yuanzhi, for his kind support and help when I went to Guangzhou for field investigation. Particularly, I appreciate Professor Howard A. ZEBKER, my advisor when I visit Stanford University as an exchange student, for his instructive comments and suggestions that improved my paper a lot.

I would also like to express my gratitude by heart to Professor ZHENG Quanan, Senior research scientist of Maryland University. His lectures and publications about microwave remote sensing taught me a lot. I not only learnt his knowledge, but also research ideas and methods. His lectures expanded my horizon and lit my scientific inspiration.

I also owe special thank to Professor Daniele PERISSIN, his instructive

suggestions and comments improved my research work a lot. I learnt a lot from our discussions.

During my study, I have been fortunate to receive enormous help from professors in Institute of Space and Earth Information Science and Department of Geography. My deep appreciation goes to Professors CHIU Long Sang, PAN Jiayi, FUNG Tung, for their valuable suggestions on my research and kind help. There are too many friends at CUHK to thank individually for their friendship, support and help. They are Dr. CHEN Fulong, Dr. HU Mingyuan, GAO Si, HU Xianzhi, HU Ya, WANG Shengxiao, HU Haiju, ZHU Qinqin, JIANG Lu, ZHANG Qian, WANG Guiwu, LIU Biao, XI Hongyan, CHENG Shilai, GU Yanzhen, SUN Yujuan, and WU Lei. I would also like to thank supporting staffs in our institute for their kind help. They are YIP Chloris, WONG Wendy, YEUNG Kin, WONG Anthony, SUEN Eric, CHAN Isaac, CHAO Ming Chun, and HE Jie.

I also owe a particular debt of gratitude to my thesis oral defence committee members: Prof. LIN Hui and Prof. ZHANG Yuanzhi; Prof. FUNG Tung; Prof. CHIU Longsang, and Prof. GE Linlin.

Last but not least, I would like to express heartfelt appreciation of my family full support. I am grateful to my father and husband for supporting my seemingly endless education, sharing in my struggles and successes, and encouraging me all the way.

ABSTRACT

of thesis entitled:

InSAR Detection of Ground Deformation in Megalopolises of Pearl River Delta

Submitted by ZHAO, Qing

For the degree of Doctor of Philosophy

at The Chinese University of Hong Kong

in May 2010

Megalopolises in the Pearl River Delta, including Guangzhou and Hong Kong, have experienced various degree of ground subsidence. The causes can be divided

into two categories: natural subsidence and the human-induced subsidence. Monitoring the ground subsidence can not only help people to find out the distributions in both spatial and temporal fields, but also guide people to minimize the hazard ahead. Thus, it is significant to monitor the ground subsidence accurately, timely and frequently. This dissertation research uses the Environmental Satellite Advanced Synthetic Aperture Radar (ENVISAT ASAR) data received at the Chinese University of Hong Kong Satellite Remote Sensing Receiving Station and SAR Interferometry (InSAR) technology as a powerful tool for large-scale ground deformation monitoring in Guangzhou and Hong Kong areas.

Persistent Scatterer Interferometry (PSI) method is used to detect ground deformation in the urban area of Guangzhou city. A ground deformation rate map with scattered distribution of point targets shows the maximum subsidence (rise) rate as high as -26 to -20 mma^{-1} (16–21 mma^{-1}), implying that the study area is an active zone for ground deformation. Based on the point target map, a contour ground deformation rate map is generated. All the six ground collapse accidents that occurred in 2007–2008 fall within the subsidence zones, qualitatively validating the IPTA results. Ground subsidence and geological conditions on Datansha Island are examined. The results indicate that the local geological conditions and underground engineering projects are responsible for ground subsidence and ground collapse accidents occurred there. To interpret the distribution of active ground subsidence zones, a local geological map is used as a reference for generating a series of thematic

maps. The results show that geological faults, rock distribution, over-development, and underground engineering projects may be four factors leading to the distribution of the active ground subsidence zones.

The Hong Kong International Airport (HKIA) was built on a site of 12.5 km^2, of which 75% is reclaimed foundation. Thus, the stability of ground foundation of HKIA is of public concern. I use the PSI method and ENVISAT ASAR data to detect the residual settlement rate from 19 April 2006 to 9 January 2008. I use ground truth data to develop empirical correction models for correcting systematic biases in the ASAR PSI-detected settlement rate. The corrected data follow the Lorentz distribution well, implying that the residual settlement process is dominated by two modes or categories of settlement rates. I find unreasonable positive values of the ASAR PSI-detected annual ground settlement rate, which follow a normal distribution. I draw a scatter plot with ground deformation rate value and coherence value of each point targets. Point targets with lower coherence values and greater positive values are extracted and drawn on a geographical map. Most of these point targets are located at the airport Midfield, which is under construction. A ground settlement rate map of HKIA shows that an area of the Passenger Terminal Building, and an area of the Southern Runway are two relatively stable areas, and one major continuous settlement area covers the airport Midfield. General spatial distribution patterns of ASAR PSI-detected ground settlement rate agree well with model-predicted residual settlement rates.

摘要

地处珠江三角洲的特大城市，例如广州和香港，正在经受不同程度的地面沉降。地面沉降不仅会威胁地表建筑物的稳定，还会严重影响地下工程、设施和城市地下管线的安全。导致地面沉降的原因可以归为两大类：自然沉降和人为因素导致的地面沉降。地面沉降监测不仅有助于及时掌握地面沉降的时间和空间分布规律，也能够为最大限度减少沉降造成的损失给予必要的指导。因此，准确、及时、定期地监测地面沉降是非常必要的。本论文以广州和香港城市地区为研究区域，应用高级雷达干涉测量技术和香港中文大学卫星地面接收站接收的ENVISAR ASAR 数据，监测两个研究区域的地表形变现状。

永久散射体干涉测量技术，作为一种最先进的雷达干涉测量技术，被应用于广州市区的地表形变监测。我得到了主城区的地表形变场图和地表形变等值线图。结合广州市区地质构造图，绘制出广州市活动地表沉降带专题图。并以大坦沙岛为例，结合地质图，分析并解译大坦沙岛附近地表沉降带的分布特征和成因。通过解译广州市活动地表沉降带专题图以及野外调研，认识到区域地质断裂构造、不同沉积物分布边界、城市过度开发以及地下工程可能是造成广州市活动地表沉降带的主要原因。

香港国际机场 75%的面积为填海而成，因此香港国际机场的地表稳定备受公众的关注。应用永久散射体干涉测量技术和 ENVISAT ASAR 来监测香港国际机场的 2006 年至 2008 年期间的地表形变量。并用香港国际机场提供的地面测量

数据验证了此结果。发现永久散射体干涉测量技术得到的地表形变结果存在系统偏差。为去除这一系统偏差，我开发了经验改正模型。经过经验改正模型改正后的地表形变速率值分布图符合洛仑兹分布。在去除系统偏差后，仍有抬升值存在。通过绘制形变速率值和相干值之间的散点图，并把具有低相干值和形变速率为抬升值的点绘制在地理图上，发现大部分此类点分布在机场中部空地。而机场空地正在修建第二座机场候机楼。绘制出的香港国际机场形变图显示：机场候机大楼和南跑道是两个相对稳定的区域，沉降区主要集中在机场中部空地区。通过与机场填海初期创建的沉降模型得到的沉降图比较，用永久散射体干涉测量技术和ASAR 数据得到的地表形变图与其吻合得很好。

Table of Content

List of Figures

List of Tables

Chapter 1. Introduction

1.1 Research background

The minute changes in the Earth crustal may have caused great impacts on the living conditions for human beings, and threaten life and property (*Jónsson, 2002*). The crustal movement of several decimeters may cause a disaster earthquake. Even a ground subsidence with a rate of 1 cma^{-1} may cause serious damages to the buildings, harbors, underground facilities, and transportation facilities, such as roads, rail lines, tunnels, port facilities, and airport runways. Thus, detecting the Earth crustal deformation, and clarifying its fundamental laws are everlasting research topics for the human pursuits.

Ground deformation can be caused by solid earth hazards and human being activities. The solid earth hazards include earthquakes, volcanic eruptions, landslides, and other types of ground instability (*Jónsson, 2002*). The human being activities are over-pumping underground water, gas, and oil, mining, and underground projects

(*Poland, 1984; He, et al., 2006*).

Previous investigators have pointed out that the ground subsidence is a major geological hazard in the cities of China (*He, et al., 2006, The Ministry of Land and Resources, 2007*). The causes of this hazard are quite complicated. The ground subsidence in China can be classified into the following three types of geographic regions (*Hu, et al., 2004*):

The coastal plain and river delta regions, such as Tianjin, Shanghai, Guangzhou, Hong Kong;

The plain regions in front of major mountains, such as the North China Plain and Songliao Plain; Regions in valleys and basins among mountains, such as Xi'an and Taiyuan.

At present, China has 96 cities and municipalities where disastrous ground subsidence has occurred or is occurring (*He, et al., 2006*). 80% of the cities and municipalities are located in the eastern of China (*He, et al., 2006*). The total subsidence area is over $7*10^4$ km^2 (*Xue, et al., 2006*). The maximum accumulative subsidence value has reached to 3 m (*Xue, et al., 2006*). It is roughly estimated that the economic loss due to ground subsidence in Yangtze River Delta is about ¥3500 billion (*Zhang, et al., 2005*). Up to 2002, more than 11 cities have had the accumulative subsidence greater than 1 m at their subsidence centers (*Hu, et al., 2004*). These cities include Shanghai, Tianjin, Suzhou, Wuxi, Changzhou, Cangzhou, Xian, Fuyang, Taiyuan, An' yang, and Taipei.

Previous investigators have pointed out that coastal megacities in China, including Shanghai, Guangzhou and Hong Kong, have experienced various degree of ground subsidence. The natural subsidence includes deformation of soft soil, and Karst geomorphologic collapse, while the human-induced subsidence results from land reclamation, over-pumping underground water, underground mining, and concentrated construction. The ground subsidence occurred in cities in southern China is strongly associated with the rapid development of industrialization and urbanization.

1.2 Research questions

Monitoring the ground subsidence can not only help people find out the distributions in both spatial and temporal field, but also guide people minimize the hazard ahead. So it is very essential to monitor the ground subsidence accurately, timely and frequently.

Leveling surveying, Global Position System (GPS), and other so-called point-based methods have often been used to monitor the ground subsidence. These methods can only measure limited number of points, and they are manpower intensive, costly and time consuming. Especially, if the ground subsidence is of large-scale, it is impossible for these traditional methods to monitor the disaster.

Satellite synthetic aperture radar (SAR) interferometry (InSAR) is potentially a powerful tool for large-scale ground deformation monitoring. The InSAR technologies have been used to detect terrain deformation with a millimetric accuracy. However,

temporal and geometrical decorrelation and atomospheric inhomogeneities make InSAR measurements unfeasible over large areas where the signals decorrelate, limit the number of image pairs suitable for interfeometric applications, prevent one from fully exploiting the data set available, and degrade InSAR measurement accuracy.

Persistent Scatterer Interferometry (PSI) is a development of the conventional InSAR technologies. An algorithm to exploit PS pixels was first achieved by Ferretti et al. (*Ferretti, et al., 2000; Ferretti, et al., 2001*). The primary aim of development of this algorithm is to overcome the limitation of temporal and geometrical de-correlation of InSAR, which prevents the technologies from being an operational tool in practice. The spatial density of PS is much higher than the grids that are generated by the traditional point-based methods, such as leveling surveying and Global Positioning System (GPS) technology. In particular in the urban areas, the PS density may reach as high as 100 PS km^{-2}. The accuracy of deformation measurements may be raised to 0.1-1 mma^{-1} on an averaged line-of-sight deformation rate, and 1-3.5 mm on a single measurement. This implies that the PSI technology can be used as an operational tool to measure ground deformation with a high accuracy and a high spatial PS grid density. The algorithm has been patented and named as "permanent scatterers technique". Similar processing algorithms have since been developed by Crosetto et al. (*Crosetto, et al., 2003; Crosetto, et al., 2003*), Lyons and Sandwell (*Lyons and Sandwell, 2003*), Werner et al. (*Werner et al., 2003)*, Kampes (*Kampes, 2005)* and Hooper (*Hooper, et al., 2004*). These methods have been very successful for InSAR analysis of radar scenes containing large numbers

of man-made structures, which tend to be angular and often produce very efficient reflectors that dominate background scattering (*Hooper, et al., 2004*).

Although the PSI technologies offer a way to reduce the main limitations in conventional InSAR methods, there are still several disadvantages in this technology. First, the technology needs as many SAR images as possible to analyze the ground deformation history. Thus it is impossible to apply this technology in the areas where there are not enough archived SAR images available. Second, although the PS density in urban areas can be very high (>100 $PSkm^{-2}$), still not all buildings can be monitored by means of this technology. Third, the PSI is not suitable for monitoring the areas that are densely vegetated because of too low PS density.

In this dissertation, the following scientific questions are studied and answered.

What is the current status of ground subsidence in the urban area of Guangzhou city? What are the distribution characteristics of ground collapse accidents occurred in Guangzhou urban area during 2007–2009? What are the mechanisms for causing the ground subsidence in Guangzhou urban area?

What is the current status of ground settlement at Hong Kong International Airport (HKIA)? What are the mechanisms and laws of ground settlement at HKIA? What are the statistic distribution characteristic of ground deformation rate dataset generated by PSI?

1.3 Research objectives

The purpose of this research is to use PSI technology and SAR images to detect ground deformation in the urban area of Guangzhou city and Hong Kong International Airport. The primary research objectives of this research are to:

1) Generate ground deformation maps in the urban area of Guangzhou city, and Hong Kong International Airport with PSI;

2) Through field work, validate ground deformation results with ground truth data;

3) Analyze the validated PSI results in detail;

4) Investigate the mechanisms for causing the ground deformation in Guanghzou urban area and Hong Kong International Airport.

1.4 Thesis framework and contributions

The main goal of this research is to apply the PSI technology to measure and monitor the ground stability of the Mega-cities of the Pearl River Delta Region, and to interpret the PSI derived results. In order to achieve this goal, a general understanding of Synthetic Aperture Radar (SAR), Synthetic Aperture Radar Interferometry (InSAR), PSI, and error sources and analysis in Radar Interferometry is foundational to this research. The Advanced Synthetic Aperture Radar (ASAR) images of Guangzhou and Hong Kong International Airport used in this study are acquired and pre-processed. In addition,

geological maps, ground truth data (or field observed ground deformation information), and field investigation materials are all collected. Guangzhou and Hong Kong International Airport are taken as two case study areas. The ASAR PSI derived results of the two study areas are field investigated and validated. A great value filter method, an empirical systematic biases correction model, and statistical analysis method are developed for the applications of PSI. The ASAR PSI results are further analyzed and interpreted using the geological maps, field investigation materials, and ground truth data.

I summarize the main contributions of this dissertation research as below.

First, I generate a ground deformation rate map of Guangzhou urban area with scattered distribution of point targets with ASAR images acquired in 2007–2008. The maximum subsidence rate reaches up to -26 to -20 mma^{-1}.

Second, based on the point target map, a contour ground deformation rate map of Guangzhou urban area is generated by an interpolation method. The contour map shows three major subsidence zones located in the middle-west, the east, and the southwest of the study area, respectively. All the sites of six ground collapse accidents that occurred in 2007–2008 fall within the subsidence areas, qualitatively validating the PSI results.

Third, ground subsidence and geological conditions along metro-lines in Datansha Island are examined as a case study.

Fourth, I generate a thematic map of active ground subsidence zones of urban area

of Guangzhou city. In order to analyze the causes of the active ground subsidence, a local geological map including geological structure, sediments, and rocks information are collected. The geological faults, the spatial distribution of sediment characteristics, over-development, and underground engineering projects are considered as four major factors for active ground subsidence zones. I did field investigations for validation.

Fifth, I generate a ground deformation rate map of Hong Kong international airport. I also validate the result with near-simultaneously leveling datasets.

Sixth, I develop an empirical systematic biases correction model to correct the systematic biases in the ASAR PSI results of Hong Kong International Airport.

Seventh, I find the statistic distribution of unreasonable positive values of ASAR PSI detected annual ground settlement rate of Hong Kong International Airport follows a normal distribution. Most of these point targets are located at the airport Midfield which is under construction.

Eighth, I generate a map of ASAR PSI-detected residual settlement rate of Hong Kong International Airport, and find that it agrees well with the model-predicted settlement rate patterns.

1.5 Thesis structure

Chapter 2 provides a brief overview of InSAR and existing persistent scatterer InSAR methods.

Chapter 3 contains descriptions of preprocessing the ASAR data used in this study.

Chapters 4 to 7 of this dissertation are prepared based on the manuscripts that have already been published in scientific journals, written or are in preparation for submission to journals. For each associated manuscript there are multiple authors, however, the author of this dissertation is the primary researcher and author in each case.

Chapter 4 describes the development of InSAR application technologies. It includes calibration and validation of InSAR derived ground deformation rate, statistical analysis of InSAR-derived ground deformation rates, great value filter method, and analysis of 2-D distribution characteristics of InSAR derived ground deformation rate. This Chapter is based on material published in Sensors, IEEE TGRS, and 2009 Joint Urban Remote Sensing Event (*Zhao et al., 2009a; Zhao et al., 2009b; Zhao et al., 2009c*).

Chapter 5 describes the application of PSI for ground deformation measuring in urban area of Guangzhou city. A time series of ENVISAT ASAR images, taken from 19 March 2007 to 12 May 2008, are used to generate ground deformation fields and interpretation maps in the study area. The derived ground subsidence data are then compared with reported ground observation results and analyzed in detail. This chapter was published in Sensors. Chapter 6 analyzes the mechanisms for causing the ground subsidence in Guangzhou urban area. This chapter was published 2009 Joint Urban Remote Sensing Event.

Chapter 7 investigates residual settlement of the reclaimed foundation at Hong

Kong International Airport. I use ENVISAR ASAR images acquired from 19 April 2006 to 9 January 2008 to generate a ground settlement rate map of the airport. The ASAR PSI-detected ground settlement rates are comparable with the ground truth data, but there are systematic biases. I correct the systematic biases in the ASAR PSI results using empirical correction models. The map of ASAR PSI-detected residual settlement rate of HKIA agrees with the model-predicted settlement rate patterns.

Chapter 8 provides a summary of the thesis and suggestions for future work.

Chapter 2. Literature Review

2.1 Synthetic Aperture Radar (SAR)

Synthetic Aperture Radar (SAR) systems have been used extensively in the past two decades for fine resolution mapping and other remote sensing applications (*Curlander and McDonough, 1991; Rosen, et al., 2000; Kovaly, 1976; Elachi, 1988*) As an active microwave sensor, SAR is capable of continuously monitoring geophysical parameters related to the structural and electrical properties of the earth's surface (and its subsurface) (*Curlander and McDonough, 1991*). As an active system, the SAR provides its own illumination and operation. Furthermore, neither clouds, fog, nor precipitation have a significant effect on microwaves, thus permitting all-weather imaging (*Curlander and McDonough, 1991*). Furthermore, SAR system is capable of achieving a resolution independent of the sensor altitude. This characteristic makes the SAR an extremely valuable instrument for space observation (*Curlander and McDonough, 1991*).

2.1.1 History of Synthetic Aperture Radar

The early versions of side-looking aperture radar (SLAR) systems were primarily used for military reconnaissance purposes (*Curlander and McDonough, 1991*). They were typically operated at relatively high frequencies compared to ground based radar systems, to achieve good along-track resolution (*Curlander and McDonough, 1991*). It was not until the mid 1960s that the first high resolution SLAR images were declassified and made available for scientific use (*Curlander and McDonough, 1991)*. These SLAR images were then immediately used for geologic mapping, oceanography, and land use (*MacDonald, 1969*). Especially, large areas of perpetually cloud-covered regions were mapped for the first time. It dramatically demonstrates the benefits of a high resolution radar imager.

Wiley noted that the reflections from two fixed targets at an angular separation relative to the velocity vector could be resolved by frequency analysis of the along-track spectrum. This characteristic permitted the azimuth resolution of the return echoes to be enhanced by separating the echoes into groups based on their Doppler shift (*Curlander and McDonough, 1991*). Wiley referred to his technique as Doppler beam sharpening rather than synthetic aperture radar in his patent application (*Wiley, 1965)*.

The radar group at the Goodyear research facility in Litchfield, Arizona, pursued Wiley's beam sharpening concept and built the first airborne SAR system, flown aboard a DC-3 in 1953 (*Curlander and McDonough, 1991)*.

An independent and nearly parallel development of synthetic aperture radar was carried out by a group at the University of Illinois under the direction of C.W. Sherwin (*Sherwin, et al., 1962*). The Illinois group and the University of Michigan developed a number of operational airborne SAR systems that routinely began producing strip maps by 1958.

In USA, the first SAR system, with a single polarization X-band, built originally by the Environmental Research Institute of Michigan (ERIM) for the US Department of Defense in 1964, was declassified in the late 60s by reducing its rang bandwidth to 30MHz. This system, flown on a C-46 aircraft, was upgraded by NASA in 1973 by adding a second frequency at L-band and equipping the system with served dual-polarized antennas (*Rawson and Smith, 1974*) This ERIM SAR was used for a number of scientific research applications, especially the imaging of arctic sea ice. The Jet Propulsion Laboratory (JPL) also developed an L-band SAR system. The JPL SAR had been upgraded to a simultaneous qual-polarized (polarimetric) capability in both L- and C-bands by the early 1980s. This system was used for geologic mapping and the study of geomorphic processes (*Schaber, et al., 1980*). A Seasat SAR was approved by NASA in1975. It was launched in July 1978. It is the first civilian spaceborne SAR (*Cumming and Wong, 2005*). The Seasat SAR observed a number of unique ocean features that significantly contributed to study of global oceans (*Fu, L.-L. and B. Holt, 1982*). The Seasat system was designed primarily to image the oceans with its steep 23° incidence angle, Seasat data was widely applied in geology, polar ice, and land use

mapping (*Elachi, 1982*). However, Seasat was limited in terms of the duration of the data collection due to a complete power failure just 100 days after its launch.

The scientific results from Seasat quickly led to the approval by NASA of the Shuttle Imaging Radar (SIR) series of flights (*Elachi, 1982; Elachi, et al., 1982*). These systems, which used many of the Seasat designs, were also L-band, HH, single channel SARs. The SIR-A was primarily for geologic and land applications with a fixed look angle 45° off nadir, while SIR-B featured a mechanically steerable antenna mount for a range of look angles from 15-60°. SIR-C/X-SAR is an imaging radar system scheduled for launch aboard the NASA Space Shuttle in 1994. It is a quad-polarized L- and C-band SAR. SIR-C/X-SAR's unique contributions to Earth observation and monitoring are its capability to measure vegetation type, extent and deforestation, soil moisture content, ocean dynamics, wave and surface wind speeds and directions, volcanism and tectonic activity, soil erosion and desertification. These systems were operating synchronously and were capable of simultaneously recording nine polarizations (L- and C-bands HH, HV, VH, VV and X-band VV).

ALMAZ, the Russian SAR satellite, was launched in 1991. Its main unique feature was its operation at a frequency of 3 GHz (S-band) (*Cumming and Wong, 2005*). A typical radar image covered a region 20-45 km wide and 20-240 km long with a resolution of 15-30 m. However, ALMAZ could aim its coverage over a swath at least 350km wide. Unfortunately, the failure of one of the SAR antennas to deploy fully rendered that side inoperable (*http://www.fas.org/spp/guide/russia/earth/almaz.htm*).

ERS-1/2, The European Remote Sensing satellite, ERS-1, was launched in 1991. Twelve European nations and Canada combined to build a multi-instrument microwave satellite (*Cumming and Wong, 2005*). The SAR operated at C-band (wavelength of 5.7 cm).

ERS-2, with the same specifications as ERS-1, was launched in 1995. Its operation in tandem with ERS-1 opened up the field of repeat-pass satellite SAR interferometry (*Cumming and Wong, 2005*). Tandem that was taken from almost the same vantage point and with one-day interval between observations could be used to measure height and to detect changes in surface features (*Cumming and Wong, 2005*).

J-ERS, the Japanese Earth Remote Sensing Satellite, was launched in 1992. It operated at a frequency of L-band (wavelength of 23.5cm).

RADARSAT-1 satellite was launched by the Canadian Space Agency in 1995. It operated at C-band (wavelength of 5.6cm). The main applications of the satellite were ice monitoring, environmental monitoring, disaster management, coastal waters and open oceans, hydrology, geology, agriculture, and forestry. A novel application of RADARSAT-1 was its use in the Antarctic Mapping Mission in 1997 (*Cumming and Wong, 2005*). The satellite imaged the areas near South Pole for the first time (*Cumming and Wong, 2005*).

SRTM, the Shuttle Radar Topography Mission (SRTM), consisted of a specially modified radar system that flew onboard the Space Shuttle Endeavour during an 11-day

mission in February of 2000 (*http://www2.jpl.nasa.gov/srtm/*). The received data generates the most complete high-resolution digital topographic database of Earth (*http://www2.jpl.nasa.gov/srtm/*).

ENVISAT/ASAR, the third European satellite SAR system was launched in February 2002. It operates at C-band (wavelength of 5.6cm). It builds upon ERS-1 and ERS-2 technology by providing polarizations plus wide swath and ScanSAR modes (*Cumming and Wong, 2005*).

ALOS/PALSAR, the Advanced Land Observing Satellite following the Japanese Earth Resources Satellite (JERS-1), was launched in 2006. The Phased Array type L-band Synthetic Aperture Radar (PALSAR) is an active microwave sensor which operates at L-band (wavelength of 23.6 cm). PALSAR is the first L-band synthetic aperture radar (SAR) having the duration and orbital accuracy needed to monitor slow crustal deformation globally (*Shimada, et al., 2007; Rosenqvist, et al., 2007*).

TerraSAR-X, German SAR satellite, was launched in June 2007. TerraSAR-X is a 1 meter resolution class radar satellite. The satellite works in the X-band (wavelength of 3.1 cm).

RADARSAT-2, Canada's next-generation commercial SAR satellite following on to RADARSAT-1, was launched in December 2007. It operates at C-band (wavelength of 5.5cm). RADARSAT-2 has been designed with significant and powerful technical advancements which include 3m high-resolution imaging, flexibility in selection of

polarization, left and right-looking imaging options, superior data storage and more precise measurements of spacecraft position and attitude (*http://www.radarsat2.info/about/mission.asp*).

Cosmo-Skymed satellites, Constellation of Small Satellites for Mediterranean basin Observation, were developed by Italy. The program involves the launch of a constellation of four satellites. The first satellite of the constellation was launched on 7th June 2007, the second on 8th December 2007 and the third on 24th October 2008. The four satellites, each equipped with a multi-mode high-resolution SAR, operate at X-band. COSMO-SkyMed was conceived as a dual use program intended to meet both civil and defense objectives. The application services that can be derived from COSMO-SkyMed will contribute significantly to the defense of the territory in areas such as fire, landslides, droughts, floods, pollution, earthquakes and subsidence, management of natural resources in agriculture and forestry, as well as monitoring of urban sprawl (*http://www.telespazio.it/cosmo.html*).

TanDEM-X is scheduled for launch in 2009. Together with the almost identical radar satellite TerraSAR-X, it will form a high-precision radar interferometer.

2.1.2 Applications of SAR data

The SAR data have a wide range of practical applications, such as:

On the land: spaceborne imaging radar data are being used or have the potential for use in a wide range of geoscientific applications such as geologic structural and lithologic mapping, vegetation and soil moisture monitoring, forestry inventory, land use earthquakes, surface rupture by earthquake faulting, anthropogenic deformation, glaciers, landslides, volcanoes, subtle deformation (*Elachi,1988;http://earth.esa.int/ applications /data_util/SARDOCS/*).

On the ocean: the surface phenomena include surface swells, internal waves, currents, wind cells, eddies, ship wakes, and oil spills, can be imaged by SAR with high resolution at any time (day and night) and irrelevant of environmental conditions (cloud cover, storms) (*Elachi, 1988)*. It is particularly valuable in global oceanographic research (*Elachi, 1988)*.

2.2 Synthetic Aperture Radar Interferometry (InSAR)

2:2.1 Introduction

Synthetic Aperture Radar Interferometry (InSAR), as a new geodetic technology, has been applied measuring changes in the Earth's surface in the early 1990s (*Massonnet and Rabaute, 1993b; Rosen, et al., 2000; Bürgmann, et al., 2000*). By exploring the phase of the coherent radar signal, interferometry has transformed radar remote sensing from a largely interpretive science to a quantitative tool, with applications in cartography, geodesy, land cover characterization, and natural hazards (*Rosen, et al., 2000*).

By using at least two complex-valued SAR images acquired from different orbit positions and/or at different times, InSAR allows accurate measurements of the radiation travel path (*Bamler and Hartl, 1998; Ferretti et al., 2007a*). Measurements of travel path variations as a function of the satellite position and time of acquisition allow generation of Digital Elevation Models (DEM) and measurement of centimetric surface deformation of the terrain (*Massonnet and Rabaute, 1993b; Ferretti, et al., 2007b; Graham, 1974; Zebker and Goldstein, 1986; Massonnet, et al., 1993a; Zebker, et al., 1994; Rosen, et al. 1996; Stevens, 1999*).

This section will briefly review the principle of repeat-pass satellite SAR Interferometry applied to measure ground deformation and the limits of interferometric measurements.

2.2.2 Principles of SAR Interferometry

There are three InSAR technologies. They are "cross-track interferometry" (XTI), "along-track interferometry" (ATI), and "repeat-track interferometry" (RTI) (*Rosen, et al., 2000*).

Cross-track interferometry, using two apertures on a single platform, was developed for routine topographic mapping. Along-track interferometry, by arranging two antennas along the flight track on a single platform, was advanced by Goldstein and Zebker (*Goldstein and Zebker, 1987*) for measurement of surface motion by imaging the surface at multiple times. Repeat-track interferometry can be used to generate topography and

motion. ATI is merely a special case of RTI (*Rosen, et al., 2000*). The orbits of several spaceborne SAR satellites have been controlled to nearly retrace themselves after several days.

Repeat-track interferometry has been recognized as the most promising space-geodetic technology for monitoring Earth's surface deformation (*Klees and Massonnet, 1998*). Leveling surveying, Global position System (GPS) and other so-called point-based methods have been often used to monitor the land subsidence. These methods can only measure limited number of points, and they are manpower intensive, costly and time consuming. Especially, if the land subsidence is large-scale, it is impossible for these traditional methods to monitor the disaster. Repeat-track interferometry has been developed in recent ten years. It can monitor the land subsidence frequently, timely, regularly, highly automatically and in large scale. It has the potential of mapping centimeter-scale ground deformation over a region many tens of kilometers in size at a resolution of a few meters.

The basic principles of repeat-track interferometry are briefly described here. Let us suppose two SARs fly on (ideally) parallel tracks and view the terrain from slightly different directions. In Fig. 2.1, SAR1 and SAR2 represent locations of SAR system where it images the area of interest twice. The separation of the flight paths is defined as B. α is the baseline angle with respect to the horizontal line. θ is look angle. R is the distance from every point of the Earth's surface to SAR antenna.

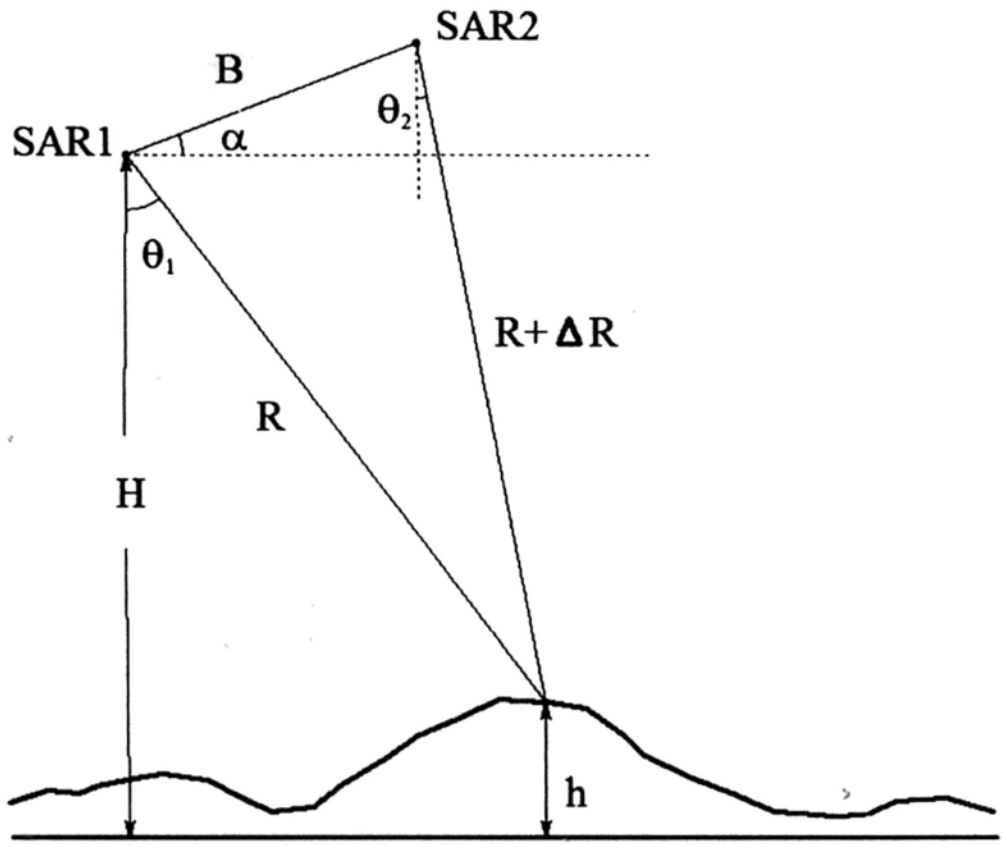

Figure 2.1 Illustration of repeat-track SAR interferometry.

Let

$$s_1(R,x) = |u_1(R,x)| \exp\{i\phi_1(R,x)\} \tag{2.1}$$

and

$$s_2(R+\Delta R,x) = |u_2(R+\Delta R,x)| \exp\{i\phi_2(R+\Delta R,x)\} \tag{2.2}$$

be the two SAR images forming the interferogram

$$\upsilon(\cdot) = s_1(R,x)s_2^*(R+\Delta R,x) = |s_1(\cdot)s_2^*(\cdot)| \exp\{i\phi(\cdot)\} \tag{2.3}$$

Where

$$\phi(\cdot) = \phi_1(\cdot) - \phi_2(\cdot) \tag{2.4}$$

is the interferometric phase.

The phase of the SAR image response of a point scatter is proportional to range plus a possible shift due to the scatterer itself, i.e.

$$\phi_1 = -2kR + \phi_{scat,1} \tag{2.5}$$

and

$$\phi_2 = -2k(R + \Delta R) + \phi_{scat,2} \tag{2.6}$$

Assuming that the scattering phase is the same in both images the interferogram phase is a very sensitive measure for the range difference:

$$\phi = 2k\Delta R = \frac{4\pi}{\lambda}\Delta R \tag{2.7}$$

ϕ is still ambiguous to within integer multiples of 2π .

$$\begin{aligned} \phi &= \frac{4\pi}{\lambda}\Delta R + 2\pi N \\ N &= 0, \pm 1, \pm 2, \cdots \end{aligned} \tag{2.8}$$

According to the geometrical relationship shown in Fig. 2.1, one can get

$$\sin(\theta-\alpha)=\frac{(R+\Delta R)^2-R^2-B^2}{2RB} \tag{2.9}$$

$$h=H-R\cos\theta \tag{2.10}$$

If $(\Delta R)^2$ is ignored, one can get

$$\Delta R\approx B\sin(\theta-\alpha)+\frac{B^2}{2R} \tag{2.11}$$

In satellite SAR system, $B<<R$, $\frac{B^2}{2R}$ can be ignored.

$$\Delta R\approx B\sin(\theta-\alpha) \tag{2.12}$$

The perpendicular component of baseline, is defined as

$$B_{\perp}=B\cos(\theta-\alpha) \tag{2.13}$$

The baseline component which is parallel to the radar look angle is defined as

$$B_{\parallel}=B\sin(\theta-\alpha) \tag{2.14}$$

$$\Delta R\approx B_{\parallel} \tag{2.15}$$

$$\phi=\frac{4\pi}{\lambda}B_{\parallel} \tag{2.16}$$

In Fig. 2.2, the distance from point P of the Earth's surface to SAR antenna is equal to the one from point P'. The topographic height between P and P' is h. $\Delta\theta_h$

is angle increment. The interferometric phase at P' is

$$\phi' = \frac{4\pi}{\lambda} B \sin(\theta + \Delta\theta_h - \alpha) \tag{2.17}$$

The phase difference between the two points is

$$\begin{aligned} \Delta\phi_h &= \phi' - \phi = \frac{4\pi}{\lambda}\left[B\sin(\theta + \Delta\theta_h - \alpha) - B\sin(\theta - \alpha)\right] \\ &= \frac{4\pi}{\lambda} B\cos(\theta - \alpha)\Delta\theta_h = \frac{4\pi}{\lambda} B_\perp \frac{h}{R\sin\theta} \end{aligned} \tag{2.18}$$

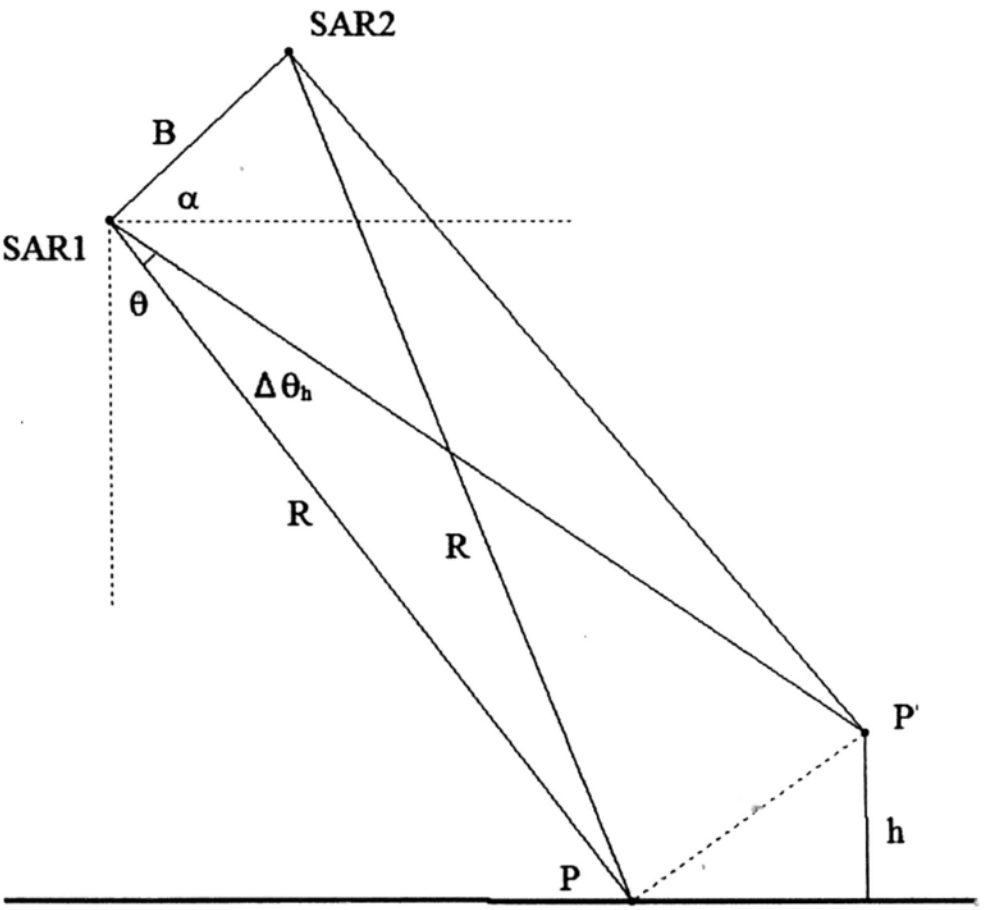

Figure 2.2 Illustration of two-pass SAR interferometry.

2.2.3 Limits of interferometric measurements

InSAR technology involves phase comparison of SAR images, acquired at different times with slightly different looking angles (*Bamler and Hartl, 1998; Gabriel, et al., 1989; Massonnet and Feigl, 1998; Rosen, et al., 2000; Colesanti, et al., 2003*). Since it has the potential to detect target displacements along the line of sight (LOS) direction with centimetric accuracy, it has been applied mapping land subsidence, volcano dynamics, coseismic and postseismic displacements along faults, and slope instability (*Amelung, et al., 1999; Carnec, et al. 1996; Rosen, et al., 1996; Owen, et al., 1995; Klees and Massonnet, 1998; Lu, et al., 1997; Massonnet, et al., 1994; Massonnet, et al., 1995b; Peltzer and Rosen, 1995; Price and Sandwell, 1998; Fruneau, et al., 1996; Wegmuller and Werner, 1997*). However, limits of InSAR degrade its application result. These drawbacks limit a full operational capability of this technology.

1. Temporal decorrelation

In InSAR technology, assume scattering phase contribution remains constant between the two phase images. However, in some situations, each pixel undergoes a random phase change. It will not vanish in their difference. Speckles appear in the interferogram. The phenomenon called "temporal decorrelation" or "incoherence". These extreme situations include water-covered surfaces, tidal areas near coastlines and plowed or irrigated agricultural fields (*Wegmuller and Werner, 1997*).

2. Atmospheric artifacts

The determination of deformation contribution using InSAR is based on the

assumption that the radar signal propagates unaffected in the atmosphere. However, Path delays occur in both the ionosphere and the troposphere (*Hanssen, 1998; Hanssen, 2001; Williams, et al., 1998; Goldstein, 1995; Zebker, et al., 1997; Sandwell and Price, 1998*). The atmospheric phase delay is severely caused by troposphere. It may be extremely difficult to discriminate deformation phase from the atmospheric phase with individual interferograms (*Massonnet and Feigl, 1995a; Massonnet and Feigl, 1998; Sandwell and Price, 1998*). In order to reduce atmospheric effect, Interferogram stacking approaches have been outlined and developed (*Zebker, et al., 1997; Sandwell and Price, 1998*).

3. Gradient limit

The maximum detectable deformation gradient for InSAR is one fringe per pixel. If deformation locally exceeds this threshold, incoherence occurs. This threshold depends on satellite, it is 3 mmm^{-1} for ERS and 13 mmm^{-1} for JERS (*Massonnet and Feigl, 1998*).

4. Geometric imaging constraints

SAR uses side-looking geometry to image. It can result in inherent constraints: layover, foreshortening and shadowing on SAR images. For steep slopes and high buildings, layover occurs on SAR images, since the upper section of the slope (or building) is closer to the senor, and therefore it appears to be laid over the lower section. When SAR looks down and to the side toward a steep slope, many objects on the mountain's facing slope may appear to be located at the same distance from the satellite. Since those many objects are located at nearly the same distance from the SAR, their

backscattered signals will return to SAR at about the same time. The SAR sensor will interpret this as a single object located at that distance; consequently, the SAR image will be very bright at that location, in which all those responses from the separate objects are mapped into one location. This is called foreshortening. Shadowing will also occur in cases where the front side of a slope or mountain creates a shade effect on the back side of the slope or mountain.

With the development of InSAR technology and new SAR system, the limits of InSAR have been or will be overcome. The advantages of its application in measuring changes in the Earth's surface are remarkable.

2.3 Differential Synthetic Aperture Radar Interferometry (D-InSAR)

Take three-pass interferometry as an example, in this section, I will briefly describe the principles of D-InSAR. The method is based on three radar images (*Zebker, et al., 1994; Gabriel, et al., 1989*). It has the advantages of not requiring any information other than the radar data.

Fig. 2.3 shows the geometry of three-pass interferometry. In Fig. 2.3, SAR1 and SAR2 represent locations of SAR system where it images the area of interest twice. Let us assume that the first SAR image is acquired before ground deformation occurs; the second image is obtained after ground deformation occurs. Then the phase of ground point P is

$$s_1(R_1) = |s_1(R_1)| \exp\left(-\frac{4\pi}{\lambda} R_1\right) \tag{2.19}$$

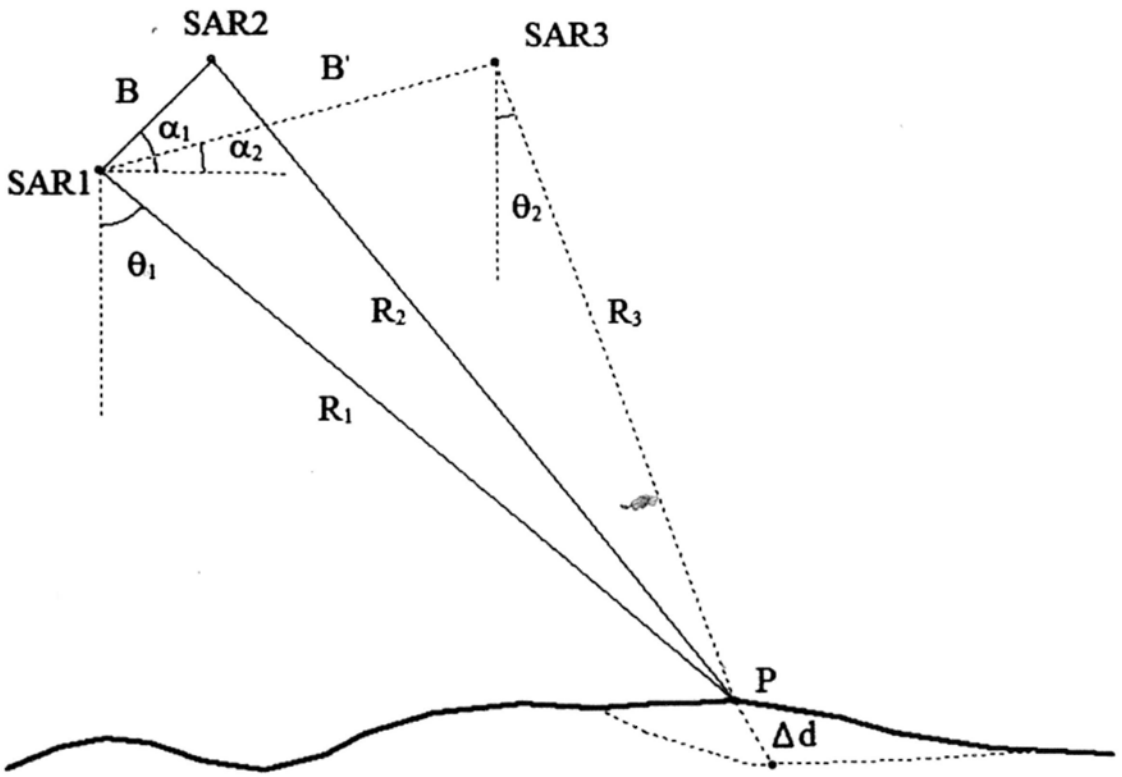

Figure 2.3 Illustration of two-pass SAR interferometry.

After ground deformation occurred, the second SAR image acquired. Assume that comparing with resolution cell of SAR, the deformation is small; and the radar signal is still coherent. The radar signal of the second SAR image at ground point P is

$$s_2(R_2) = |s_2(R_2)| \exp\left(-\frac{4\pi}{\lambda}(R_2 + \Delta d)\right) \tag{2.20}$$

Δd is ground deformation along the radar LOS between the observations. The phase of the first interferogram which is generated by the two SAR images includes the

topographic phase and ground deformation phase occurred during the observation period.

$$\phi_1 \approx -\frac{4\pi}{\lambda} B_{\parallel} - \frac{4\pi}{\lambda} \Delta d = -\frac{4\pi}{\lambda} B \sin(\theta_1 - \alpha_1) - \frac{4\pi}{\lambda} \Delta d \qquad (2.21)$$

In order to obtain ground deformation phase, topographic effects should be eliminated. There are three methods which are used to eliminate the topographic contribution. First one, one can select two images of which the baseline length is zero. In the case, topographic contribution can be ignored. Ground deformation along the radar LOS can be calculated using Equation (2.21). However, the kinds of image pairs are rare. The second, the topographic can be eliminated by subtracting the fringe pattern calculated from external digital elevation model (DEM). It is called two-pass interferometry. The third method is three-pass interferometry. This method has the advantage of not requiring any information other than the radar data. It uses three images with the same master to construct two interferograms. The second one is due only to relief. We may subtract fringes caused by topographic effect in the first interferogram from the second one.

Let us assume that we obtain the third SAR image before ground deformation occurs. Then the phase of the point P in the third SAR image is

$$s_3(R_3) = |s_3(R_3)| \exp\left(-\frac{4\pi}{\lambda} R_3\right) \qquad (2.22)$$

Using the first image and the third one, the second interferogram can be constructed, and the phase of which is due only to relief.

$$\phi_2 \approx -\frac{4\pi}{\lambda} B'_{\parallel} = -\frac{4\pi}{\lambda} B' \sin(\theta_2 - \alpha_2) \tag{2.23}$$

The phase caused by ground deformation along LOS is

$$\phi_{\Delta d} = \phi_1 - \frac{B_{\parallel}}{B'_{\parallel}} \phi_2 = -\frac{4\pi}{\lambda} \Delta d \tag{2.24}$$

$\phi_1, B_{\parallel}, B'_{\parallel}, \phi_2$ can be calculated using the phase values of two inteferograms and orbit parameters. So the ground deformation along LOS Δd of each pixel can be obtained.

The ratio of two image pairs

$$\frac{B_{\parallel}}{B'_{\parallel}} = \frac{B \sin(\theta_1 - \alpha_1)}{B' \sin(\theta_2 - \alpha_2)} \tag{2.25}$$

is function of look angle θ. It depends on imaging parameters and the relief of every pixel on SAR image. In order to calculate ground deformation along LOS with Equation (2.24) and (2.25), DEM or other methods should be used to obtain the height information of the area of interest. According to the principles of InSAR, look angle θ consists of reference look angle θ_0 and increment of local look angle $\Delta\theta_Z$. With respect to $\Delta\theta_Z$, it varies with the local relief. An indirect method can be used to flatten the fringe variation caused by local relief in the interferogram. After removing the flattened phase, the new phases are given by

$$\phi_{f1} = -\frac{4\pi}{\lambda} B\left[\sin\left(\theta_{0_1} + \Delta\theta_{z_1} - \alpha_1\right) - \sin\left(\theta_{0_1} - \alpha_1\right)\right] - \frac{4\pi}{\lambda}\Delta d$$
$$= -\frac{4\pi}{\lambda} B\cos\left(\theta_{0_1} - \alpha_1\right)\Delta\theta_{z_1} - \frac{4\pi}{\lambda}\Delta d \tag{2.26}$$

$$\phi_{f2} = -\frac{4\pi}{\lambda} B'\left[\sin\left(\theta_{0_2} + \Delta\theta_{z_2} - \alpha_2\right) - \sin\left(\theta_{0_2} - \alpha_2\right)\right]$$
$$= -\frac{4\pi}{\lambda} B\cos\left(\theta_{0_2} - \alpha_2\right)\Delta\theta_{z_2} \tag{2.27}$$

Assuming that $\Delta\theta_{0_1} \approx \Delta\theta_{0_2}$, Equation (2.24) can be given using unflatten phase

$$\phi_d = \phi_{f_1} - \frac{B_\perp}{B'_\perp}\phi_{f_2} = -\frac{4\pi}{\lambda}\Delta d \tag{2.28}$$

In this equation, ground deformation Δd can be calculated without accurate θ and relief information. It should be noted that in the processing of flattening process, if the baseline distance value is not the real one, error will be induced in interferometric phase, and will cause distortion of deformation map.

The ground deformation along LOS gives rise to an interferometric phase of

$$\frac{\phi_d}{\Delta d} = -\frac{4\pi}{\lambda} \tag{2.29}$$

Since the wavelength is in the order of centimeters, D-InSAR can measure displacements down to millimeter accuracy, provided that that coherence is high enough. Recently, Stramondo et al. used differential SAR interferometry (DinSAR) to detect ground deformation after the Sichuan earthquake (*Stramondo, et al., 2008*).

The figure shows below is the D-InSAR processing flow.

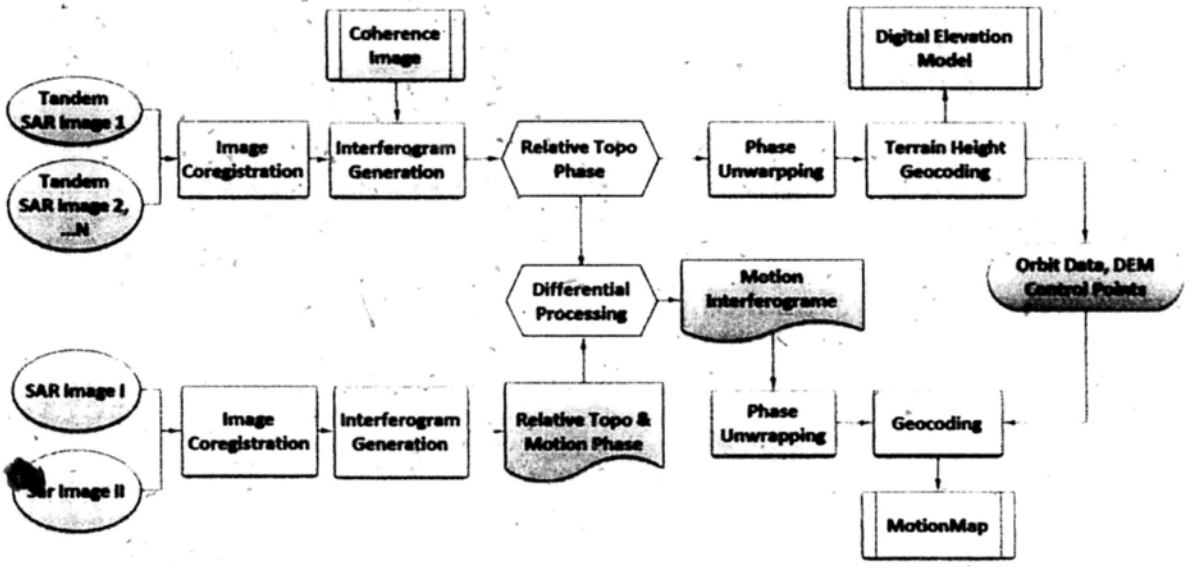

Figure 2.4 D-InSAR processing flow.

The five processing steps of 3-pass interferometry are

1. The three radar images must be coregistered with a precision of a fraction of a pixel.

2. Construct two interferograms with the same master image.

3. Subtract these calculated fringes from the second interferogram which is due only to relief, eliminating topographic effects.

4. Then the wrapped differential interferogram is unwrapped.

5. Project the unwrapped interferogram into an orthogonal cartographic or geographic coordinate system.

The three pass interferometry only uses radar data to calculate ground deformation along LOS. However, comparing with the two-pass interferometry, the method has several drawbacks, which limit its practical usefulness:

1. The first interferogram must be unwrapped. Since the unwrapping is not an easy work and may induce errors, particularly where the fringes become dense or incoherent, moreover, once the errors were induced, they will properly recycle as incorrect topographic information in the final interferogram and are not easy to recognize, the difficult areas which have low coherence are advisably masked.

2. The three-pass method uses the complementary image pair to estimate the topography. However, an interferogram always contains atmospheric contributions. It was not recognized in the process.

3. Since the three-pass interferometry includes only three SAR images, there is no knowledge of the topographic information, it cannot apply a pulse response filter during the interferometric fusion, diminishing the quality of the interferogram (*Massonnet and Feigl, 1998*).

4. Three-pass approach requires that all three images are acquired by the same

satellite in the same orbital track. However, DEM can be calculated from a pair of images in another orbital track, or even another satellite. In this case, the DEM cannot be used in three-pass. Moreover, the two images pair used in generating DEM should have good coherence. That is to say the time interval of the two observations should not be too long, and the baseline should not also be too long. The probability of finding three coherent images is smaller than find two such images.

2.4 PSI (Persistent Scatterer Interferometry)

Since the late 1990s, an advanced InSAR approach, referred to Persistent Scatterers Interferometry (PSI), has been used to monitor ground deformation with a millimetric accuracy by exploiting certain point-wise radar targets, which are highly coherent over long time intervals and for long spatial baselines (*Ferretti, et al., 2000; Ferretti, et al., 2001; Ferretti, et al., 2007a; Mora, et al., 2003; Werner, et al., 2003; Wegmuller, 2003; Hooper, et al., 2004; Lanari, et al., 2004; Kampes, 2006; Crosetto, et al., 2007a; Crosetto, et al., 2007b; Raucoules, et al., 2007*).

The Permanent Scatter (PS) technology has been developed in 2000 by Alessandro Ferretti, Claudio Prati, and Fabio Rocca of the Technique University of Milan (POLIMI). It aims to overcome the limitations----temporal and geometrical decorrelation which prevents SAR interferometry from being an operational tool in practice, and atmospheric effect which can strongly degrade the accuracy of the interferometric result (*Ferretti, et al., 2000; Ferretti, et al., 2001; Kampes, 2006*). The spatial density of PS is much higher

than the grids that are generated by the traditional point-based methods, such as leveling surveying and Global Positioning System (GPS) technology. In particular, in the urban areas the PS density may reach as high as 100 PS km^{-2}. The accuracy of deformation measurements may be raised to 0.1–1 mma^{-1} on the averaged line-of-sight deformation rate, and 1–3.5 mm on a single measurement (*Ferretti, et al., 2001; Dehls, 2006*). This implies that the PS technique can be used as an operational tool to measure ground deformation with a high accuracy and a high spatial PS grid density.

Meanwhile, similar processing algorithms are developed, such as Coherent Target Monitoring (CTM), Interferometric Point Target Analysis (IPTA), Spatial Temporal Unwrapping Network algorithm (STUN), and Stanford Method for PS (StaMPS) (*Kampes, 2006*). These methods have been very successful for time series analysis of radar images containing large numbers of stable pixels in urban or non-urban areas.

Comparing PSI with D-InSAR technology, I summarize advantages and drawbacks of both of them (*Ferretti, et al., 2000*).

1. All the available SAR images can be exploited in PSI without concern for the temporal and spatial baseline. On the contrary, only images pairs with small spatial and temporal baseline can be included for D-InSAR. That's to say D-InSAR can not exploit all the available images.

2. Atmospheric effect with low spatial frequency can be practically eliminated in PSI. It is a major limit of D-InSAR.

3. A coarse DEM can be used in PSI since the accurate elevation of each PS is estimated. D-InSAR needs accurate DEM for extracting ground deformation information. A coarse DEM used in D-InSAR will induce error for obtaining ground deformation, since there is no model for eliminating DEM errors.

4. Coherent pixels can be identified, although images pairs with large temporal and spatial baselines are included in PSI.

5. Although coherent pixels with high density can be identified in most areas, little PS can be found in low-reflectivity areas in PSI.

6. Temporal sampling is limited by satellite repeat cycles for both technologies.

7. Only "slow" deformation (<10 cma^{-1} in LOS) can be measured by both technologies.

As mentioned before, the concept of the Permanent Scatterer (PS) technology was first raised by a research team at POLIMI (*Ferretti, et al., 2000; Ferretti, et al., 2001*). The motivation for developing this technique is to overcome the limitations of temporal and geometrical de-correlation, which prevents SAR interferometry from being an operational tool in practice, and atmospheric effect, which can greatly degrade the accuracy of the interferometric results (*Ferretti, et al., 2000; Ferretti, et al., 2001*). The PS technology identifies the so-called permanent scatterers (PSs), which are image pixels coherent over long time series. The coherent values may be quite high even for

interferogram baselines that are longer than the critical length. Thus, the technology may exploit the interferometric phase and attain millimetric ground settlements based on the sparsely distributed PSs. The PS technique fully exploits a great number of archived SAR images, even the interferometric SAR images with baselines larger than the so-called critical baseline.

In our study, the Interferometric Point Target Analysis (IPTA) technology and ASAR images are used to generate ground deformation maps of Guangzhou urban area and Hong Kong International Airport. The IPTA is one of PSI technologies (*Werner, et al., 2003; Wegmuller, 2003*). The idea of IPTA technology is to use point targets for completely exploiting achieved data even for the interferometric pairs with long baselines. Thus, the technology is capable of reducing the errors resulting from the atmospheric path delay and increasing the temporal sampling rate. The selection criteria of point targets are mainly based on low spectral diversity, high backscattering intensity and low temporal variability of the SLC intensity. Another reason for this study choosing IPTA technology is that there is commercial software available. Our quite long term experience to use this software indicates that it is quite efficient and user-friendly.

The unwrapped interferometric phase ϕ_{unw} model of IPTA is the sum of topographic ϕ_{topo}, ground deformation ϕ_{def}, differential path delay phase ϕ_{atm}, and phase noise ϕ_{noise} terms (*Wegmuller, 2003*):

$$\phi_{unw} = \phi_{topo} + \phi_{def} + \phi_{atm} + \phi_{noise} \tag{2.30}$$

Across the layers of data stack, it is considered that the phase model is a linear dependence of the topographic phase on the perpendicular baseline component. A linear regression, which depends on the perpendicular baseline component, is employed. The slope of the regression line represents a relative height correction value. Consequently, the two-dimensional (2D) regression analysis, which is based on the perpendicular baseline and the time and treating deformation rate as a constant, is performed only for pairs with short spatial perpendicular baseline taken at all point targets. Next, for large stacks, a non-linear regression is performed using the wrapped phase. However, spatial phase unwrapping is prior to the non-linear regression for small stacks. The residual phase includes the atmospheric delay phase, non-linear deformation and an error term. According to different spatial and temporal dependences among different phase terms, an approach of a step-wise, iterative improvement of different parameters is used to separate different parameters and to refine the phase model expressed in Equation (2.30). By extending the point list to the refined phase model, there is an expectation that a few point targets may also be found in non-urban areas, enlarging the spatial coverage of point targets.

In summary, the IPTA technology is characterized by the following features: 1) It exploits the temporal and spatial characteristics of interferometric signatures collected from point targets (*Wegmuller, 2003*); 2) There are two different approaches, which are used to select point target candidates. For large data stacks, the criteria for an initial selection of point target candidates include low temporal variability of the backscattering

coefficient. In the case of small data stacks, the temporal variability criteria to select point target candidates become less reliable for statistical reasons. Thus, for small data stacks, the criteria are high backscattering and low spectral phase diversity. Combining the two approaches for limited data stacks may increase the reliability and confidence level of point target candidates (*Gamma Remote Sensing. GAMMA Software Documentation, 2006*). Both the two approaches for selection point target candidates are used in our experiments.

The Fig. 2.5 below shows the workflow of IPTA.

The IPTA processing begins by assembling a stack of co-registered single look complex images with the related SLC and orbit parameters. A DEM model is also used in the processing.

Based on the registered SLCs, a candidate list of point targets is determined. Point targets do not show the speckle behavior associated with distributed targets. Point targets are the pixels where a single coherent scatterer dominates the echo and behave somewhat like point scatterers. Criteria for an initial selection of point target candidates are low temporal variability of the backscattering coefficient. It works well for large data stacks. For small data stacks, the criteria are high backscattering and low spectral phase diversity. The point targets selected in this stage are only "candidates". At a later stage, the quality of the candidates will be more carefully evaluated. The point targets with poor quality will be rejected.

Then initial estimates of the interferometric baselines are calculated from the available orbit state vectors. A master image is selected according to the lengths of temporal, spatial and doppler baselines. Next, the differential interferograms are calculated only for the selected point targets candidates. It is done by simulation of the unwrapped interferometric phase based on the currently available information include initial baselines and the available DEM. No information on deformation and atmospheric phase delay is available at this stage. For each selected interferometric pair this simulation is calculated and subtracted from the interferogram. Depending on the accuracy of the assumed model parameters, the quality of the candidate points, and the baselines, these differential interferograms may look smooth or very noisy.

Then the stack of differential inteferograms is analyzed. For large stacks, it is done primarily in the temporal domain. The phase model indicates a linear dependence of the topographic phase on the perpendicular baseline component. Thus, for the phase differences between two image points a linear dependence on the perpendicular baseline component is found, with the slope of the regression indicating the relative height correction. The phase standard deviation includes terms related to $\phi_{noise}, \phi_{atm}, \phi_{def}$ and baseline errors. Except for ϕ_{noise}, these terms depend all on the distance between the two points.

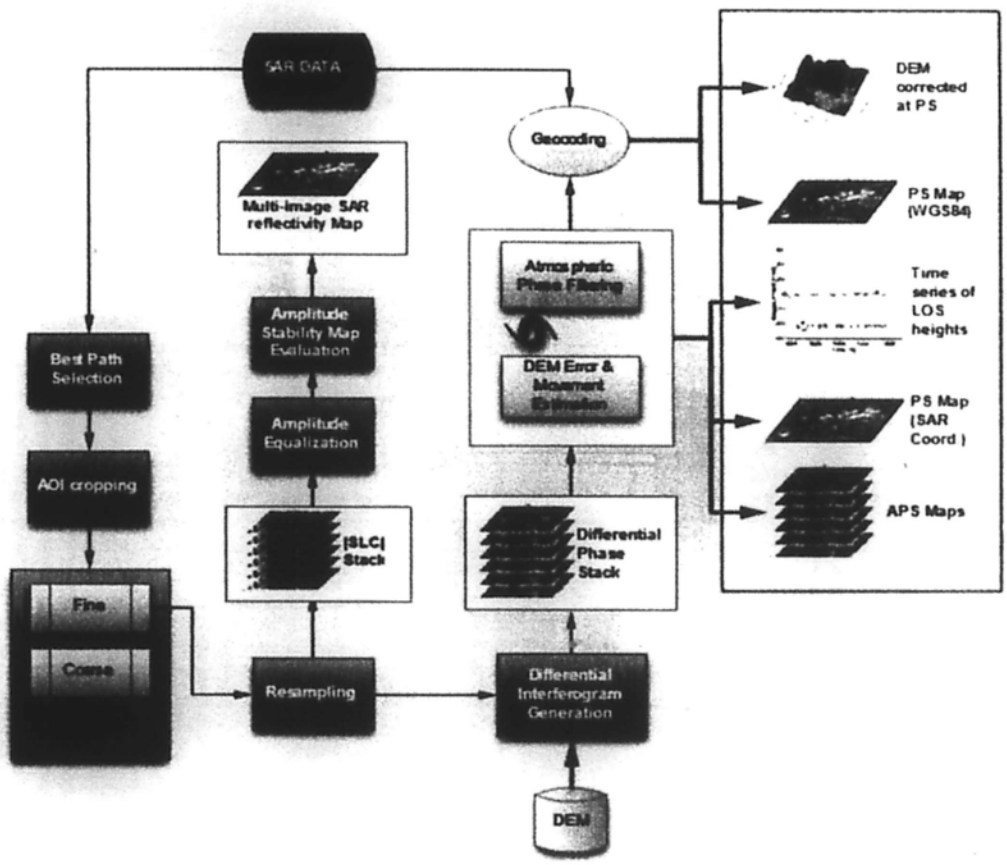

Figure 2.5 The workflow of IPTA.

Consequently, for pairs with short spatial separation this regression analysis can be done independently of the quality of ϕ_{atm}, ϕ_{def} and the baseline. The regression is further improved and made more robust by also considering linear phase dependence with time, equivalent to a constant deformation rate. One problem for the regression is that the phases in the differential interferograms are still wrapped. For large stacks performing a non-linear regression using the wrapped phase data is possible, but for small stacks, spatial phase unwrapping may be required prior to the regression step. The standard deviation of the phase from the regression is used as a quality measure, permitting to

detect and reject points which are not suited for IPTA analysis. This regression analysis is performed for the entire point targets.

The results from the regression analysis are height corrections, linear deformation rates, a quality measure, residual phases, and the unwrapped interferometric phase. These are used to improve the model. The height corrections, for example, are added to the DEM heights used in the simulation. The residual phase contains the atmospheric phase, which is related to the path delay heterogeneity at the two acquisition times of the pair, as well as non-linear deformation and error terms. Different phase terms can be discriminated based on their differing spatial and temporal dependencies. The atmospheric path delay is low-pass in the spatial dimension, but uncorrelated from pass to pass. The non-linear deformation is generally low pass in the spatial and temporal dimension, but there may be cases where this is clearly not the case. Baseline related errors are low-pass in the spatial dimension and uncorrelated from pair to pair. Finally, the phase noise is random in both spatial and temporal dimensions.

An important aspect of the IPTA concept is the possibility of a step-wise, iterative improvement of different parameters. Main improvements include the consideration of a height correction, a deformation rate, a baseline refinement, atmospheric phase terms, and extension of the point list.

The IPTA result consists of the improved model, including heights, linear deformation rates, atmospheric phase delays, refined baselines, quality information, and

non-linear deformation histories for each point.

2.5 Error sources and analysis in Radar Interferometry

The final InSAR results can be influenced by several kinds of errors. The main error sources are atmospheric effect, temporal and geometric decorrelation, phase ambiguity number, orbits and DEM errors (*Hanssen, 2001; Liu, 2003*).

1. Atmospheric effect

For repeat-pass interferometry, the atmospheric effect is one of the most intractable problems. It is well known that radar signals suffer from propagation delays when they travel through the atmosphere. The atmospheric state can vary considerably among the acquisitions. Additional shifts in phase signals occur. Any differences in path delays often introduce significant errors. Zebker et al., reported 10-14cm errors in the measured ground deformations can be induced by the spatial and temporal changes of 20% in the relative humidity of the atmosphere in the case of the SIR-C/X-SAR.

The atmospheric correction approaches from SAR interferograms which have been developed in recent years are pair-wise logic or linear combination (*Massonnet and Feigl, 1995a; Hanssen, 2001*), stacking (*Zebker et al., 1997; Sandwell and Price, 1997; Ferretti, et al., 1999; Emardson, 2003*), modeling of atmospheric delays based on ground meteorological data (*Saastamoinen, 1972; Baby, ett al., 1988; Askne and Nordius, 1987; Bonforte, et al., 2001; Delacourt, et al., 1998*), numerical atmospheric model (*Shimada,*

2000; Shimada, et al., 2001; Wadge, et al., 2002; Webley, 2003), stochastic filtering (*Crosetto, 2002*), persistent scatterers interferometry (*Ferretti, et al., 2000; Ferretti, et al., 2001*), the use of GPS measurements (*Bock and Williams 1997; Ge et al., 2000; Buckley, et al., 2003*), and the use of space-based radiometer measurement (*Li, 2005*).

These approaches have their own limitations in correction atmospheric effects. The atmospheric effect can not be eliminated, but only be reduced using these methods.

2. Temporal and geometric decorrelation

Temporal decorrelation occurs when the distribution of wavelength-scale scatterers within a resolution cell, or their electrical characteristics, differs as a function of time between the first and the second data acquisition, uncorrelated with other resolution cells (*Hanssen, 2001*).For the ERS images, the shortest temporal baseline is Tandem data. It is 1 day. For ASAR images, the temporal baselines are 35 days, 70days, 105days and so forth.

Temporal decorrelation can be caused by anthropogenic changes, weather conditions, and natural processes. Low temporal coherence values are generally obtained for areas covered by lush vegetation and snow.

Zebker and Villasenor present an analytical model of temporal decorrelation, in which only the movement of scatterers is considered (*Zebker and Villasenor, 1992*). In their model, temporal decoorelation equation related to changes in horizontal position and

height assuming Gaussian-statistic motion. If the probability distributions are Gaussian, after normalization the temporal decorrelation can be expressed by the equation shown below.

$$\rho_{temporal} = \exp\left\{-\frac{1}{2}\left(\frac{4\pi}{\lambda}\right)^2\left(\sigma_y^2 \sin^2\theta + \sigma_z^2 \cos^2\theta\right)\right\} \tag{2.31}$$

For the ASAR Image Mode Swath 2 geometry, the nominal incidence angle θ ranges from 19.2°to 26.7°. σ_y and σ_z are the rms displacements in horizontal position and in height respectively. According to the equation, the C-band data is more susceptible to displacements of scatterers than L-band data. 3 cm rms displacement can cause total decorrelation for C-band data; however 10 cm is for L-band data (*Liu, 2003*). Thus, for vegetated areas longer wavelength data are preferred.

Geometric decorrelation is a result of a difference in the angle of incidence between the two sensors (*Hanssen, 2001; Williams, et al., 1998; Gatelli, et al., 1994*). The geometric decorrelation can be defined with critical perpendicular baseline (*Hanssen, 2001*):

$$\left|\gamma_{geom}\right| = \begin{cases} \dfrac{B_{\perp,crit} - B_\perp}{B_{\perp,crit}}, & \left|B_\perp\right| \le B_{\perp,crit} \\ 0, & \left|B_\perp\right| > B_{\perp,crit} \end{cases}, \tag{2.32}$$

Where $B_\perp$ is perpendicular baseline, $B_{\perp,crit}$ is critical perpendicular baseline. $B_{\perp,crit}$ is defined as a function:

$$B_{\perp,crit} = \lambda(B_R / C)R_1 \tan(\theta_{inc} - \varsigma) \quad (2.33)$$

λ is wavelength, θ_{inc} is the incidence angle, and the topographic slope is ς. For a flat horizontal terrain, the ASAR critical baseline is approximately 1.2 km.

3. Phase ambiguity number

Phase unwrapping of an interferogram is an important step in InSAR. The purpose of phase unwrapping is to determine the phase ambiguity and absolute phase. If the expectation value of the wrapped phase is $E\{\phi^W\}$, the expectation value of unwrapped phase can be denoted as $E\{\phi\} = E\{\phi^W\} + k2\pi$, with $k \in Z$ (*Hanssen, 2001*).

The wrapped phases in an interferogram are often degraded by layover, superposition, shadows, low signal returns, poor image correlation, and signal aliasing. Errors induced by the integration of the phase gradients in one part of the interferogram can propagate into other parts easily (*Hanssen, 2001*). Most of the currently used phase unwrapping algorithms obey the integerness-condition. It implies that the errors introduced by phase unwrapping have a discrete ($k2\pi$) distribution (*Hanssen, 2001*).

4. Orbits and DEM errors

Orbital satellite state vectors are required to determine the spatial baseline. Orbit errors result in a residual reference phase in the interferogram which can be erroneously interpreted as topography, deformation, or atmospheric signal (*Hanssen, 2001*). The errors can propagate directly into topographic height or deformation maps. In our

experiments, precise orbit data are used to eliminate orbit errors.

DInSAR requires either an interferometric DEM or an external DEM to remove topographic phase contribution. Therefore, the quality of the DEM directly affects the quality of deformation measurements. DEM errors can be significantly reduced by choosing deformation pairs with short perpendicular baseline or selecting a good quality external DEM.

Chapter 3. Data and Data Processing

3.1 ENVISAT ASAR data

The Advanced Synthetic Aperture Radar (ASAR) instrument on board the ENVISAT satellite extends the mission of the Active Microwave Instrument (AMI) Synthetic Aperture Radar (SAR) instruments flown on the European Remote Sensing (ERS) Satellites ERS-1 and ERS-2 (*European Space Agency, 2002*). ASAR is the largest single instrument of ENVISAT, operating at C-band. It ensures continuity of data after ERS-2, despite a small (31 MHz) central frequency shift. It is characterized by enhanced capability in terms of coverage, range of incidence angles, polarization and modes of operation.

The ASAR instrument was designed with a life requirement of 5 years in the low earth polar orbit environment (*Hutchinson and Gibbons, 2000*). It has been still operative since ENVISAT was launched in 2002. Since the high data demand from both the science

and operational user communities combined with the good status of the ENVISAT satellite, during its 131st meeting on 26 May 2009, the ESA Earth Observation Programme Board has approved at unanimity the principle of a 3-years ENVISAT mission extension (2011, 2012, 2013) (*http://envisat.esa.int/object/index.cfm?fobjectid=6293*). However, as the ENVISAT on-board hydrazine will be almost completely consumed in the near future, a pre-requisite for the 3-years extension is the modification of the ENVISAT orbital parameters to allow operating the satellite with minimum amount of hydrazine. The new ENVISAT orbit will have a repeat cycle of 30 days instead of 35 days (*http://envisat.esa.int/object/index.cfm?fobjectid=6293*). The implementation of the new orbit is presently foreseen for October 2010. The current excellent ASAR interferometric capabilities will not maintain.

ASAR images have been mainly used for measuring sea state conditions, mapping ice sheet and snow, monitoring ship traffic, agriculture and forest, mapping topographic, predicting, tracking and responding to natural hazards and ground deformation monitoring (*European Space Agency, 2002*). The ASAR instrument is designed to provide five operational modes (*European Space Agency, 2002; http://esapub.esrin.esa.it/bulletin/bullet102/Desnos102.pdf*):

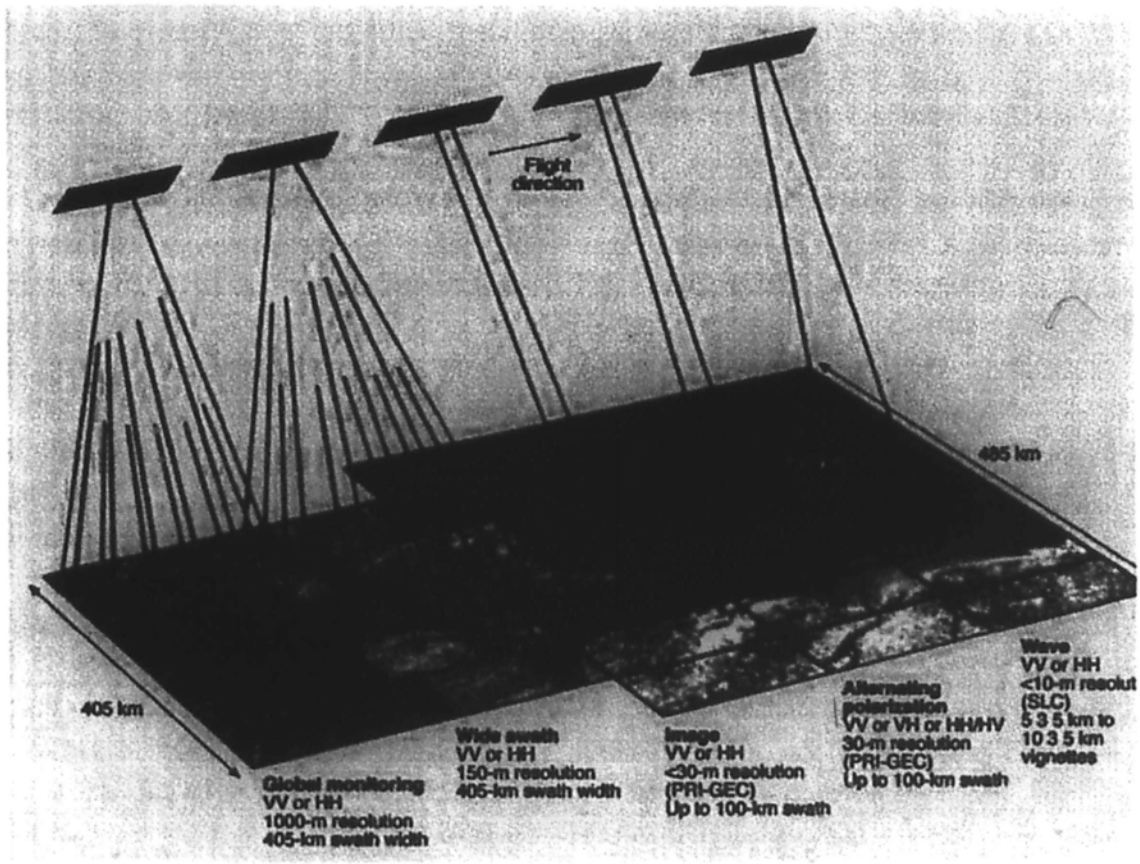

Figure 3.1 ASAR operating modes (Refer to (*European Space Agency, 2002*)).

The Image Mode (IM) generates high-spatial-resolution data products (30 m for precision images) selected from the total of seven available swaths located over a range of incidence angles spanning 15 to 45 deg with either vertically or horizontally polarized radiation. The images used in our study are all acquired by Image mode with swath 2.

The Wave Mode generates vignettes of 5 km by 5 km, spaced 100 km along-track. It uses the same swaths and polarizations as Image Mode.

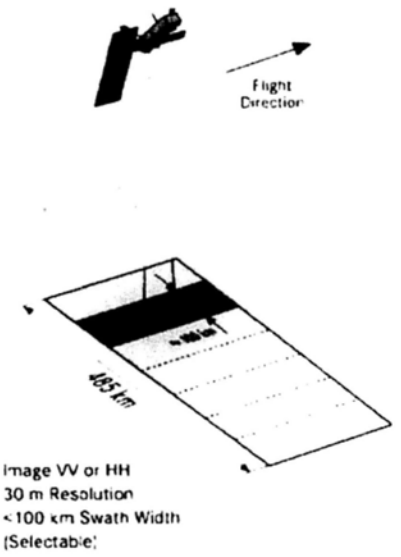

Figure 3.2 Image Mode (Refer to (*European Space Agency, 2002*)).

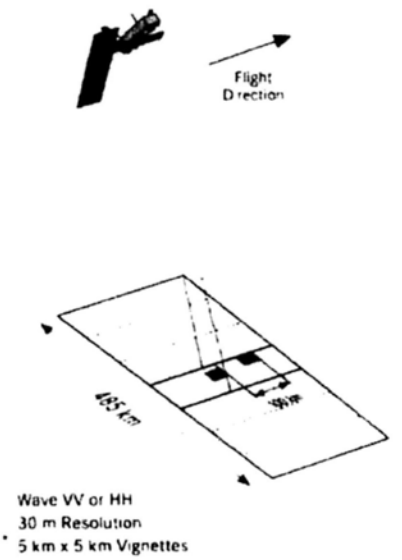

Figure 3.3 Wave Mode (Refer to (*European Space Agency, 2002*)).

The Wide Swath and Global Monitoring modes are based on the ScanSAR technique using five sub-swaths, and they generate wide-swath (400 km) with resolutions of 150 and 1000 m, respectively.

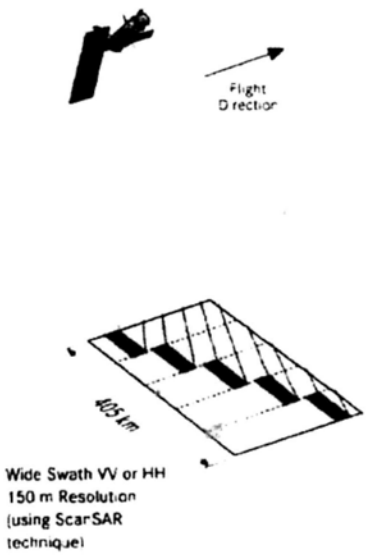

Figure 3.4 Wide Swath Mode (Refer to (*European Space Agency, 2002*)).

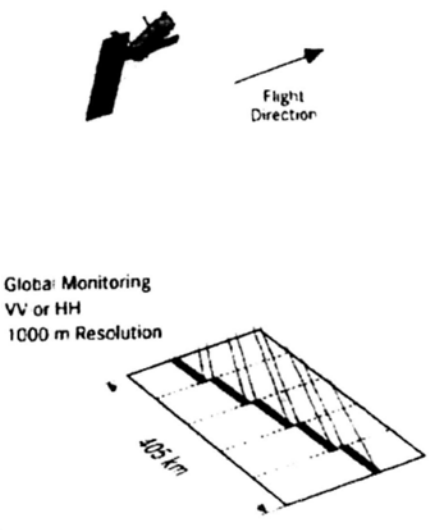

Figure 3.5 Global Monitoring Mode (Refer to (*European Space Agency, 2002*)).

These four modes may be operated in one of two polarizations, either HH or VV

(the letter first indicates the polarization of the transmit signal H for horizontal, V for vertical and the second the polarization of the received signal).

The Alternating Polarization Mode provides two simultaneous images from the same area in HH and VV polarizations, HH and HV or VV and VH, with the same imaging geometry as the IM and similarly high spatial resolution.

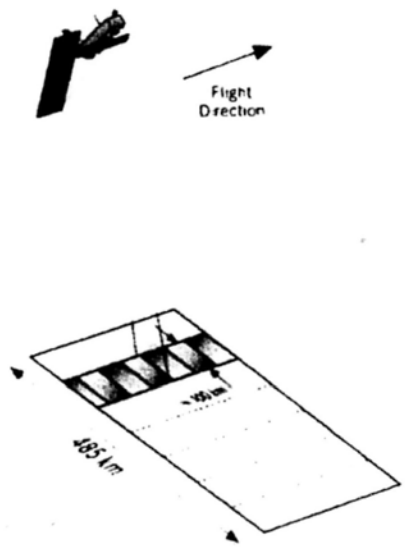

Figure 3.6 Alternating Polarization Mode (Refer to (*European Space Agency, 2002*)).

3.2 SAR data pre-processing

The SAR data used in this study are all raw data (also referred to as level 0) received by the Chinese University of Hong Kong Satellite Remote Sensing Receiving Station. The station covers over 2,500 km radius circular area centered at Hong Kong. It covers Korea and southern part of Japan in the east, eastern India Ocean in the west, Jilin

province in the north, and part of Indonesia in the south (Shown in Fig. 3.7). By capturing and processing satellite-sourced remote sensing data, the Station can provide useful information that is useful to Hong Kong, South China and neighboring regions. It will be useful in monitoring the environment and natural disasters including landslides, subsidence, earthquakes, tsunamis, floods and typhoons, thereby reducing the risk of civilian casualties and economic loss.

Figure 3.7 Coverage of the satellite remote sensing ground receiving station of the Chinese University of Hong Kong.

I use Gamma software to generate Single Look Complex (SLC) format (also referred to as level 1) from raw data (*Gamma Remote Sensing. GAMMA Software Documentation, 2006*). The Gamma Modular SAR Processor allows for accurate range-Doppler algorithms, radiometric calibration to perform basic data conditioning and preserves the phase for interferometric processing. The flow chart of this pre-processing is shown below.

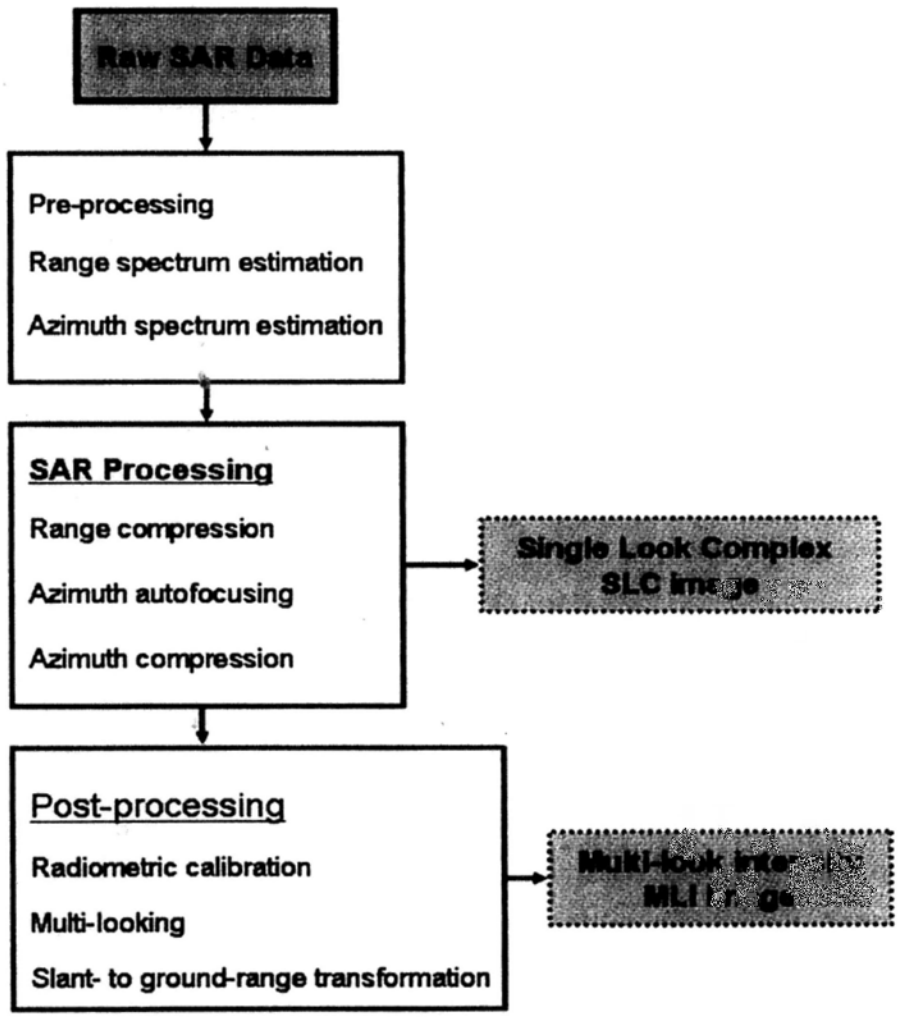

Figure 3.8 SAR pre-processing flowchart (*Gamma Remote Sensing. GAMMA*

Software Documentation, 2006).

Fig. 3.9 shows an example of ENVISAT ASAR intensity image of Guangzhou area. Fig. 3.10 is 1 by 5 multi-looked intensity image of the same area. The region in blue rectangle is the urban area of Guangzhou city which is one of our study areas. Fig. 3.11 shows an example of ENVISAT ASAR intensity image of Hong Kong. Fig. 3.12 is 1 by 5 multi-looked intensity image of the same area. The region in blue rectangle is the Hong Kong International Airport which is one of our study areas.

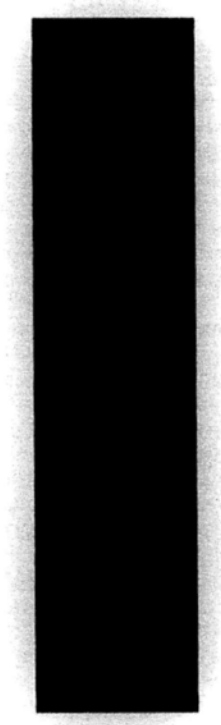

Figure 3.9 Intensity image of Guangzhou

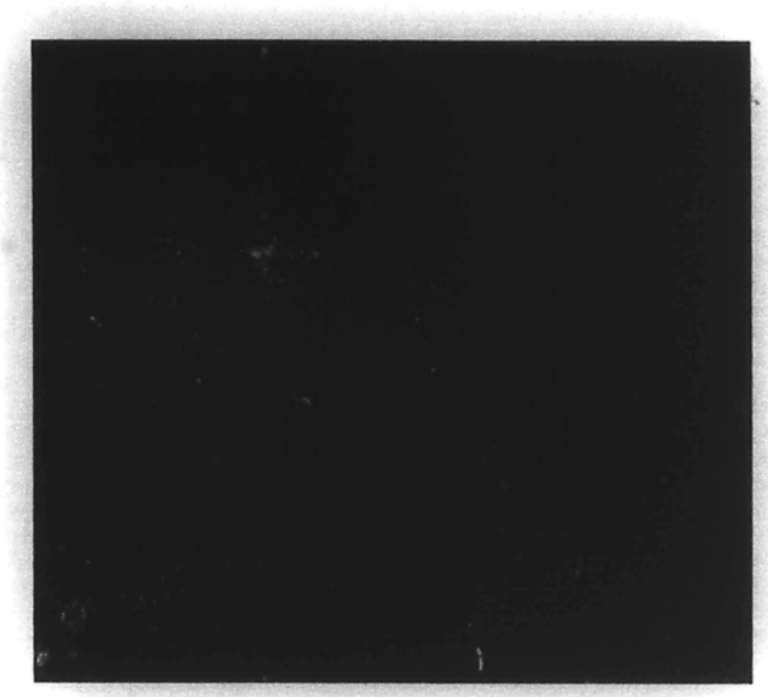

Figure 3.10 1 by 5 multi-looked intensity image of Guangzhou

Figure 3.11 Intensity image of Hong Kong

Figure 3.12 1 by 5 multi-looked intensity image of HKIA.

Chapter 4. Development of InSAR Interpretation Methods

As mentioned in Section 1, InSAR technology is potentially to be used as a powerful tool for large-scale ground deformation monitoring. The previous investigators have shown that InSAR technology is capable of detecting terrain deformation with a millimetric accuracy, and an InSAR derived ground deformation map may contain rich information of local ground subsidence or rising with a horizontal resolution as high as 10-20 m. However, any results or products generated by any InSAR algorithms, models, or software can be treated as raw data only. This is because, like all measurement technologies, InSAR measurements also contain errors and biases induced by temporal and geometrical decorrelation and atmospheric inhomogeneities of the pair of SAR images used for interferometric calculation. These errors or biases should be estimated and corrected as possible. Moreover, even all these corrections are done; an InSAR interferometric image still cannot automatically give us all answers we want. Specified data and information from such an image with suitable methods should be extracted. This

process is called "thematic mapping", as the users do for the use of other satellite images. Therefore, InSAR interpretation technologies and methods aimed to solve these problems must be developed. This chapter will summarize the InSAR interpretation methods I have developed for my dissertation research.

4.1 Calibration and validation of InSAR-derived ground deformation rate

As mentioned above, like all measurement technologies, InSAR measurements also contain errors and biases. These errors and systematic biases may be induced by various causes and different mechanisms, including limitations of InSAR algorithms, models, and software to be used. However, it is hard to estimate and correct these errors and biases by theoretical analysis and calculation only. One shortcut, which the earlier studies used to estimate and correct these errors and biases, is to validate InSAR-detected ground deformation with simultaneously or near-simultaneously field-measured ground deformation data and to use field data as ground truth to correct the InSAR derived values (*Ge, et. al., 2007; Liu, et. al., 2001; Ferretti, et. al., 2007*). After this procedure is done, the InSAR-detected data will be ready to be used for further analysis and interpretation; in particular, in the case of high measurement accuracy is required, such as detection of ground deformation rate of Hong Kong International Airport (HKIA). For these purposes, the following work has been done.

4.1.1 Time series analysis

In HKIA ground deformation monitoring research, the InSAR PSI technology (Gama software) and ENVISAT ASAR images are used for detection of residual settlement at HKIA with a reclaimed foundation. The PSI technology has an important capacity to generate a time series of ground deformation data. One of the validation methods for PSI-detected ground settlement data is comparing them with simultaneously measured ground truth data. In this research, four point targets coded 32524, 32816, 32672, and 33055 (as marked in Fig. 7.13) are chosen for the validation. The results obtained at point target 32524 are shown in Fig. 4.1 as an example (results at other three point targets, which in fact show similar curves, will be given in Chapter 7). From the curves one can see two major features. 1) The two data sets show the same trend. One can see that the ground subsided quite quickly from March 2006 to March 2007 at an annual rate of 4.5 mma^{-1}. After that, the data sets show that the ground was basically in a stable status. 2) The curves show that the magnitudes of PSI-detected ground subsidence and the slopes of the curve are smaller than the ground truth data. This implies that there are systematic biases between the two data sets. These systematic biases must be corrected if the PSI-detected ground subsidence data are used for operational or research purposes.

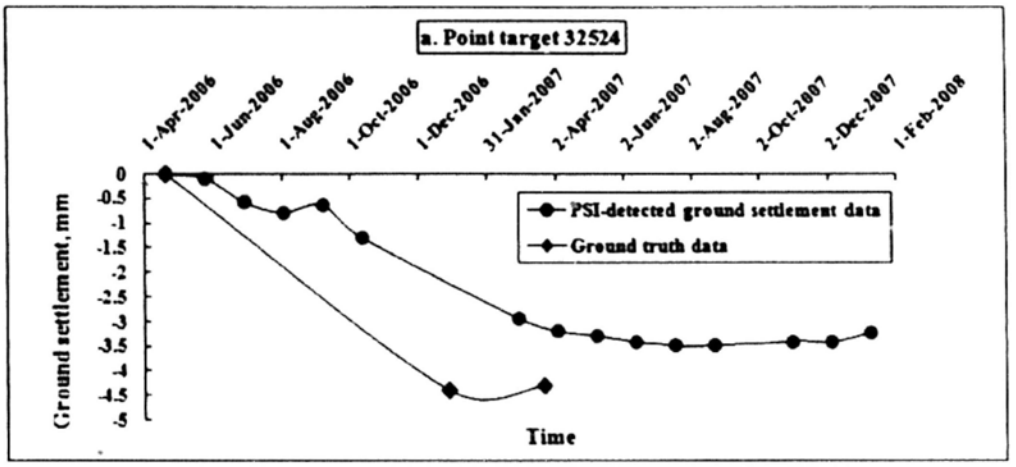

Figure 4.1 Time series of ground settlement process at point target 32524 of HKIA. Dots represent the ASAR-PSI detected ground settlement data, and diamonds represent the simultaneously measured ground truth data.

4.1.2 Regression analysis

I use a correlation analysis method to determine the systematic biases found in comparison of time series data as described above. An ASAR PSI-detected ground deformation rate (H_a, hereafter) data set of HKIA from 2006 to 2008 has been obtained. Before further analysis can be carried out, this data set must be simultaneously or near-simultaneously validated against field-measured ground deformation rates (H, hereafter) data to estimate the accuracy and potential systematic biases. Fig. 4.2 shows a comparison of the two data sets. For convenience the ground subsidence is defined as the positive deformation values in this figure. From these data points, a linear regression function with a correlation coefficient (R^2) of 0.8284 is obtained

$$H_a = 0.6559H - 0.4145. \tag{4.1}$$

This function shows a systematic bias in H_a data set with respect to H data set. The slope of the straight line, 0.6559, is smaller than 1, implying that the ASAR PSI-detected ground deformation values systematically underestimate the real ground deformation represented by the ground truth data set. The potential causes of this systematic bias may be discussed in Chapter 7. The straight line represents a linear regression line.

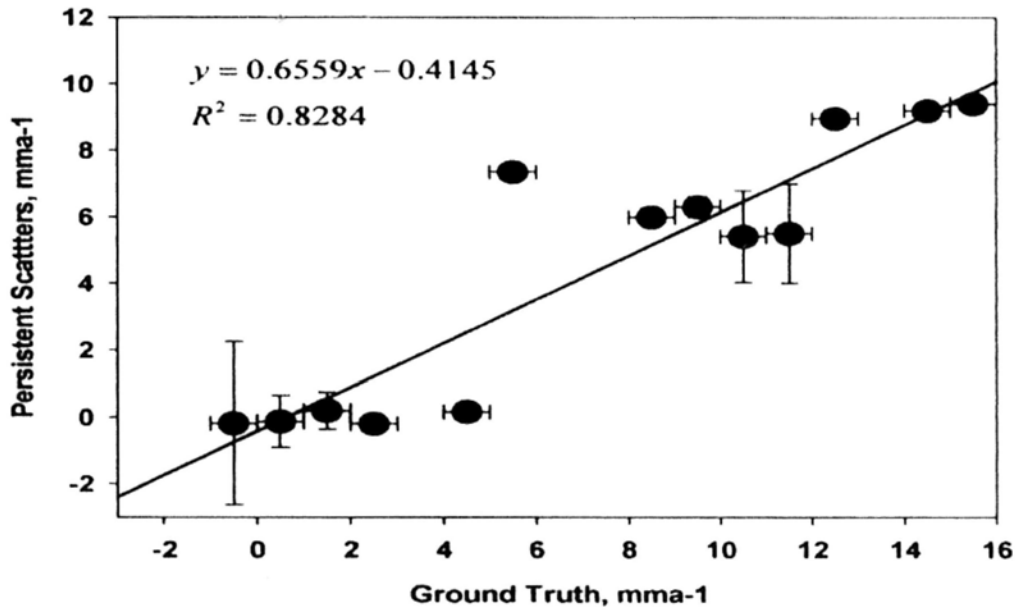

Figure 4.2 Comparison of ASAR PSI-detected ground deformation data set of HKIA from 2006 to 2008 with simultaneous or near-simultaneous ground truth data. Here ground subsidence is defined as the positive deformation rate values. The strait line is a linear regression of the data.

4.1.3 Derivation of an empirical correction model

From the linear regression function (4.1), a correction model is derived as

$$H = 1.52(H_a + 0.4145), \tag{4.2}$$

where H and H_a take positive values for ground subsidence rates (in mma^{-1}). This relationship has been used to correct the ASAR PSI-detected ground deformation rates data set for further analysis in HKIA ground deformation monitoring research.

4.2 Statistical analysis

The statistical methods are used to analyze the general distribution features of InSAR-derived ground deformation rate data in HKIA ground deformation monitoring research. As shown in Fig. 4.3, a Gaussian distribution or normal distribution in the form of

$$f(x) = ae^{-\left[\frac{x-b}{\sqrt{2}\sigma}\right]^2} \tag{4.3}$$

is used to fit the data points. The parameters (with 95% confidence bounds) in (4.3) are determined as a = 126.2 (115.5, 137) mma^{-1}, b = -2.433 (-3.08, -1.786) mma^{-1}, and σ= 6.585 (5.938, 7.234) mma^{-1}, respectively. Goodness of fit, R-square, is 0.8918, implying that the Gaussian distribution gives a very good description of major statistical features of ground deformation rates in HKIA.

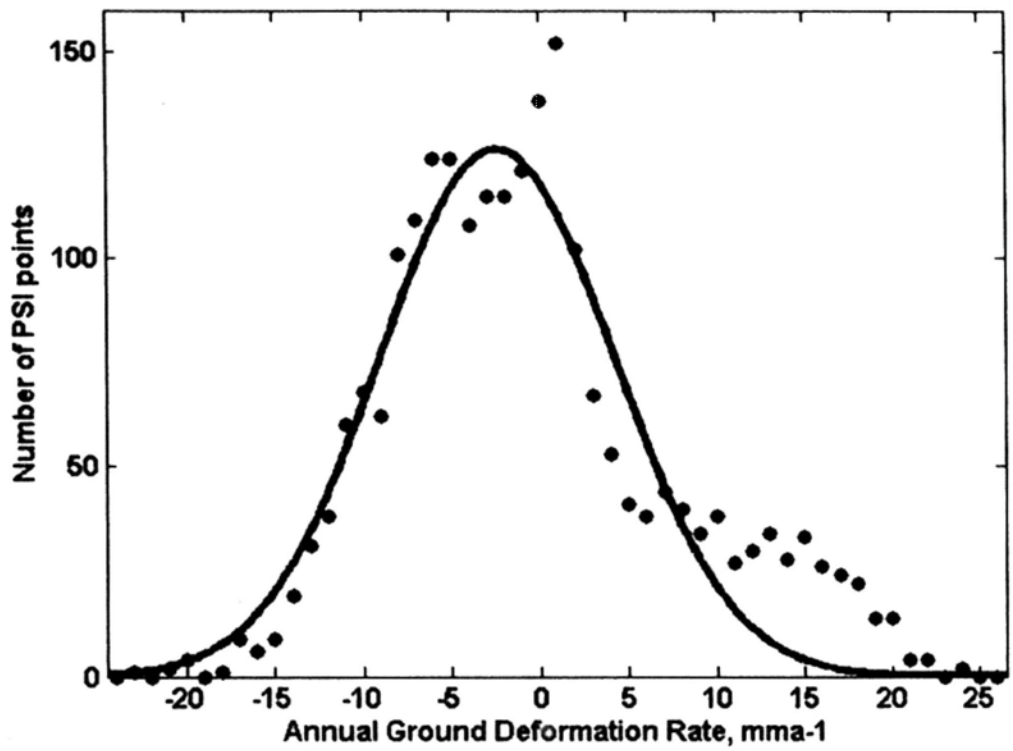

Figure 4.3 Statistical distribution features of ground deformation in HKIA. The vertical axis represents the numbers of data points, and the horizontal axis represents the annual ground deformation rates in mma^{-1}, rising positive. The curve represents a Gaussian distribution function.

From Fig. 4.3, one can see that the number of point targets with subsidence value is 54.5% of the total, that of rising is 39.3% of the total, and that of unchanged ground is 6.1% of the total. The peak of the Gaussian distribution is located at -2.433 mma^{-1} and the number of data points is 5.11% of the total, implying that the general statistical trend of ground deformation in HKIA is toward subsidence.

Furthermore, from Fig. 4.3 one can see a systematic bias on the positive

deformation side. There appears to be a secondary peak at around 14 mma^{-1}. Thus a Lorentz distribution function in the form of

$$f(x) = a_1 e^{-\left[x-b_1 / \sqrt{2}\sigma_1 \right]^2} + a_2 e^{-\left[x-b_2 / \sqrt{2}\sigma_2 \right]^2} \tag{4.4}$$

is used to fit the ASAR PSI-detected ground deformation data. The results are shown in Fig. 4.4 Goodness of fit, R-square, is 0.9472, which is higher than that of a single Gaussian distribution fit. The major peak is located at -2.811 mma^{-1} (b_1) and the minor at 14.11 mma^{-1} (b_2). The mechanisms for formation of this Lorentz distribution of ground deformation will be examined in Chapter 7.

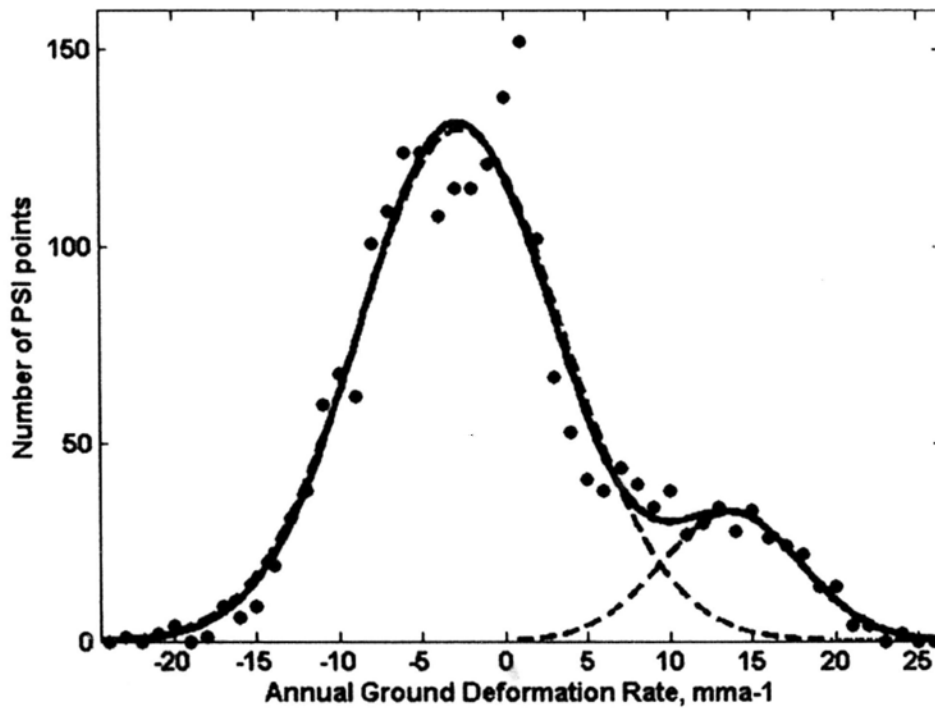

Figure 4.4 A Lorentz distribution fit to the annual ground deformation rates in HKIA.

4.3 Thematic mapping methods

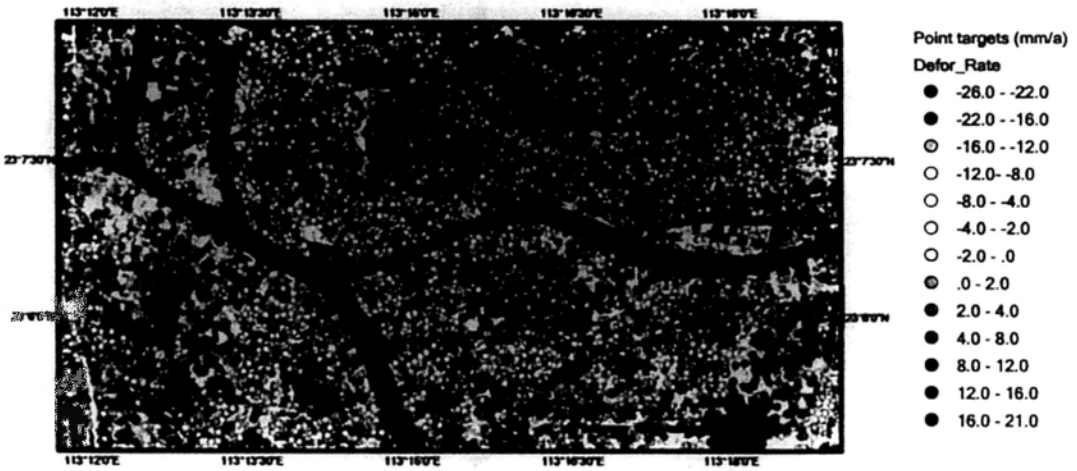

Figure 4.5 A ground deformation rate map of IPTA-derived point targets in Guangzhou using ASAR data. Deformation rates are color-coded, as shown on the right-hand side. (The background image is Landsat TM false color composite image. The spatial resolution is 30 m.)

As above mentioned, an InSAR interferometric image cannot automatically give us the special information we need. We should extract specified data and information from such an image with suitable thematic mapping methods. Fig. 4.5 shows an example of ground deformation rate map of IPTA-derived point targets in Guangzhou using ASAR data.

From Fig. 4.5, One can see that the data points are unevenly but densely distributed over the study area. A total number of 21,265 point targets are detected. The average

density is 150 points km^{-2}. Obviously, this map contains rich information on the ground deformation in the study area, such as the maximum subsidence rate of -26 to -20 mma^{-1}, and the maximum rise rate of 16–21 mma^{-1}. However, the map is a comprehensive one, with all information mixed together. In order to extract specified data and information we need, further processing and interpretation, including thematic mapping, are necessary. Fig. 4.6 shows the idea and procedures for thematic mapping. The products of thematic mapping will contain the specially required data and information, and be used for further interpretation.

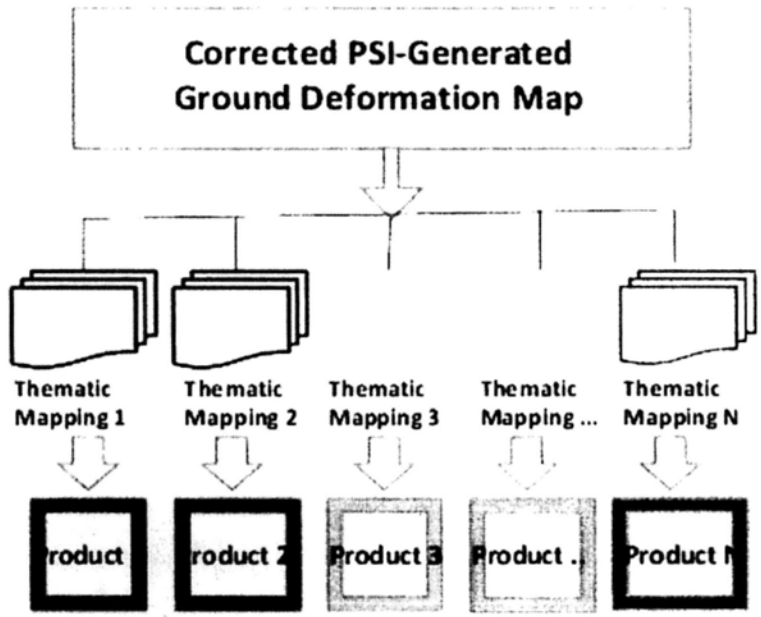

Figure 4.6 Idea and procedures for thematic mapping.

4.3.1 Great value filtering

Great value filtering is one of thematic mapping methods I developed. In order to

obtain active deformation zones from the ground deformation map, a great value filter is used to extract characteristic points with great values. I define an area with a ground deformation rate, subsidence or rise, greater than 10 mma^{-1} as an active ground deformation zone. Five steps of the great value filter can be as follows:

Step 1: The ground deformation rate map is divided into 200 m × 200 m grids.

Step 2: Statistics of the number of points is done with great values, subsidence or rise, in each grid.

Step 3: Average, maximum, minimum, median, and standard deviation values are calculated in each grid.

Step 4: A new point in each grid is defined.

Step 5: Points with great values are selected.

Based on the ground deformation rate maps of the study area derived from ASAR-PSI technology and great value filtering, thematic maps of active subsidence zones are generated. Fig. 4.7 shows a superposition of active subsidence points in Guangzhou urban area generated with great value filtering methods on the sedimentation boundaries of local geology map.

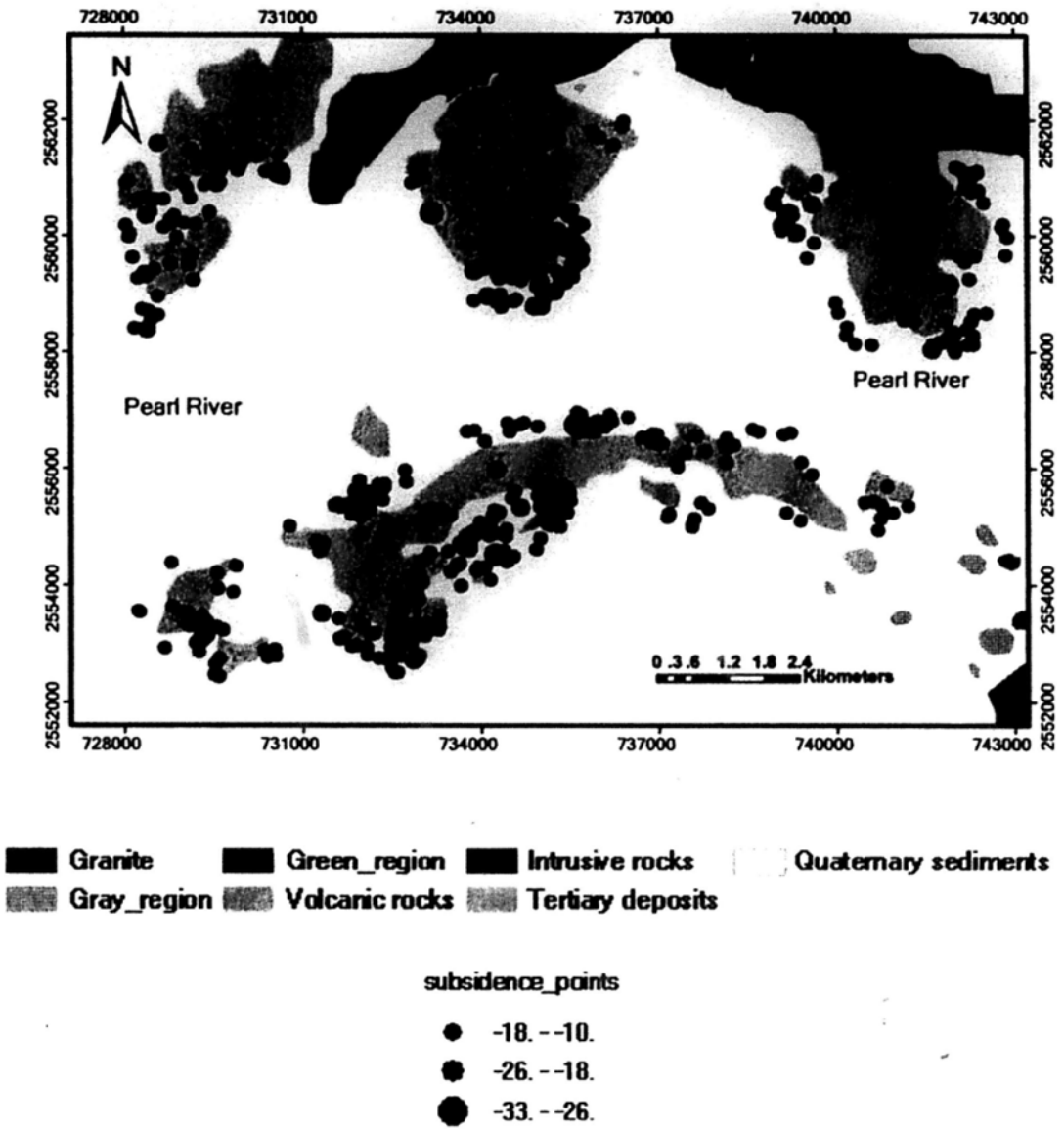

Figure 4.7 Interpretation map of the relationship between active subsidence zones and the sedimentation boundaries

From Fig. 4.7, one can see that four active subsidence zones shown as ASAR-PSI detected great value point targets in Guangzhou urban area. All the four zones are distributed on sedimentation boundaries shown on the local geology map. Three of the active subsidence zones are located on the north side of the Pearl River. The two kinds of

sediments are Quaternary sediments (shown with gray color) and Tertiary deposits (light brown). The porosities of the two kinds of sediments are different. Geologically, subsidence zones are usually distributed on the boundaries of sedimentations. Our results are consistent with these natural characteristics.

4.3.2 Clustering

Another thematic mapping method I developed is a clustering method, i.e., grouping the ASAR-PSI detected point targets into different categories according to their values or signs, then analyzing their spatial distribution features. According to the Gaussian distribution curve of the ground deformation rates and an estimated average deformation rate for the crust of 5 mma^{-1} (*Zhao, et al., 2009a*), the ground deformation rates in HKIA may further be divided into subareas. For example: category 1, stable state, which is defined as a deformation rate falling within a range of $[-\sigma \leq H \leq +\sigma]$; category 2, continuous settlement state, which is defined as a deformation rate falling in two ranges of $[H \leq -\sigma]$ and $[+\sigma \leq H]$, or three or more categories. Further calculations indicate that the number of data points of Category 1 (stable) is 1375, occupying 61.1% of the total, and Category 2 (continuous stable state) is 875 or 38.9% of the total. This implies that the majority of detected points (61.1%) are in a stable state with absolute ground deformation rates smaller than 6.6 mma^{-1}.

A distribution map of three categories of ground stabilities is shown in Fig. 4.8. According to the PSI point density of different stability category, the airport can

generally be divided into sub-areas. The green circle (top right) shows an area with stable PSI points dominant (stable area). This is the Passenger Terminal Building area. Another green circle, on the lower part of the map, shows a second area with PSI dominant (except for several unstable points in the middle). This is the Southern Runway area. The yellow points are near-stable points. The unstable PSI points are concentrated at upper middle area of the map and are marked within a red circle. This is the Midfield of the airport. There are sparsely distributed PSI points in the Northern Runway area and along the central northern edge, but their quantity is statistically not significant enough to determine the stability category of that area.

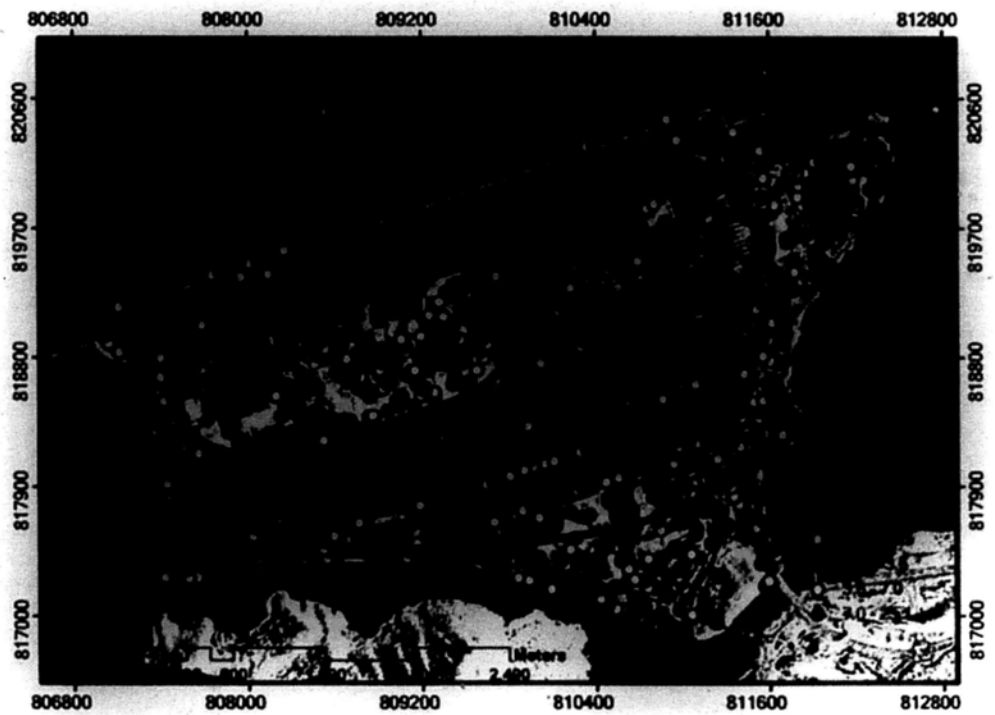

Figure 4.8 A map of ground stabilities of HKIA. The color-coded points are ASAR PSI points. Green, yellow, and red points represent stable, near-stable, and unstable status, respectively.

Chapter 5. A Case Study of Ground Deformation in Guangzhou Urban Area

5.1 Introduction

Previous investigators have pointed out that the ground subsidence is a major geological hazard in the coastal cities in China (*The Ministry of Land and Resources, 2007*; *He, et al., 2006*). The causes of this hazard are quite complicated, but can be loosely divided into two categories: natural subsidence and the human-induced subsidence. The natural subsidence mainly includes deformation of soft soil, and Karst geomorphologic collapse, while the human-induced subsidence results from over-pumping of underground water, land reclamation, underground mining, and concentrated construction (*Xue, et al., 2006; Ding, et al., 2004; Liu, et al., 2005*).

Guangzhou city, the study area of this work, is a mega-city and a major industrial development center in South China. In recent years, the development of this city has

severely been hampered by problems induced by ground subsidence. Investigations indicate that the main factors causing ground subsidence in Guangzhou include natural factors, such as Karst geomorphologic collapse, and deformation of soft soil, and human activities, particularly activities such as over-pumping underground water from the groundwater supply source located in the Karst geomorphologic structure and subway construction (*Liu, et al., 2005; Fang, 2005; Liu, et al., 2007*) Thus, development of new technology for accurate and dynamic detecting of ground subsidence in the Guangzhou urban area is of significance for engineering design, city development zoning, and decision-making.

In this chapter, the Interferometric Point Target Analysis (IPTA) technique, a PSI technique, is used to investigate ground deformation in the urban areas of Guangzhou city, which is located at the Pearl River Delta in South China. A time series of ENVISAT (European Space Agency satellite) ASAR images, taken from 19 March 2007 to 12 May 2008, are used to generate ground deformation fields and interpretation maps in the study area. The derived ground subsidence data are then compared with reported ground observation results and analyzed in detail. The mechanisms for causing the ground subsidence in Guangzhou urban area are also analyzed. This work is also a demonstration study for evaluating the general performance of the applied PSI technique in detecting ground subsidence with limited SAR images.

5.2 Study area

Guangzhou city, the study area of this work, is the capital of Guangdong province in South China. The land area of Guangzhou city is 7,434.4 km^2 and the recorded population at the end of 2006 was 9,754,600, making it the third most important metropolitan area in China (*http://en.wikipedia.org/wiki/Guangzhou*). Guangzhou harbor is an important navigation center in South China, which is connected with the outside world through the waterways of the Pearl River and the South China Sea. Guangzhou is the economic center of South China. In 2007, its GDP reached US $92 billion, ranking Guangzhou 6th among the Chinese cities (*http://en.wikipedia.org/wiki/Guangzhou*). Thus, thousands of construction projects are currently underway or in the planning stages.

Geographically, Guangzhou covers an area from 112°57′ to 114°3′E and from 22°26′ to 23°56′N (see Fig. 5.1). This region is located at the northern margin of the Pearl River Delta. Guangzhou is within a humid subtropical climate zone controlled by the Asian monsoon, which is characterized by wet summers with high temperatures and high humidity and cool dry winters. The mean annual temperature is 22.8°C. The average annual precipitation can reach 1,982.7 mm, concentrated in the flood season from April to October with frequently occurring typhoon and rainstorm landfalls. Generally, in the wet season, the underground water table rises and the flow rate increases. Dissolution becomes stronger. The collapse of Karst-cave roofs is common. After the wet season, the underground water table decreases. The Karst-cave roofs can also collapse due to the effects of gravity. Thus, the high annual precipitation rate and uneven annual precipitation

distribution constitute a significant mechanism for ground collapse in the Karst geomorphologic areas (*Liu, et al., 2005*).

The landform of Guangzhou city corresponds to hilly country, with altitudes of about 200–1,000 m. The north terrain is higher than the south (*Liu, et al., 2005*). The urban area of Guangzhou is located in the Guangdong Depression Belt of the South China fold system. There are more than 40 faults and 30 folds. The Guangzhou-Sanshui fault and Guangzhou-Conghua fault divide the city into three sub-geological structure units: Guangzhou-Huadu fault basin, Zengcheng salient, and the Pearl River Delta Depression (*Liu, et al., 2005*). These large-scale structures constitute potential causes of ground surface deformation.

The northern and western portions of Guangzhou city, belonging to Guangzhou-Huadu fault basin, are rich in huge limestone. Thus, the limestone corrosion fractures and the Karst caves are gestated there. The depth of silt layer in the Pearl River Delta reaches about 15–40 m. This kind of soft soil, with high compressibility, lower permeability and bearing capacity, easily leads to ground deformation damage, thixotropic flow, foundation sinking, sand liquefaction, and seismic subsidence (*Fa and Huang, 1995; Zhi, et al., 2001, Zhang and Wei, 2003*).

117°0'0"E
114°0'0"E
111°0'0"E
24°0'0"N
21°0'0"N
Guangdong
Guangzhou
South China Sea
220 Kilometers
220 110 0
China
Guangdong

(a)

(b)

Figure 5.1 (a) Location of study area in Guangdong Province. (b) Map of study area. Active faults are marked in red (partially referred to (*Liu, et al., 2005; http://en.wikipedia.org/wiki/Guangzhou)*).

5.3 ASAR data and data pre-processing

The satellite SAR images taken by ENVISAT satellite constitute a baseline for this work. ENVISAT satellite is an advanced polar-orbiting earth observation satellite launched by the European Space Agency in March 2002. The ASAR instrument on board the ENVISAT operating at C-band ensures continuity with the image mode (SAR) and the wave mode of the ERS-1/2 Active Microwave Instrument (AMI). It features enhanced capability in terms of coverage, range of incidence angles, polarization and modes of operation (*http://envisat.esa.int/ handbooks/asar/CNTR.htm*).

All the ASAR images used in this work were acquired at the Hong Kong Remote Sensing Ground Receiving Station, which was established at the Chinese University of Hong Kong in 2006. The antenna of the receiving station covers a circular area with a radius of over 2,500 km centered in Hong Kong. Our study area is near Hong Kong, so that it is located near the center of circular coverage of the antenna. This work uses 10 images of Image Mode raw data taken from March 19, 2007 to May 12, 2008 as listed in Table 6.1, which have been pre-processed at the receiving station before delivering to the users. Images taken between December 24, 2007 and May 12, 2008 are not included in our study, since they were acquired with alternative polarization mode.

Table 5.1 Image Mode ASAR Data used in this study.

No.	Acquisition Date (yyyymmdd)	Orbit No.
1	20070319	26403
2	20070422	26904
3	20070528	27405
4	20070702	27906
5	20070806	28407
6	20070910	28908
7	20071015	29409
8	20071119	29910
9	20071224	30411
10	20080512	32415

The images listed in Table 5.1 are single look complex (SLC) image products generated from raw ASAR data, which are geometrically corrected. The images have also been radiometrically calibrated using Gamma software (*http://www.gamma-rs.ch/gamma.html*).

5.4 Field observed ground deformation

Previous investigations indicated that in Guangzhou area ground subsidence and ground collapse may occur anytime throughout the year. The frequency has steadily increased continuously in recent years, mainly due to over-pumping of underground water to satisfy the need for drinking water and water for industrial uses. The peak phase of occurrence frequency of serious events lasts from April to August. In this local spring-summer rainy season, the groundwater level rises significantly. It becomes the main factor causing covered Karst collapse. The regional distribution of ground collapse and ground subsidence in Guangzhou city is shown in Fig. 5.2. One can see that ground subsidence is mainly distributed in the urban area of Guangzhou city and that ground collapse mainly occurs in the Guangzhou-Huadu basin.

Figure 5.2 Distribution of ground collapse and ground subsidence in Guangzhou City (partially referred to (*Liu, et al., 2005*)).

The spatial distribution of main ground collapse accidents occurring from 2007 to 2008 is shown in Fig. 5.3. These accidents are mainly distributed along the underground metro-lines around Datansha Island in Liwan District in the southwest of Guangzhou city. The related information of six ground collapse events coded in Fig. 5.3 is listed in Table 5.2(*http://news.163.com/08/0301/08/45UG8VE700011229.html;http://news.sina.com.cn/o/2008-01-18/144213285387s.shtml;http://news.sohu.com/20071006/n252487281.shtml;*

http://news.boxun.com/news/gb/misc/2008/01/200801241131.shtml;http://www.gd.xinhuanet.com/dishi/2008-02/02/content_12388671.htm). Fortunately, the occurrence dates of the accidents were all in the ASAR image receiving time scope (see Table 5.1). This provides a useful opportunity to validate the ground deformation data derived from ASAR images.

Table 5.2 Ground collapse accidents in Guangzhou in 2007–2008 are coded from 1 to 6 in Figure 5.3.

Code	Occurrence time	Location	Scope, x×y×z	DR* mma^{-1}
1	Feb 29, 2008	Huanshixi Road, Liwan	3 m × 1.5 m × 3 m	-15 - -10
2	Jan 31, 2008	Zhongshanba Road	small scope, 30 cm deep	-15 - -10
3	Oct 06, 2007	Duobao Road	300 m^2, ~ 6m deep	-20 - -15
4	Feb 18, 2008	Juncture of Zhongshanba Rd. Nanan Rd and Huangsha Av, Liwan	100 m^2, deepest site over 40m	-20 - -15
5	Jan 23-24, 2008	Datansha Island	200-300 m^2, >3m deep	-15 - -10
6	Feb 02, 2008	Datansha Island	Observable	-15 - -10

*ASAR-derived ground deformation rate (vertical rate)

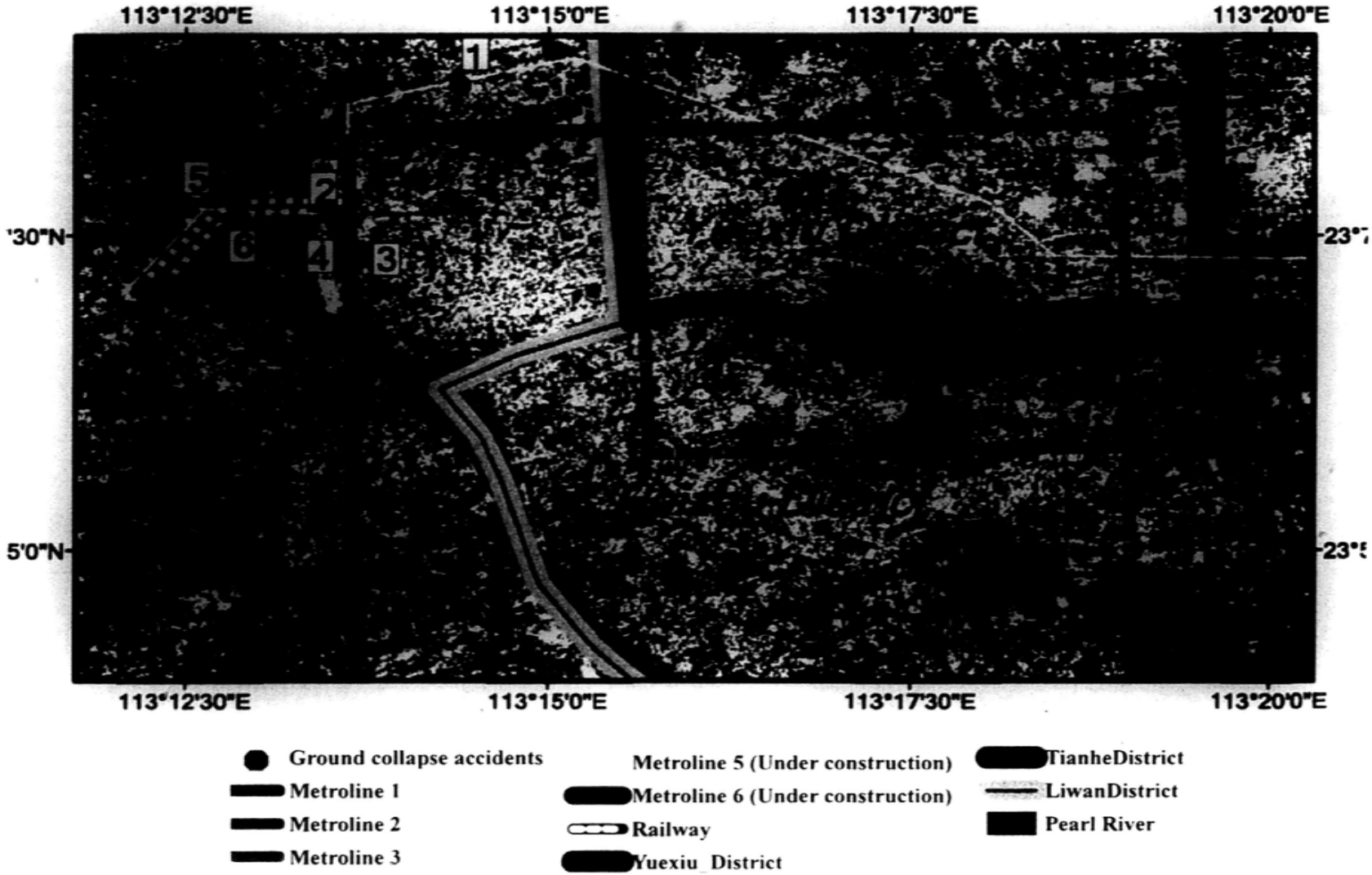

Figure 5.3 The spatial distribution of ground collapse accidents in 2007–2008 are coded from 1 to 6. The underground metro-lines and district boundary lines are also marked. (The background image is an ENVISAT ASAR image.)

5.5 Mapping of ASAR-derived ground deformation

Using the IPTA technique and ASAR data listed in Table 5.1, a ground deformation rate map of the Guangzhou urban area is generated, as shown in Fig. 5.4. One can see that the data points are unevenly but densely distributed over the study area. A total number of 21,265 point targets are detected. The average density is 150 points km^{-2}. The maximum subsidence rate is -26 to -20 mma^{-1}, and the maximum rise rate is 16–21 mma^{-1}. These values are much larger than the normal ground deformation rates induced solely by crustal movements. Gumen and Kissin (*Gumen and Kissin, 1995*) measured an average vertical amplitude of crustal movements in Byelorussia as 4 ± 3 mma^{-1} ranging from 0 to 10 mma^{-1} from 1975 to 1986. Mizouo (*Mizouo, 1967*) gave vertical amplitude of earth crustal movements in Japan as 1–4 mma^{-1} for the wavelength of 20–100 km (a scale of our study area). Therefore, 5 mma^{-1} should be a reasonable estimate for the normal ground deformation rates induced solely by crustal movements. This indicates that the ground deformation rates in the Guangzhou urban area derived from this study are 4–5 times greater than the normal ground deformation rates induced solely by crustal movements, implying that the study area is an extremely active area for ground deformation.

In order to further examine the spatial distribution features of ground deformation in the study area, a contour map is generated using the data in Fig. 5.4 and interpolation technology. The results are shown in Fig. 5.5. From this ground deformation contour map, one can see that all the sites of 6 ground collapse accidents that occurred in 2007–2008,

as listed in Table 5.2, fall within the subsidence areas. The corresponding subsidence rates derived from ASAR images are also listed in Table 2 as a reference. One can see that all the subsidence rates at these 6 sites exceed -10 mma^{-1}, and the maximum value is -20 mma^{-1}. This close correlation relationship indicates that the ASAR-derived ground deformation rates are reasonable, and may be used to reveal the macro-scale features of ground deformation in the study area.

The horizontal resolution of the ground deformation rate contour map is 100 m and the vertical resolution is 2 mma^{-1}. Thus, the map contains rich information on ground deformation, which is important for various users. In order to describe 2-D spatial distribution features of ground deformation in the study area, the connected subsidence (rise) areas are circled by red (blue) ellipses. One can see three major subsidence zones. The largest zone is located in the middle west of the study area, which runs from the north border to the south border and crosses the Pearl River. A high subsidence sub-region with a subsidence rate of -26 mma^{-1} is located in the south of the Pearl River as coded SS1 in the figure. Its area is about 2 km^2. The secondary subsidence zone is located in the east of the study area. Its coverage is a little smaller than the largest one, and also distributed crossing the Pearl River. Within this subsidence zone, there is also a high subsidence sub-region with a subsidence rate of -26 mma^{-1}, which is located in the north of the Pearl River as coded SS2 in the figure. Its area is about 6 km^2. The third subsidence zone is located in the southwest of the study area. Between two subsidence zones, there is always a rise zone with a maximum rise rate of 21 mma^{-1}. In the other

words, the subsidence zones and rise zones are alternately distributed. The horizontal scale of the subsidence - rise patterns is about 5 km. These interesting patterns seem to show that they may be caused from the movement of local geological structure. Of cause, to conclude validation of this hypothesis, however, requires further evidence and examination.

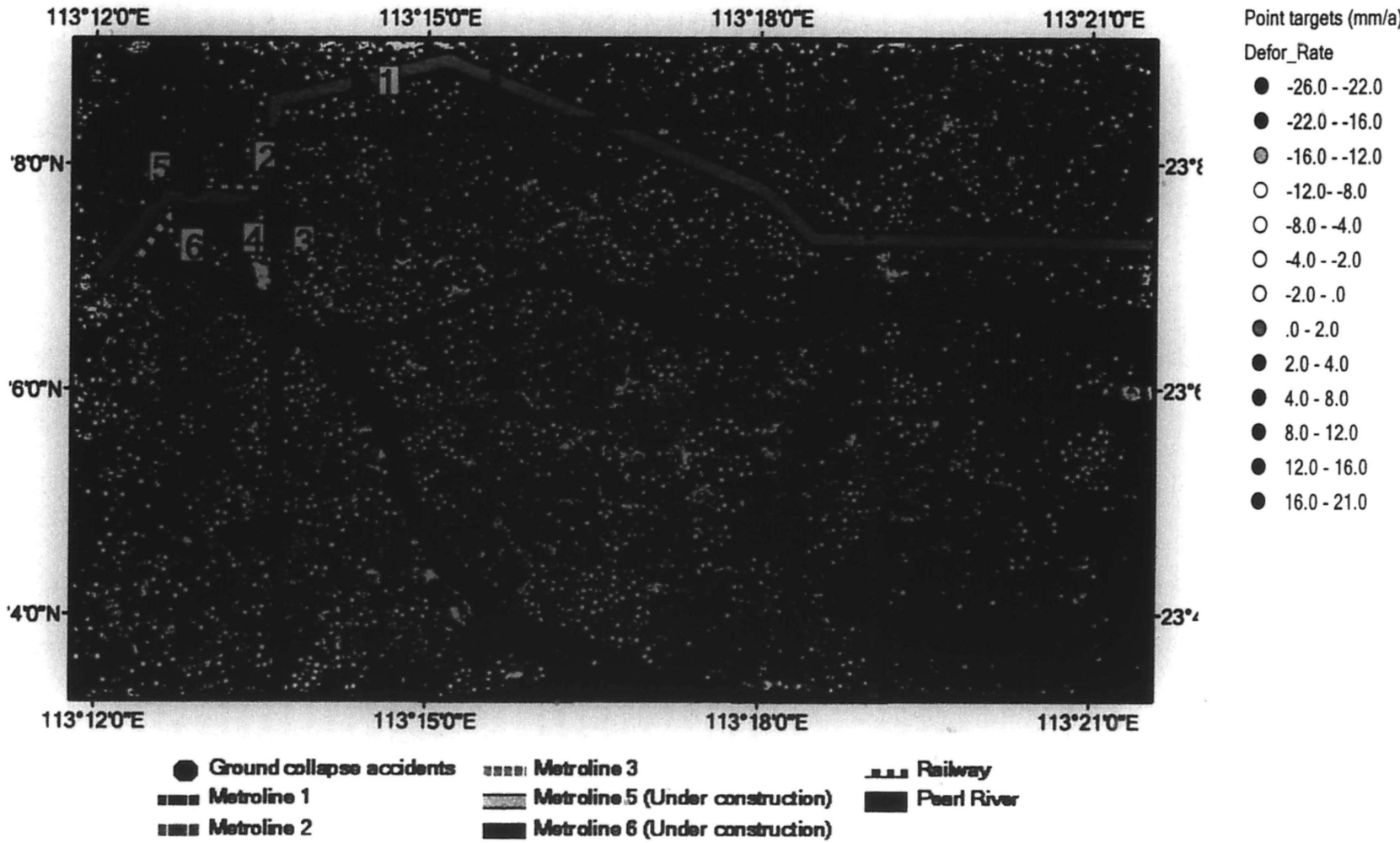

Figure 5.4 A ground deformation rate map of IPTA-derived point targets in Guangzhou using ASAR data listed in Table 5.1. Deformation rates are color-coded, as shown on the right-hand side. Numbers 1–6 as marked in Figure 5.3 show the locations of ground collapse accidents that occurred in 2007–2008. (The background image is an ENVISAT ASAR image.)

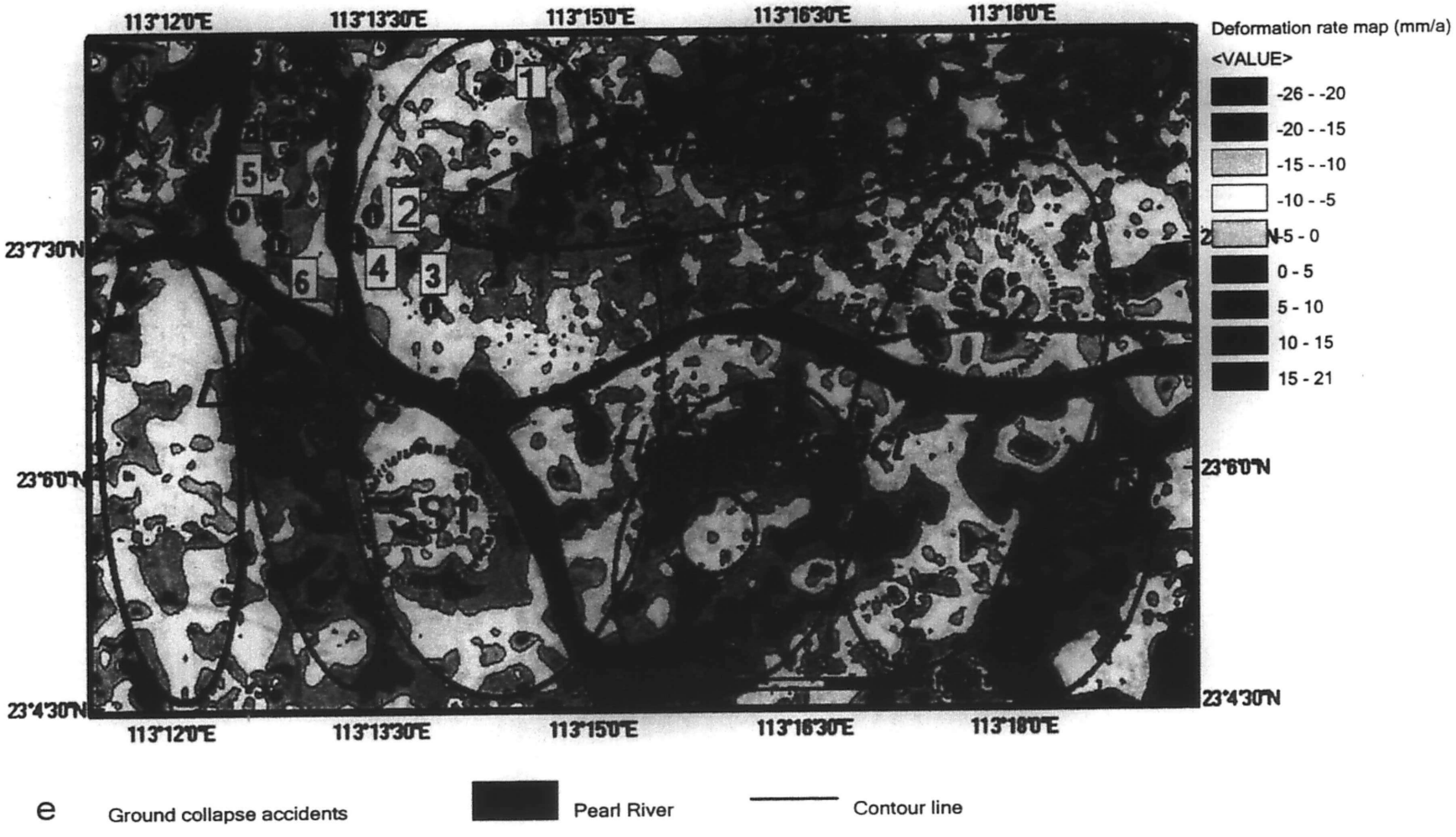

Figure 5.5 A contour map of ground deformation in Guangzhou city.

5.6 Ground subsidence and geological conditions analysis in Datansha Island

Two underground metro-lines under construction in Guangzhou City, Line 5 and Line 6, pass through and intersect in Datansha Island. The island is located in the center of the Pearl River in the northwest of study area as shown in Fig. 5.6. Thus, the island is used as a test site for detecting ground subsidence caused from natural processes and underground engineering projects. Eight point targets distributed along underground metro-lines 5 and 6 in Datansha Island as shown in Fig. 5.6 are used for this purpose. The corresponding ground subsidence rates derived from ASAR images are listed in Table 3. One can see that the mean subsidence rate reaches -19.6 ± 3.1 mma^{-1}, ranging from -13.7 to -23.1 mma^{-1}. These values are 2.7–4.6 times higher than the normal ground deformation rate, ± 5 mma^{-1}. Moreover, all ground collapse accidents that occurred in 2007–2008 were also distributed along underground metro-lines 1, 5, and 6. These facts indicate that Datansha Island area is an active ground subsidence zone. In order to analyze the causes of ground subsidence, the test site is divided into 3 sections according to the geological conditions: section 1 from Jiaokou station to Datansha station, section 2 from Datansha station to Zhongshanba station, and section 3 is the Datansha Island segment of metro-line 6 as shown in Fig. 5.7. Note that underground metro-lines 5 and 6 cross each other at Datansha station.

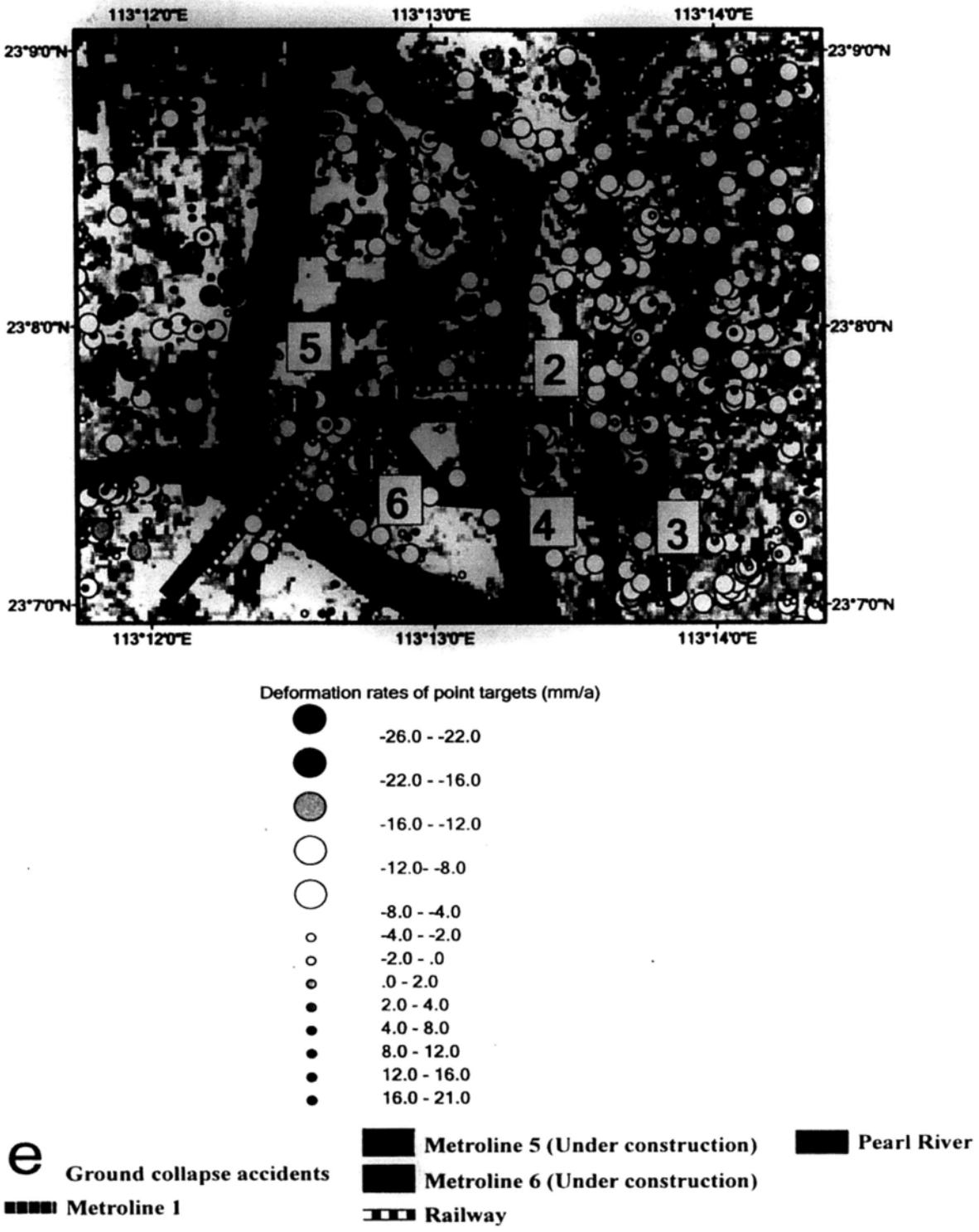

Figure 5.6 An ASAR-derived ground deformation map in Datansha Island area. PT1–PT8 are test sites along metro-lines 5 and 6. Numbers 2–6 are sites of ground collapse accidents occurred in 2007–2008.

Table 5.3 Point targets in Datansha Island.

Metro-line	Point Target	Deformation Rate (mma^{-1})
6	PT1	-22.6
6	PT2	-18.2
6	PT3	-23.1
6	PT4	-22.2
6	PT5	-13.7
5	PT6	-21.4
5	PT7	-17.3
5	PT8	-17.9
	Mean	-19.6 ± 3.1

1) Section 1: from Jiaokou station to Datansha station

Datansha Island is a relatively flat and wide sand bank. This segment of underground metro-line 5 crosses the south portion of the island as shown in Fig. 5.7. In the east of metro-line 5, there is the Inner Ring Road, and the Pearl River Bridge is running over it. From Fig. 5.6, one can see that ground collapse accident 5 occurred

within this section. At point target 7, near ground collapse 5, the subsidence rate is -17.3 mma^{-1}.

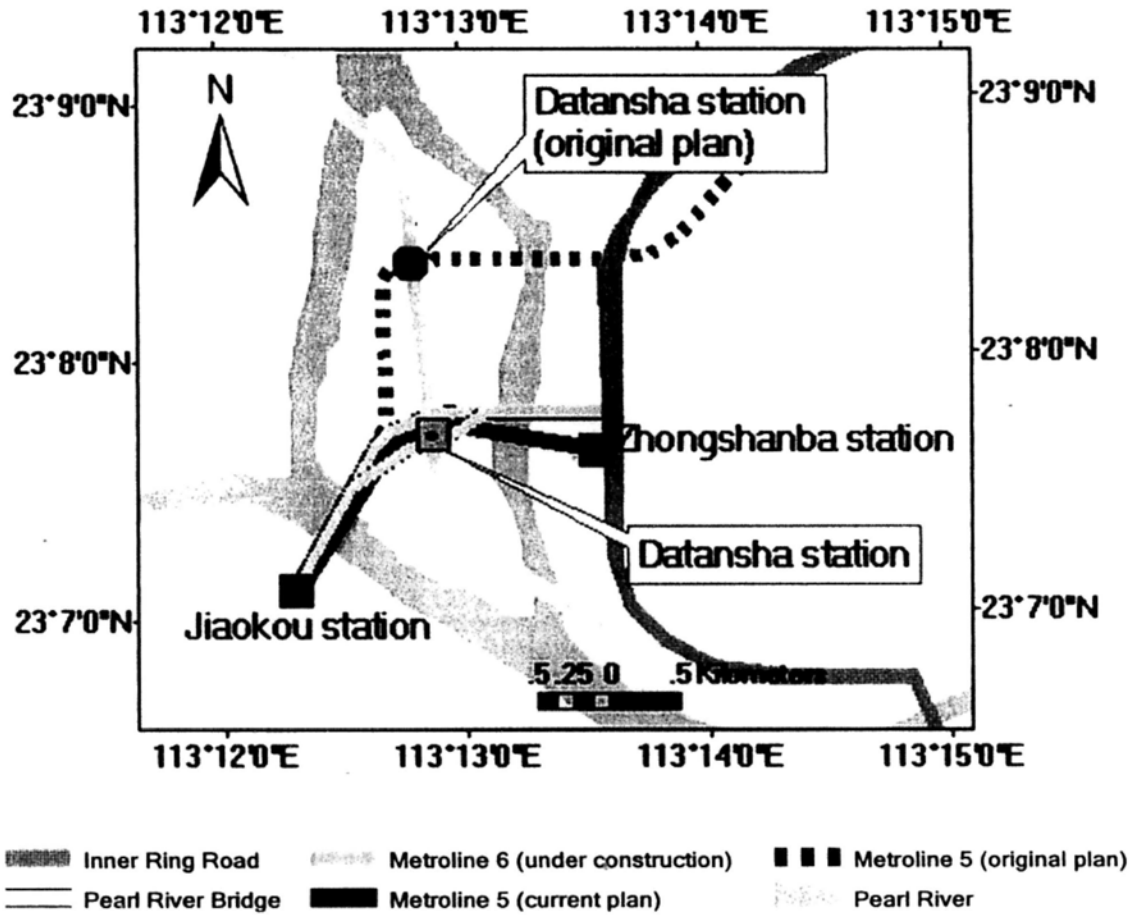

Figure 5.7 Datansha Island area and underground metro-lines (partially referred to (*Liu, 2006*)).

In the feasibility study phase of the underground metro-line project, the original design of metro-line 5 was expected to use the underground line (shown as dashed line in Fig. 5.7). Meanwhile, an open surface method was chosen to construct Datansha station. A shield method was designed to construct the section from Jiaokou station to Datansha station. However, the initial plan was soon abandoned due to the complicated engineering

geological conditions. According to the original design, the Guangzhou-Sanshui fault and metro-line 5 would intersect under the western branch of the Pearl River. Fault breccia is found at Datansha station. Quaternary sandstone is also developed here. The sandstone has strong permeability and the sandstone layer also has direct hydraulic connection with the Pearl River. The bedrock is constituted by cretaceous red sandstone and carboniferous Huanglung limestone. Thus, lithology is complicated. Moreover, Huanglung limestone is well developed here. During the drilling process, a moderately large cave was found, and ground collapse occurred. Thus, all the underground lines west-eastward going through Datansha Island would inevitably pass through limestone. Therefore, the final design of this segment is to build an elevated bridge instead of underground tunnels (*Liu, 2006*).

2) Section 2: from Dantansha station to Zhongshanba station

From Figures 5.6 and 5.7, one can see that ground collapse accidents 2 and 4 occurred within this section. The underground tunnel for metro-line 5 from Datansha station to Zhongshanba station passes through mucky sandstone. The geological condition of some segments is silt layer and moderate coarse sandstone. The bottom of the tunnel passes through sedentary rock and strata. The shortest distance from the roof of tunnel to the bottom of Pearl River is about 5 m. The average water content of silt layer is 63.90%. Void ratio is 1.71. The average compressibility is 1.42 MPa^{-1}(*Liu, 2006*). Thus, the silt layer is characterized by high water content, high void ratio, high compressibility, low bearing capacity, and low shear strength. The mucky sandstone and moderate coarse sandstone are highly permeable and also have direct hydraulic connection with the Pearl

River.

3) Section 3: Datansha Island segment of metro-line 6

From Figures 5.6 and 5.7, one can see that ground collapse accident 6 occurred at this segment. At point target 8, near accident 6, the ground subsidence rate reaches -17.9 mma^{-1}. Metro-line 6 is designed to pass through Datansha Island from north to south.

The geological condition of Datansha Island is that carboniferous Huanglung strata are mainly distributed there. Limestone Karst caves have developed. Previous investigations showed that the Karst caves are distributed as moniliforme. The maximum height of a single cave reaches up to 21 m. According to the results of the pumping test, Huanglung limestone corrosion fissure and the Karst caves are well developed there. The water permeability coefficient of carbonates corrosion fissure and Karst caves is 112.2–135.5 md^{-1}. The maximum prediction value of water inflow is 608.8–814.7 m^3d^{-1} (*Fang, 2005*).

5.7 Conclusions and Discussion

This study uses IPTA technique and ASAR images acquired in Hong Kong to detect ground deformation in the urban area of Guangzhou city, an important industrial center in South China, which is negatively affected by ground subsidence. The major results are summarized as follows:

1) A ground deformation rate map of Guangzhou urban area with scattered

distribution of point targets is generated with ASAR images acquired in 2007–2008. The maximum subsidence (rise) rate reaches up to -26 to -20 mma^{-1} (16–21 mma^{-1}). These values are 3–5 times larger than the normal ground deformation rate induced solely by crustal movement, implying that the study area is an active zone for ground deformation. This agrees with the results obtained by previous investigations.

2) Based on the point target map, a contour ground deformation rate map of Guangzhou urban area is generated by an interpolation method. The horizontal (vertical) resolution of the contour map is ~ 100 m (2 mma^{-1}). The contour map shows three major subsidence zones located in the middle-west, the east, and the southwest of the study area, respectively. The maximum subsidence rate reaches -26 mma^{-1}. Between two subsidence zones, there is always a rise zone with a maximum rise rate up to 21 mma^{-1}. The horizontal scale of the subsidence - rise patterns is about 5 km. All the sites of six ground collapse accidents that occurred in 2007–2008 fall within the subsidence areas, qualitatively validating the IPTA results.

3) Ground subsidence and geological conditions along metro-lines in Datansha Island are examined as a case study. The analysis indicates that the local geological conditions, such as limestone Karst geomorphology, as well as silt layers characterized by high water content, high void ratio, high compressibility, low bearing capacity and low shear strength, are natural causes for ground subsidence and ground collapse accidents occurring there. Human activities in the form of underground engineering projects constitute another important cause.

This study gives the quantitative data of ground deformation in the Guangzhou urban area. It is necessary to have a precision assessment for these results and for the technique used. Although there are not simultaneous leveling data available for a point-to-point comparison with IPTA ground deformation measurements, the results of case study of Datansha Island indicate that the IPTA-derived ground subsidence rates qualitatively coincide with field observations of ground collapse events. On the other hand, in a parallel research project, the IPTA technique is applied for monitoring ground stability in Hong Kong International Airport (HKIA). For that project, there are simultaneous or near-simultaneous leveling data available for comparison with IPTA/ASAR-derived ground deformation data. Statistical analysis gives a systematical bias of 2 mma^{-1} between the two datasets (IPTA/ASAR method underestimated) with the annual deformation rates ranging from 0.1 to 10.2 mma^{-1}. The correlation coefficient (R^2) between the two datasets is 0.736. These results may serve as a close estimate for a potential precision of IPTA technique used for this study. How many SAR images are really needed for employing IPTA technique? This is another important question. Theoretically, the more, the better, but there is not a hard threshold. Ferretti *et al.* supposed that if the quantity of SAR images is more than 30, the time series of the amplitude values of each pixel can be analyzed for detecting stable scatterers (*Ferretti, et al., 2001*). They used 41 SAR images to estimate ground subsidence in Pomona (*Ferretti, et al., 2000*). For our HKIA project, 15 ASAR images are used to generate ground deformation fields and interpretation maps. As mentioned above, the systematic bias between the field measured and IPTA/ASAR-derived ground deformation rates reaches 2

mma^{-1}. We may say that although this precision is not perfect for all the users, the data are still useful at least for long term trend monitoring. For this project, serving as a demonstration study, only 10 ASAR images with a temporal coverage of one year are available for the use to generate ground deformation fields in the study area. The results indicate that important information on locations of major ground collapse disasters and horizontal distribution features of ground deformation can be extracted from the IPTA/ASAR-derived ground deformation data, demonstrating that the IPTA technique with limited archived SAR data may serve as an efficient tool for monitoring the ground deformation. The availabilities of point-to-point comparison data for the correlation/validation analysis of IPTA/ASAR-derived ground deformation data with field measurements and more SAR images would always be a hope for the future study.

The contour ground deformation rate map of Guangzhou urban area shows alternately distributed patterns of subsidence and rise zones with a horizontal scale of about 5 km. The patterns seem to indicate that they may be caused by the movement of local geological structure. To confirm this point, further evidence and analysis are needed.

Chapter 6. Analysis of Active Ground Subsidence Zones in Guangzhou City based on ASAR-PSI result

In last chapter, IPTA, an improved PSI technology is used to investigate the ground deformation in Guangzhou city. In this chapter, ground subsidence zones will be analyzed based on the ASAR-PSI result. To obtain active subsidence zones from ground deformation map generated by ASAR-PSI technology, a great value filter method is developed to extract characteristic points with great values. Based on the ground deformation rate maps of the study area derived from ASAR-PSI technology and the great value filter, a thematic map of active subsidence zones are generated. For the further analysis and interpretation the distribution mechanisms of active subsidence zones, a local geological map including geological structure, sediments, and rocks information are used to generate a series of thematic maps. I consider that the geological structure, sediment spatial distribution characteristics, over-development, and underground engineering projects may be major mechanisms. Therefore, the relationships between the

distribution of active subsidence zones and these four factors are analyzed. The results show the geological structure, sediment spatial distribution characteristics, over-development, and underground engineering projects may probably be closely associated with the distribution of active subsidence zones.

6.1 Great value filter

In order to obtain active deformation zones from the ground deformation map, a great value filter is used to extract characteristic points with great values. I define an area with a ground deformation rate, subsidence or rise, greater than 10 mma^{-1} as an active ground deformation zone. Five steps of the great value filter can be as follows:

Step 1: The ground deformation rate map is divided into 200m×200m grids.

Step 2: Statistics of the number of points is done with great values, subsidence or rise, in each grid.

Step 3: Average, maximum, minimum, median, and standard deviation values are calculated in each grid.

Step 4: A new point in each grid is defined.

Step 5: Points with great deformation rate values are selected.

Based on the ground deformation rate maps of the study area derived from ASAR-PSI technology and the great value filter, thematic maps of active subsidence zones are generated. The active subsidence zones are analyzed and interpreted.

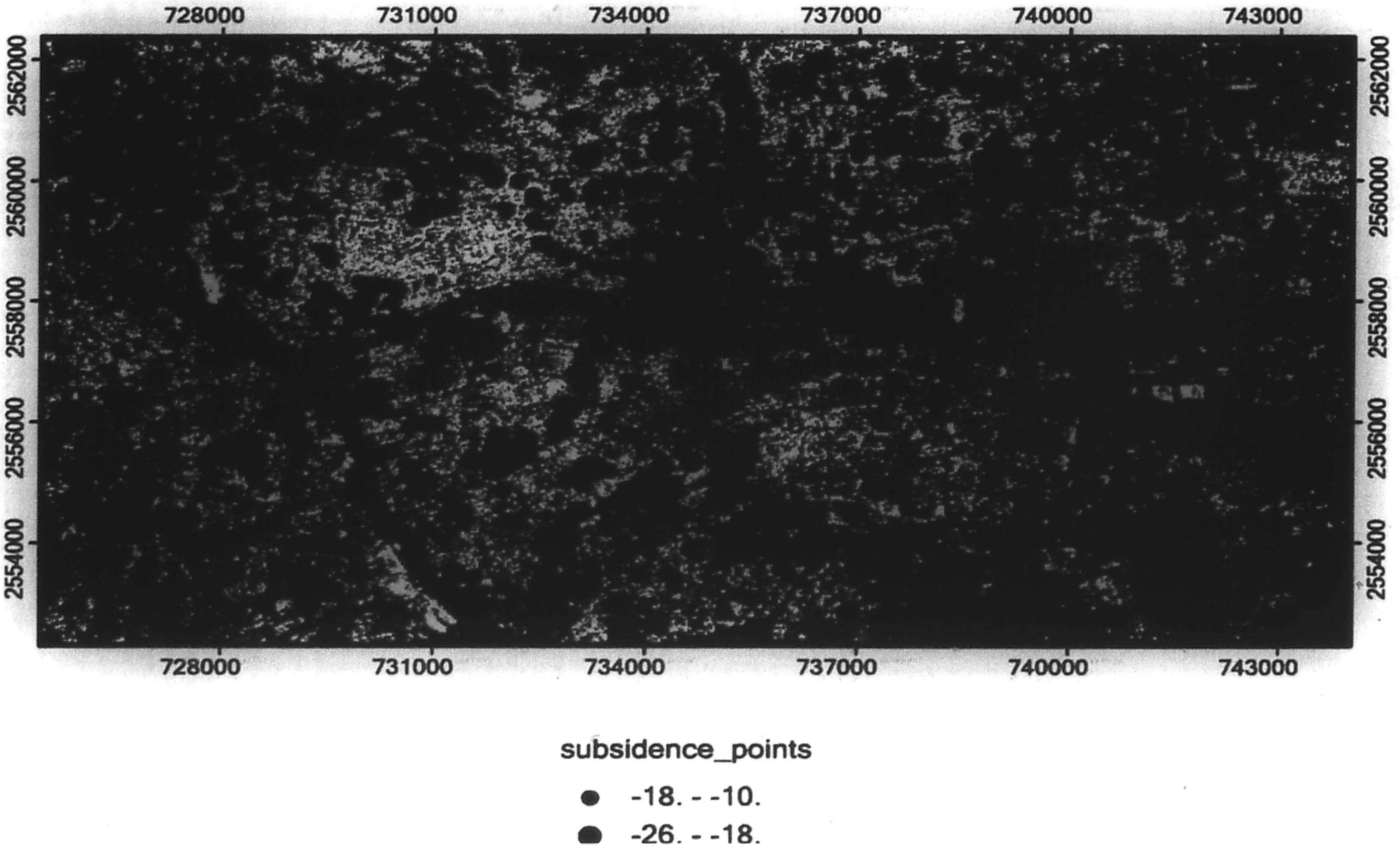

Figure 6.1 A thematic map of active subsidence zones derived from ASAR-PSI point targets in Guangzhou city. The points are classified into 3 classes. The bigger point refers to the greater subsidence value. The background image is an ENVISAT ASAR image.

The northwest and north subsidence sub-zones with the densest distribution of active subsidence points are distributed at the downtown area (Yuexiu District), which is the old business center in Guangzhou city.

6.2 Analysis of mechanisms of the active subsidence zones

As above mentioned, the mechanisms for resulting in the ground subsidence may be quite complicated. In the study area, the geological structure, the characteristics of sediment spatial distribution, over-development, and underground engineering projects are considered as major factors. Thus, this section shows that the relationships between the distribution of active subsidence zones and the four factors.

A. Large scale geological structure

In order to analyze the relationship between the distribution of active subsidence zones and geological structure, a local geological map including geological structure, sediments, and rocks information are collected as shown in Fig. 6.2. It is clear that two obvious active subsidence zones, one is marked as a brown capital C-shape and another as an ellipse, are distributed on the two sides of a geological fault running southwest-northeastward. Along another west-east fault, active subsidence points are also distributed on the two sides of the fault.

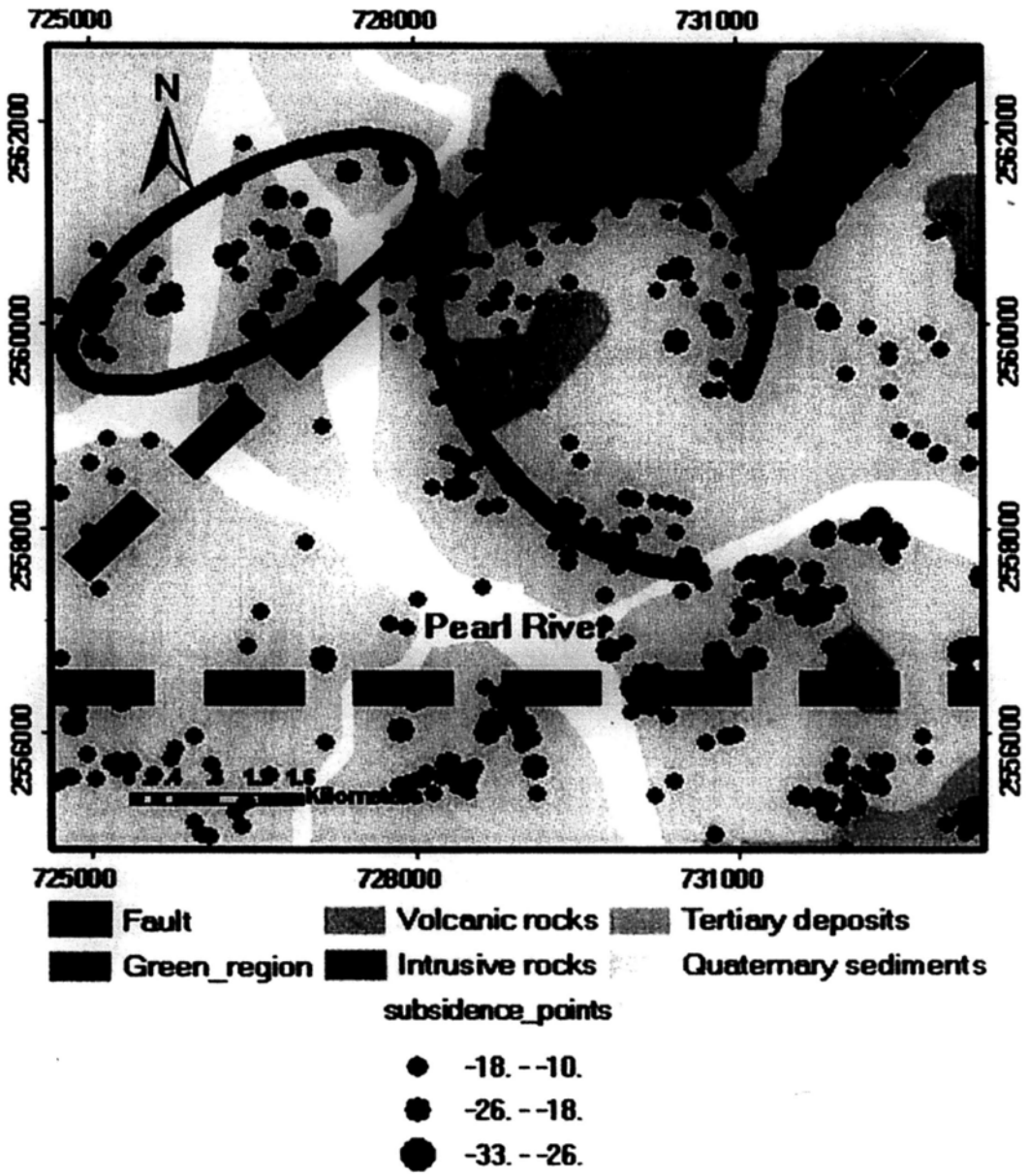

Figure 6.2 Interpretation map of the relationship between active subsidence zones and geological structure.

B. Sedimentation boundaries

As shown in Fig. 4.7, four active subsidence zones, which are distributed on sedimentation boundaries, are found according to the active subsidence zones of

ASAR-PSI detected point targets in Guangzhou city. Three of the active subsidence zones are located on the north side of the Pearl River. The two kinds of sediments are Quaternary sediments (shown with gray color) and Tertiary deposits (light brown). The porosities, water content, void ratio, compressibility, bearing capacity and shear strength of the two kinds of sediments are different *(Zhou, et al., 2006; Zhou, et al., 2009)*. Subsidence zones usually distributes on the boundaries of sedimentations. Our result is consistent with the natural characteristic.

C. Underground engineering projects

The spatial distribution of main ground collapse accidents occurring from 2007 to 2009 is shown in Fig.6.3. These accidents are mainly distributed along the underground metro-lines around Datansha Island. Table 6.1 is the ground collapse accidents (*http://www.gdemo.gov.cn/yjdt/gdyjdt/200811/t20081106_72196.htm;http://gd.nfdaily.cn/content/2009-04/08/content_5046438.htm;http://news.sina.com.cn/c/2009-03-18/012017426289.shtml*).

Datansha Island is located in the center of the Pearl River in the northwest of Guangzhou city, where two under-construction underground metro-lines pass-through and intersect. Our previous work has shown that the ground subsidence is closely associated with underground subway construction (*Zhao, et al., 2009a*).

Among the 9 ground accidents, four were occurred on Datansha Island. The locations of the 4 ground collapse accidents are very close to the two under-construction

metro-lines. This indicates underground engineering projects probably lead to the ground collapse accidents. Furthermore, based on the above analysis, underground engineering projects may not be a single factor. It is also affected by geological structure and rocky conditions. The active subsidence points are dense near most of the ground collapse accidents. It implies that the active subsidence zone has a high relationship with these underground engineering projects.

On the other hand, Fig.6.3 shows that the active subsidence points mainly distribute around the downtown area. The relationship between active subsidence points and downtown area is discussed below.

Table 6.1 Ground collapse accidents in Guangzhou in 2007-2009 coded from 1 to 9 in Fig. 6.4 (partially referred to (*Zhao, et al., 2009a*))

Code	Occurrence time	Location	Scope, x×y×z	DR* mma^{-1}
1	Feb 29, 2008	Huanshixi Road, Liwan	3m x 1.5m x 3m	-15 - -10
2	Jan 31, 2008	Zhongshanba Road	small scope 30cm deep	-15 - -10
3	Oct 06, 2007	Duobao Road	300 m^2, ~ 6m deep	-20 - -15
4	Feb 18, 2008	Juncture of Zhongshanba Rd. Nanan Rd and Huangsha Av, Liwan	100m^2, deepest site: over 40m	-20 - -15
5	Jan 23-24, 2008	Datansha Island	200-300m^2,>3 m deep	-15 - -10
6	Feb 02, 2008	Datansha Island	Observable	-15 - -10
7	Nov 04, 2008	Datansha Island	500 m^2, 100m x 0.2m x 1m	-20 - -15
8	Feb 17, 2009	Juncture of Nanzhou Rd and South Dongxiao Rd, Haizhu	Observable	-15 - -10
9	Mar 04, 2009	Keji Rd, Tianhe	Observable	-15 - -10

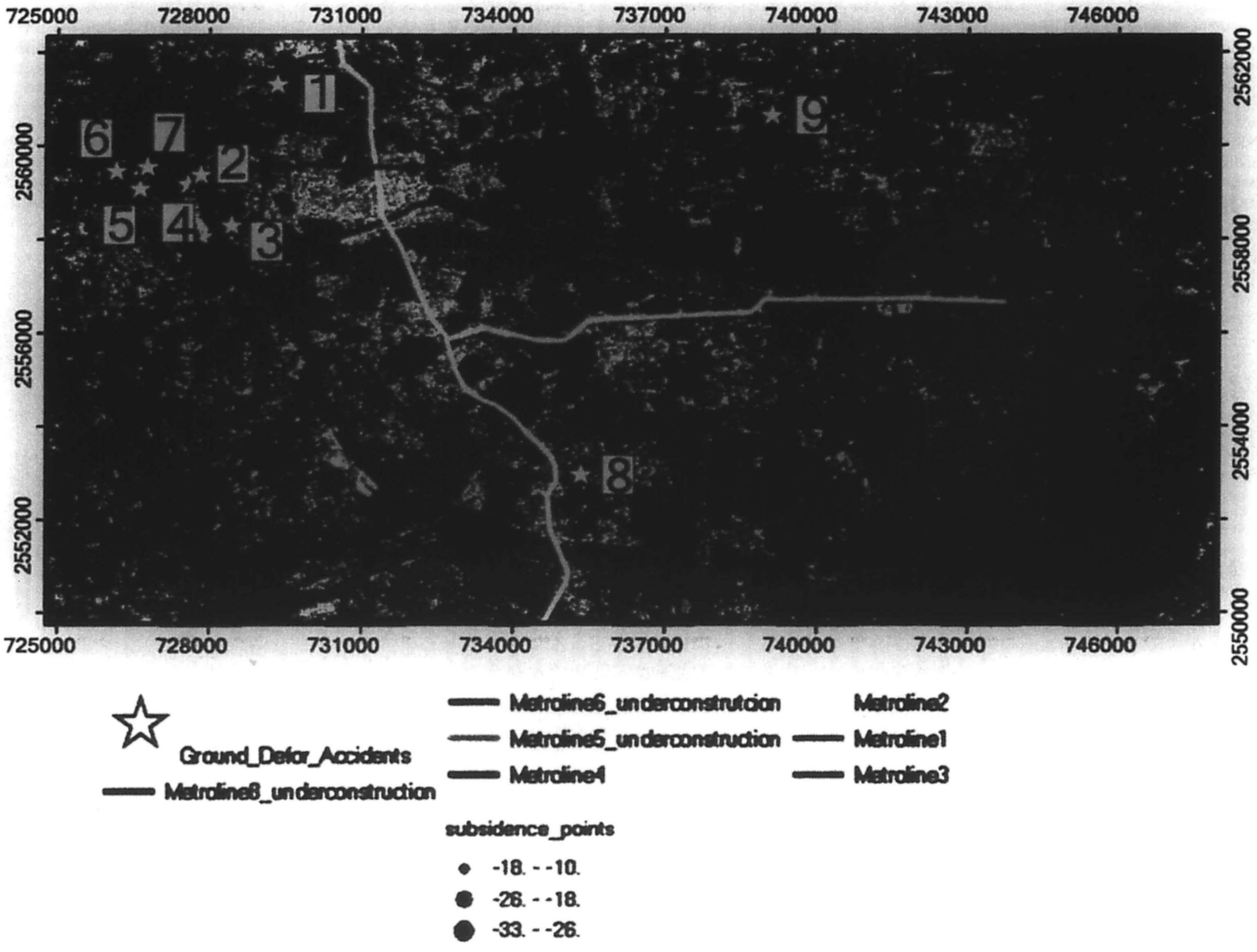

Figure 6.3 Interpretation map of the relationship between active subsidence zones and underground engineering projects

D. Subsidence in the old downtown

From Fig. 6.4, it is also noted that the active subsidence points are mainly distributed in the old downtown area. Fig. 6.4 shows that the downtown of Guangzhou city with the largest spatial scale and the densest distribution of active subsidence points in the study. This implies that the old downtown area is over-development, which may be an important reason to cause the ground subsidence. Yuexiu district shown in Fig. 6.4 is the oldest urban area in Guangzhou city. The average population density is, 35,000 persons dwell in each square kilometer of Yuexiu district, where the urban blocks often have an oppressive building density of more than 70%. On the other hand, as discussed earlier, this active subsidence zone is also located in the sedimentation boundaries. Thus, over-development and sedimentation boundaries are probably the major factors, leading to these dense active subsidence points.

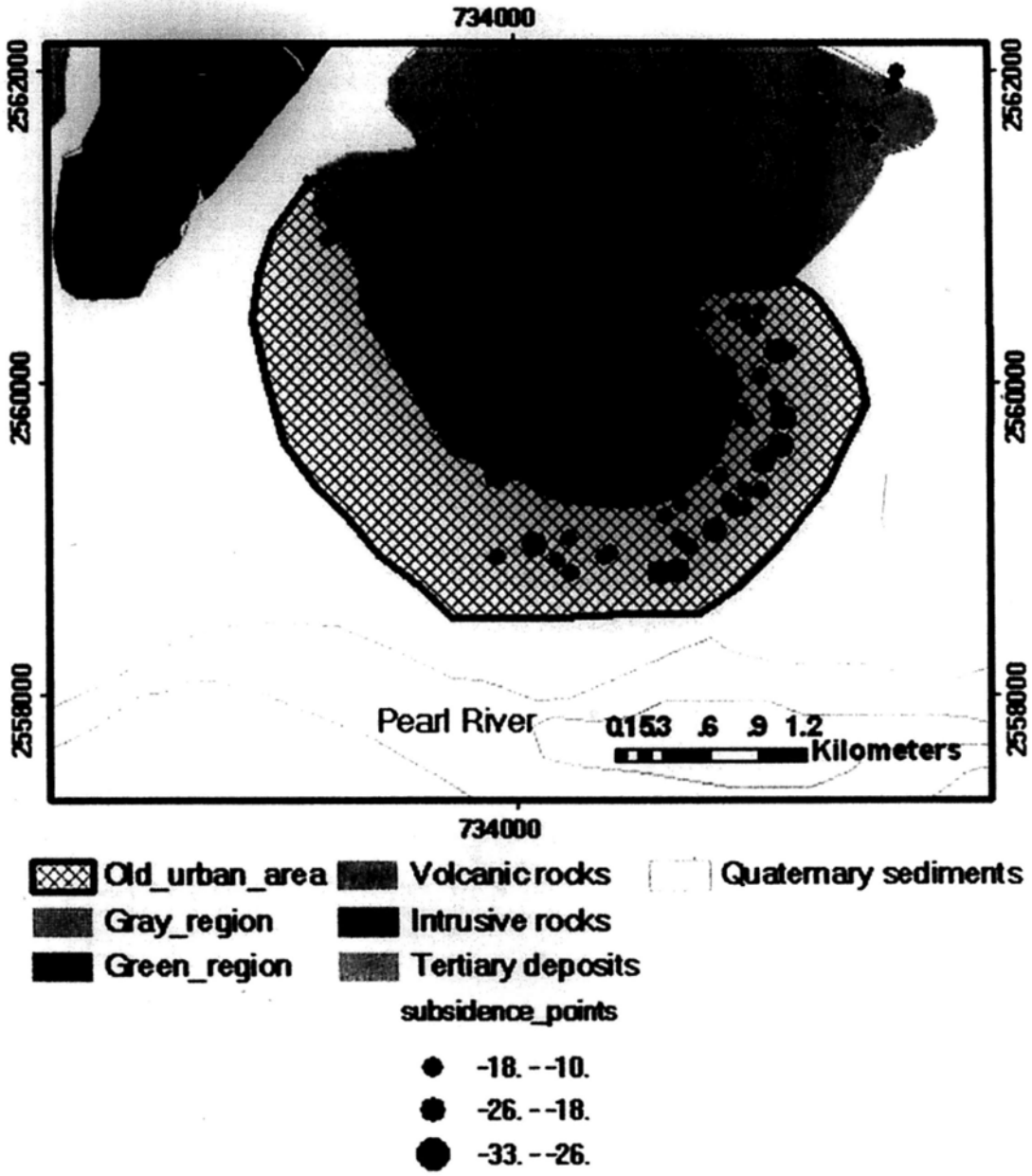

Figure 6.4 Interpretation map of the relationship between active subsidence zones and downtown area

6.3 Summary

In this section, the ASAR-PSI technology is used to detect the ground deformation in the urban area of Guangzhou, China. An area with a ground deformation rate,

subsidence or rise, greater than 10 mma^{-1} is defined as an active ground deformation zone. Based on the ground deformation rate maps, thematic maps of active subsidence zones are generated and further analyzed.

The geological structure, the characteristics of sediment spatial distribution characteristics, over-development, and underground engineering projects are considered as four major mechanisms for inducing the active subsidence zones. The analysis of relationships between the distribution of active subsidence zones and the four factors indicates that. The results are summarized as follows.

The spatial distribution characteristic of active subsidence zones has a close relationship with the geological fault. Two obvious active subsidence zones are distributed on the two sides of a geological fault running southwest-northeastward.

Four active subsidence zones, which are distributed on sedimentation boundaries, are found. This implies that the sedimentation boundaries are an important factor, which affects the distribution of active subsidence zones.

The major subsidence sub-zones with the densest distribution of active subsidence points are mainly distributed in the old downtown area at Yuexiu District, which is the oldest business center in Guangzhou city. Over-development and sedimentation boundaries are probably the major factors for resulting in the ground subsidence.

For the case of Datansha Island, our previous work has shown that the ground

subsidence is closely associated with underground subway construction. As shown in thematic maps of active subsidence zones, the geological structure and underground engineering projects mainly cause the area to be an active subsidence zone. The further study still needs to be investigated.

In summary, combined ASAR-PSI detected ground deformation data with geomorphologic data, the relationships between active subsidence zone and local geological structures, sediment distribution characteristics, density of buildings, and underground engineering projects are analyzed and interpreted in the study. The results can serve as useful information for local development planning and decision making.

Chapter 7. Detection of Residual Settlement at Hong Kong International Airport

7.1 Introduction

Previous investigations have indicated that the major natural forces causing ground deformation include large-scale plate tectonic motion, volcanic activity, local geological processes, effects of ocean tides, and hydrological loading (*Jónsson, 2002; Stephen, et al., 2001; Khan and Scherneck, 2003; Mangiarotti, et al., 2001; Zerbini, et al., 2002*). Human activities are also considered as a contributory factor for ground deformation (*Ding, et al., 2004; Liu, et al., 2001; Holzer and Johnson, 1985; Fielding, et al., 1998*). Even a very small ground deformation may seriously impact people's living conditions. A ground subsidence of a rate of 1 cma^{-1} may cause serious damages to the buildings, highways, airport runway, harbors, and underground facilities (*Zhi, et al., 2001; McFadden and Siebe, 1986; Teatini, et al., 2005; Lee, et al., 2006*).

HKIA, the study area, is an important international airport in Asia. The airport was built on an area of 12.5 km^2, of which three quarters were reclaimed from the sea. Another quarter was made of the former Chek Lap Kok Island and Lam Chau Island (*Plant and Oakervee, 1998b*). The majority of buildings and facilities of HKIA are built on the reclaimed foundation. Therefore, the ground stability of the HKIA platform is a matter of public concern.

Ground settlement of the reclaimed foundation has occurred during construction of the airport and will continue at a reducing rate after the completion of the filling project (*Plant et al., 1998a*). The early prediction of residual settlement from 1997 to 2040 based on field measurements and laboratory tests is in the range of 200 to 500 mm. Ten years have passed since the opening of the airport for commercial operations in 1998. What is the current status of ground settlement at HKIA? Is it within a reasonable range? These questions should be both asked and answered. Thus, detecting the ground deformation and clarifying its fundamental laws are significant research topics for HKIA.

Ground-based monitoring methods, such as spirit leveling and borehole extensometer have been used to detect ground deformation at HKIA. These methods are able to offer high measurement accuracy, but are manpower intensive, time consuming, costly, and point-wised. Thus, the previous investigators have tried to use satellite InSAR to detect ground deformation at the airport. Their results indicated that detected ground deformation agrees with the leveling measurements at some benchmarks to root mean square (RMS) error of 1cm, and an overall correlation coefficient of 0.89 (*Ding, et al.,*

2004; Liu, et al., 2001). They not only confirmed the residual settlement occurrence of the reclaimed foundation, but also pointed out the accuracy of InSAR results hampered by temporal and geometrical decorrelation and atmospheric phase screen.

The main goal of this study is to investigate the residual settlement of reclaimed foundation at HKIA. The ENVISAT ASAR images taken from 19 April 2006 to 9 January 2008 are used to generate a time series of ground deformation at four reference points and ground deformation rate fields over HKIA. The ASAR PSI-detected ground settlement rates are then validated with the ground truth data. In order to correct systematic bias existing in the ASAR PSI results, empirical correction models are developed. The corrected ASAR PSI-detected annual ground settlement rate data are further analyzed. The generated distribution map of the ASAR PSI-detected residual settlement rate over HKIA reclaimed foundation is compared with model-predicted ground settlement map.

7.2 Study area

Hong Kong is a major air transportation center in Asia. The Hong Kong International Airport, the study area as shown in Fig. 7.1, has been one of the largest airports in East Asia since launched in 1998. More than 47.8 million passengers travelled through HKIA in 2007, and the volume of cargo was over 3.74 million tones. The airport was built on an area of 12.5 km^2 located in the Pearl River Estuary, 6 km long and 3.5 km wide. The runways, up to 3800 m in length, are designed to accommodate all types and

sizes of passenger and cargo airplanes. HKIA has a design capacity of 87 million passengers and 9 million tones of air cargo per year (*Shu, 1998*).

The reclaimed ground of the airport was built using 197 million m^3 of reclaimed materials, similar to modern loose sediment. The airport is located in the East Asia sub-tropical monsoon weather region, which is characterized by high annual mean temperature (23.5℃) and high annual mean precipitation (2,214.3 mma^{-1}). This means that geological and meteorological conditions of HKIA are unfavorable for airport ground stability. Fig. 7.1 shows a TerraSAR-X (German radar satellite launched in 2007) image of HKIA, displaying a top view imagery map of HKIA. The dark imagery surrounding the airport is the water area of the Pearl River Estuary. The bright imagery on the lower side is Lantau Island of Hong Kong.

Monitoring potential ground deformation is a vital task for maintaining safe conditions for taking off and landing of aircraft, airport maintenance and management. This study aims to develop applications of interferometric synthetic aperture radar for high accuracy measurement of the airport ground deformation. One of advantages of this study is that the ASAR data are locally acquired and processed at the Hong Kong Satellite Remote Sensing Ground Receiving Station, which was established at the Chinese University of Hong Kong in 2006. Meanwhile, high accuracy ground truth data are available for validation of ASAR PSI-detected ground deformation results.

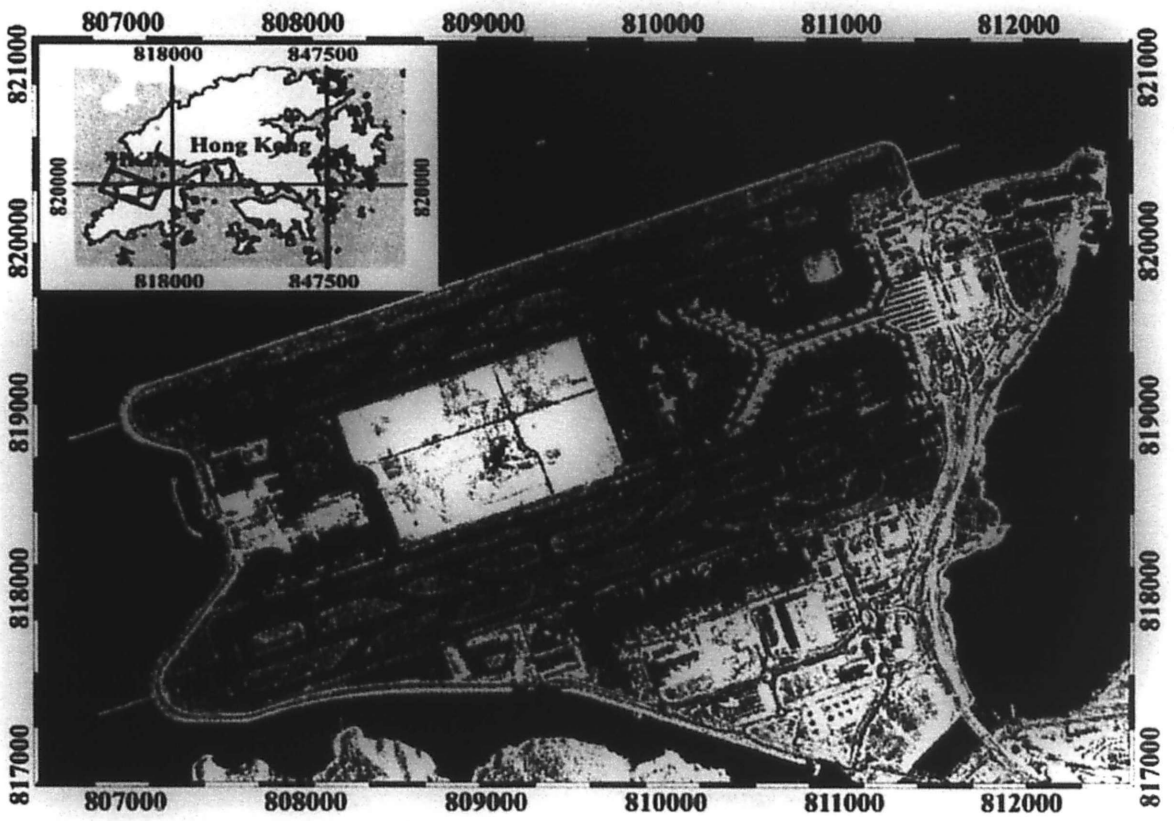

Figure 7.1 A TerraSAR-X single-look complex image product of HKIA in slant range projection and its location in Hong Kong (red box in inset). The spatial resolution is 1 m. The light dark net-like patterns are imagery of the southern and northern runways, respectively. The Projected Coordinate System is WGS 1984 UTM 49N.

7.3 ASAR data and data pre-processing

Table 7.1 lists 15 ASAR images used in this work. ENVISAT offers a 35-day repeat cycle, so that the data schedules generally run at a 35-day time interval. The plot of perpendicular baseline versus temporal baseline is shown in Fig. 7.2.

Table 7.1 Image mode ASAR data used in this study.

No.	Received Date	Orbit Number	Perpendicular Baseline (m)	Temporal Baseline (day)	Doppler Baseline (Hz)
1	04-19-2006	21622	-383	-175	-0.8
2	05-24-2006	22123	347	-140	0.2
3	06-28-2006	22624	-727	-105	21
4	08-02-2006	23125	-866	-70	31.7
5	09-06-2006	23626	220	-35	-36.6
6	10-11-2006	24127	0	0	0
7	02-28-2007	26131	-4	140	8.3
8	04-04-2007	26632	-47	175	-99.4
9	05-09-2007	27133	51	210	20.2
10	06-13-2007	27634	71	245	-49.3
11	07-18-2007	28135	239	280	-22.8
12	08-22-2007	28636	324	315	-41.2
13	10-31-2007	29638	165	385	0.6
14	12-05-2007	30139	-203	420	-25.1
15	01-09-2008	30640	239	455	-1.6

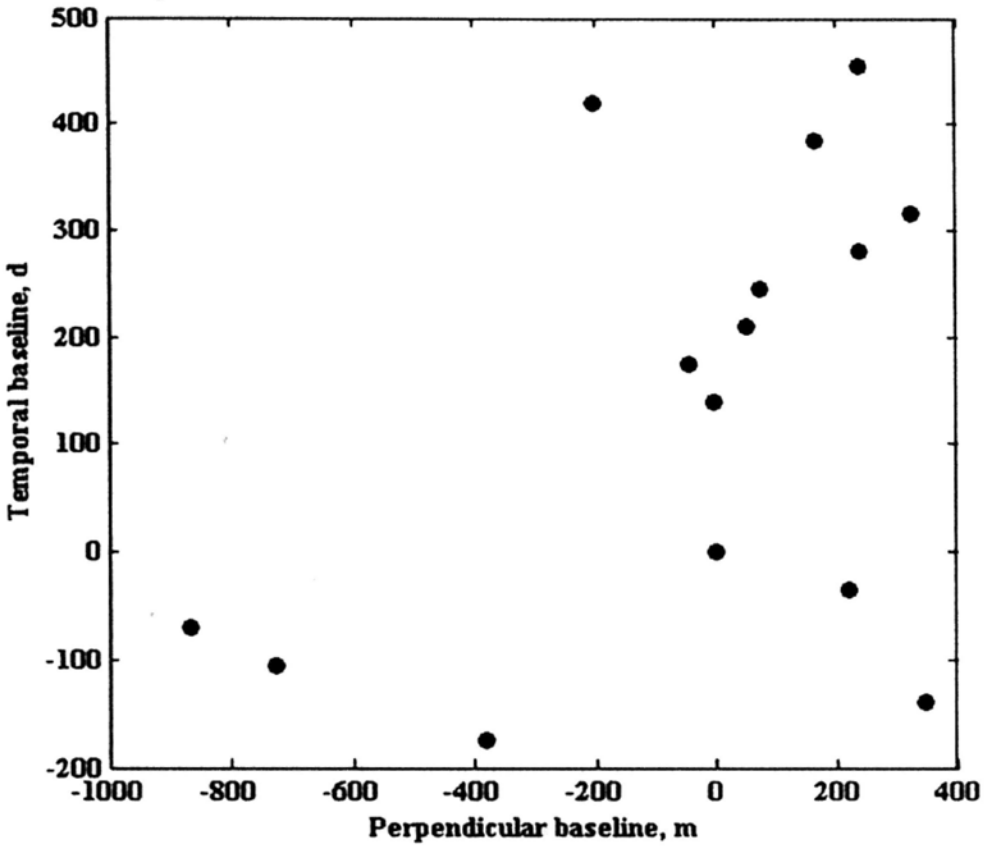

Figure 7.2 A plot of baseline configuration. The temporal baseline is given on the vertical axis, and the horizontal axis represents the perpendicular baselines, relative to the master acquisition at (0, 0). The 15 acquisition times and perpendicular baselines correspond to actual acquired images for ASAR frame 441, track 25.

7.4 Ground truth data

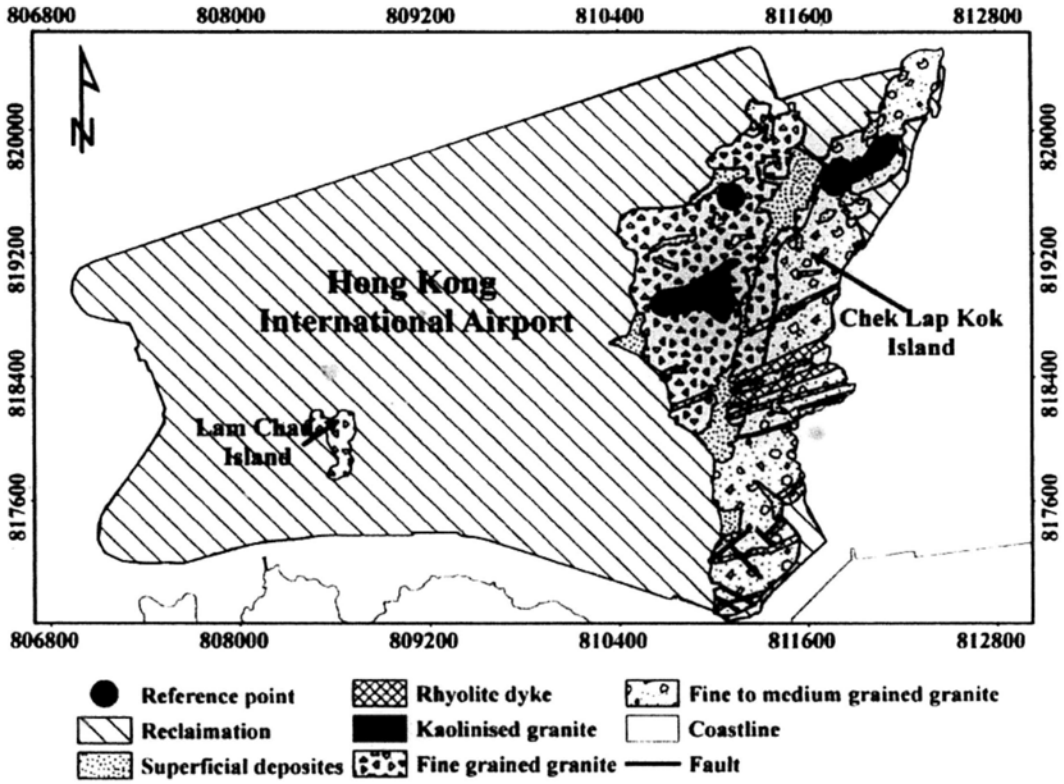

Figure 7.3 A Geological map of Hong Kong International Airport. The black double circled point marked on Chek Lap Kok Island is the reference point. (partially referred to (*Plant et al., 1998a*))

The Airport Authority Hong Kong provided the ground truth data of ground settlement used for this study. There are 36 ground control points surveyed by traditional leveling methods from March 2006 to April 2007. These ground control points are mainly distributed along the center-line of the Southern Runway and around the Passenger Terminal Building. The reference point for ground deformation and unwrapping is

located at the northeast of HKIA, where the geological condition is granite, as marked in Fig. 7.3. The ground truth data accuracy is better than 0.1 mm. I calculate the annual ground settlement rate of each ground control point, and use these results to validate ASAR PSI-detected annual ground settlement rate.

7.5 Validation of ASAR PSI-detected ground settlement data

7.5.1Time series analysis

As mentioned in Section 4.1, the PSI technology has an important capacity of generating a time series of ground deformation data. One of the validation methods for PSI-detected ground settlement data is comparing them with simultaneously measured ground truth data. In this study, four point targets coded 32524, 32816, 32672, and 33055 as marked in Fig. 7.13 are chosen for the validation. The results are shown in Fig. 7.4. From the curves shown in the Figures 7.4 a-d, one can see two major features. 1) The two data sets show the same trends. Figures 7.4a and 7.4b show that the ground subsided quite quickly from March 2006 to March 2007 at an annual rate of 4.5 mma^{-1} and 12.5 mma^{-1} at point targets 32524 and 32816, respectively. After that, the data sets show that the ground was basically in a stable status. Unlike point targets 32524 and 32816, the two data sets measured at point targets 32672 and 33055 show a continuous subsidence trend. 2) The curves of all four point targets show that the magnitudes of PSI-detected ground subsidence and the slopes of the curves are smaller than the ground truth data. This

implies that there are systematic biases between the two data sets, which should be corrected, when the PSI-detected ground subsidence data are used for operational or research purposes.

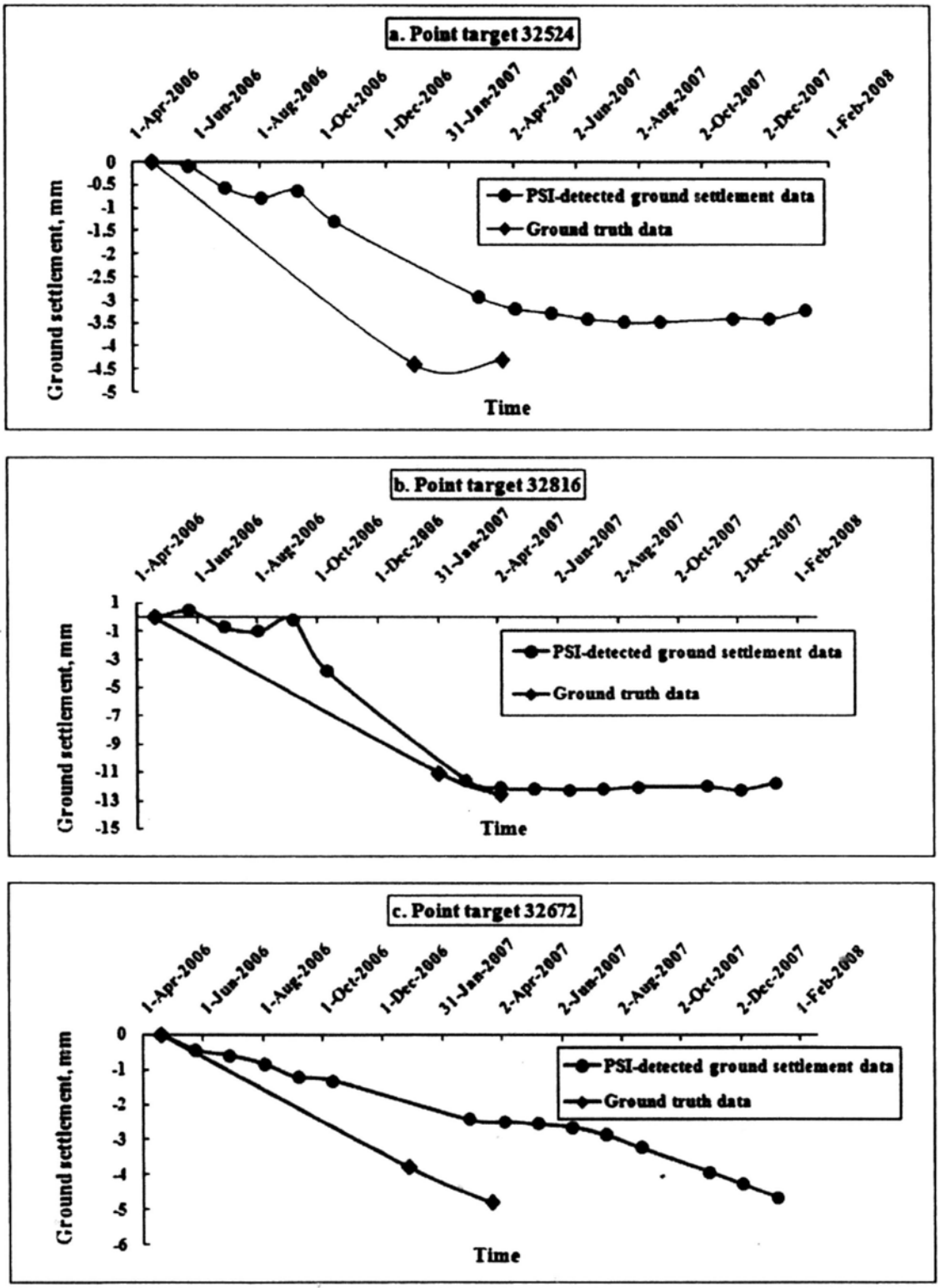

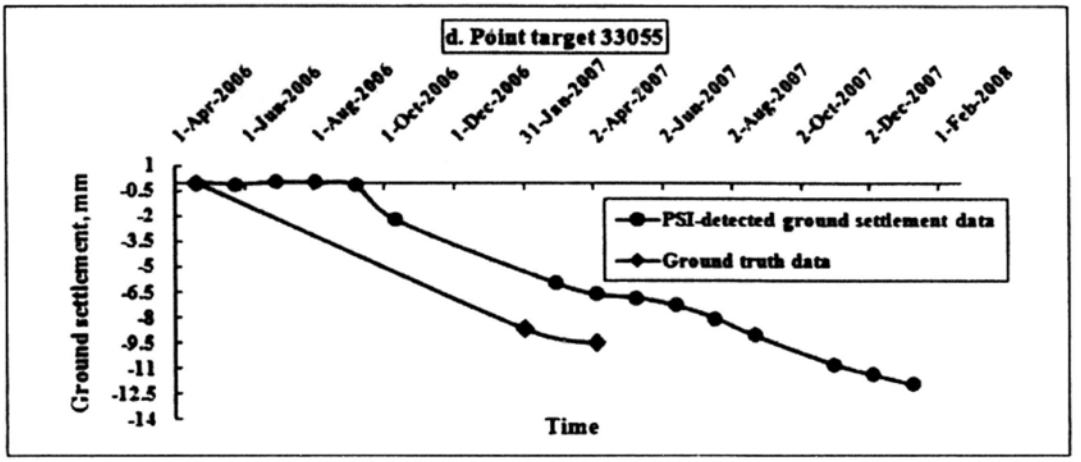

Figure 7.4 Time series of ground settlement process at four point targets of HKIA. Dots represent the ASAR-PSI detected ground settlement data, and diamonds represent the simultaneously measured ground truth data.

7.5.2 Derivation of new empirical correction models

Using the methods mentioned in Chapter 4, I obtain an ASAR PSI-detected ground settlement rate data set of the reclaimed foundation area of HKIA platform from 2006 to 2008. Before further analysis can be carried out, this data set should be validated against simultaneously or near-simultaneously field-measured ground settlement rate data. In fact, the time series analysis in the above section has indicated that there are systematic biases between the two data sets. Therefore, it is necessary to derive empirical models from the available data for removing the biases from ASAR PSI-detected ground deformation data. Fig. 7.5 shows a comparison of the two data sets. One can see that for the small magnitudes of ground deformation (< 4 mma^{-1}), the ASAR PSI-detected values overestimate the ground deformation, but for the large magnitudes of ground deformation (> 4 mma^{-1}), the ASAR PSI-detected ground deformation values underestimate the

ground deformation.

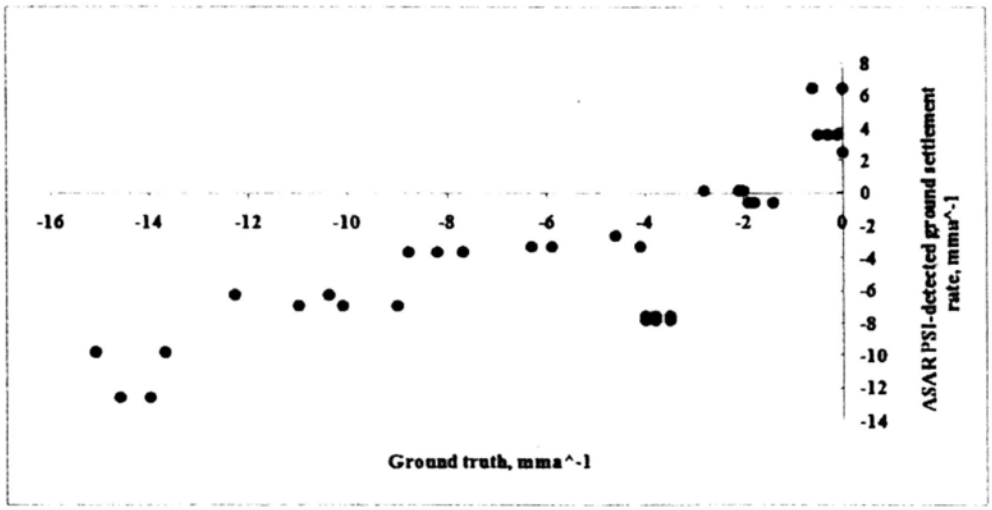

Figure 7.5 Comparison of ASAR PSI-detected ground settlement rate data of the reclaimed foundation area of HKIA platform from 2006 to 2008 with simultaneous or near-simultaneous ground truth data.

In order to derive empirical models from the data shown in Fig. 7.5 to correct ASAR PSI-detected ground settlement rate data, two linear functions are used to fit the data in the form of

$$H_a = \begin{cases} 3.262H + 5.374, & -4 < H < 0, \\ 0.832H + 1.818, & H < -4, \end{cases} \tag{7.1}$$

where H_a is the ASAR PSI-detected ground settlement rate, H is the ground truth, and both of them are in mma^{-1}. Comparison of the empirical functions with the data is shown in Figures 7.6a and 7.6b. The empirical functions fit the data points quite well, with correlation coefficients of 0.891 and 0.834, respectively.

From (7.1), empirical correction models for the ASAR PSI-detected ground settlement rate are derived in the form of

$$H = \begin{cases} 0.307H_a - 1.65, & -4 < H < 0, \\ 1.20H_a - 2.19, & H < -4, \end{cases} \tag{7.2}$$

where H is the real ground settlement rate in mma^{-1}. Fig. 7.7 shows a comparison of the ASAR PSI-detected ground settlement rate corrected with the empirical functions (7.2) to the ground truth data. The slope of the linear regression line of the data points is near 1 and an intercept is near 0. The correlation coefficient is as high as 0.95. This implies that the empirical correction models (7.2) work almost perfectly. Thus, these models are used to correct the ASAR PSI-detected ground settlement rate data set for further analysis.

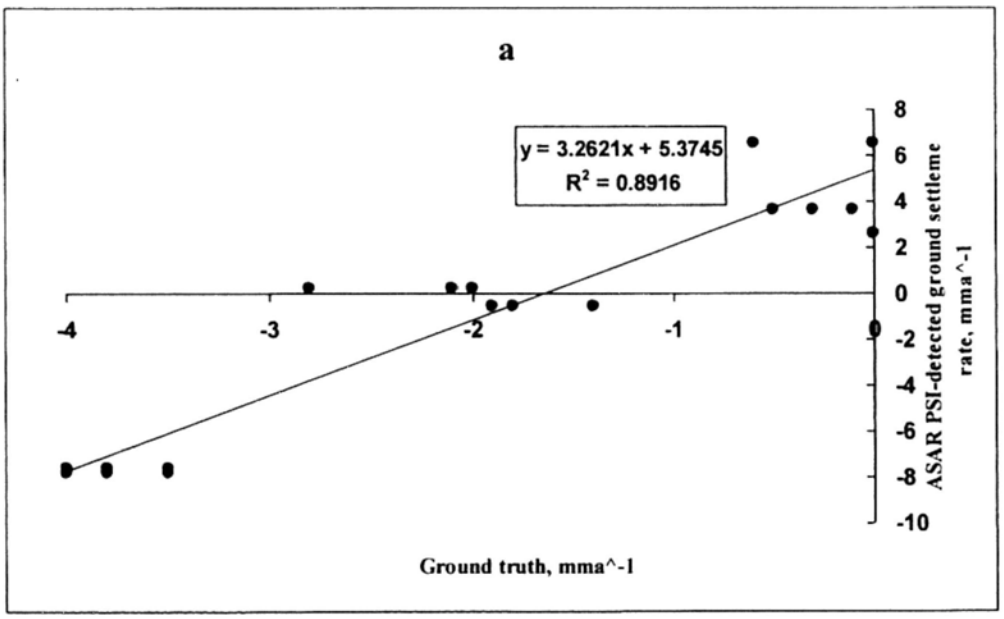

Figure 7.6(a) Comparison of the empirical functions with the ground settlement rate data for -4 < H < 0

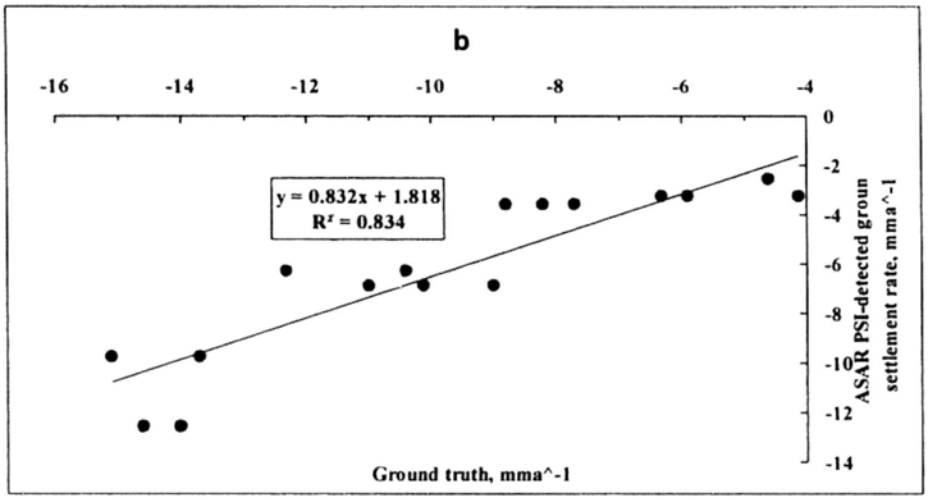

Figure 7.6(b) Comparison of the empirical functions with the ground settlement rate data for H < -4

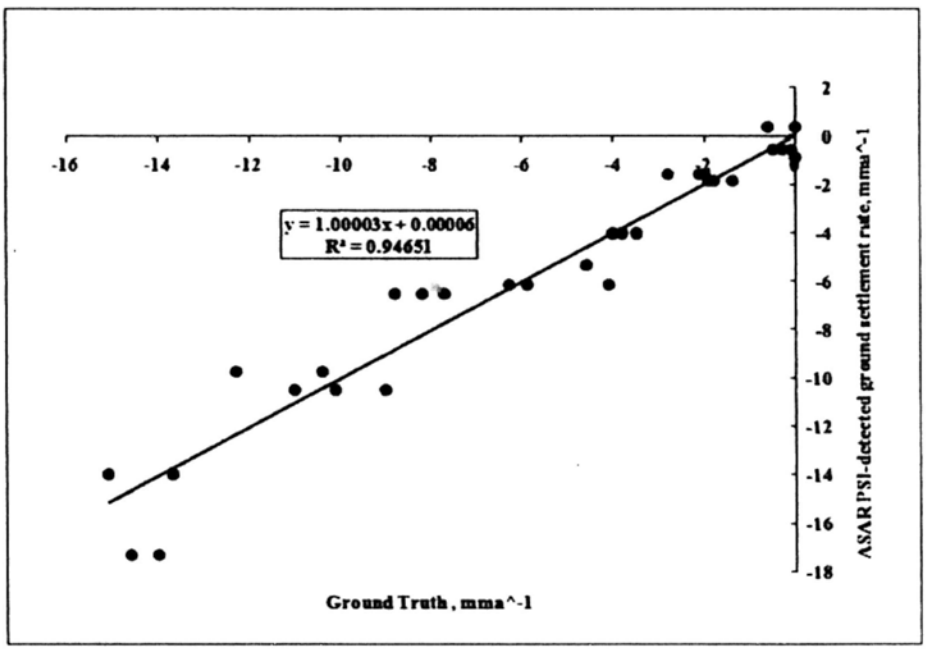

Figure 7.7 Comparison of the ASAR PSI-detected ground settlement rate of HKIA reclaimed foundation from 2006 to 2008 corrected with empirical models (7.2) to simultaneous or near-simultaneous ground truth data.

7.6 Statistical features of ground settlement in HKIA reclaimed foundation

After correction by empirical models, statistical distribution of residual settlement rate of corrected data set is shown in Fig. 7.8. This plot does not correspond to the one represented in Chapter 4 where the settlement rate of all point targets are shown.

One can see that the Lorentz distribution function in the form of

$$f(x) = a_1 e^{-\left[x-b_1/\sqrt{2}\sigma_1\right]^2} + a_2 e^{-\left[x-b_2/\sqrt{2}\sigma_2\right]^2} \tag{7.4}$$

fits the ASAR PSI-detected ground residual settlement rate distribution very well. Here a_1 and a_2 are coefficients, respectively. Goodness of fit, R-square, is 0.98. Two peaks are located at -2.7 mma^{-1} (b_1) and -10 mma^{-1} (b_2), respectively. This double-peaked distribution indicates that the residual settlement process is dominated by two modes or categories of settlement rates. The first mode or category, covered by the first normal distribution, contains 42% of the total, representing a relatively stable state with a maximum annual settlement rate smaller than -4 mma^{-1}, which is smaller than an estimated average deformation rate for the crust of 5 mma^{-1} (*Zhao, et al., 2009a*). The second mode or category, covered by the second normal distribution, which has a peak at -10 mma^{-1}, 58% of the total, representing a continuous settlement state. The spatial distribution of these two mode points will be mapped and further analyzed in the next section.

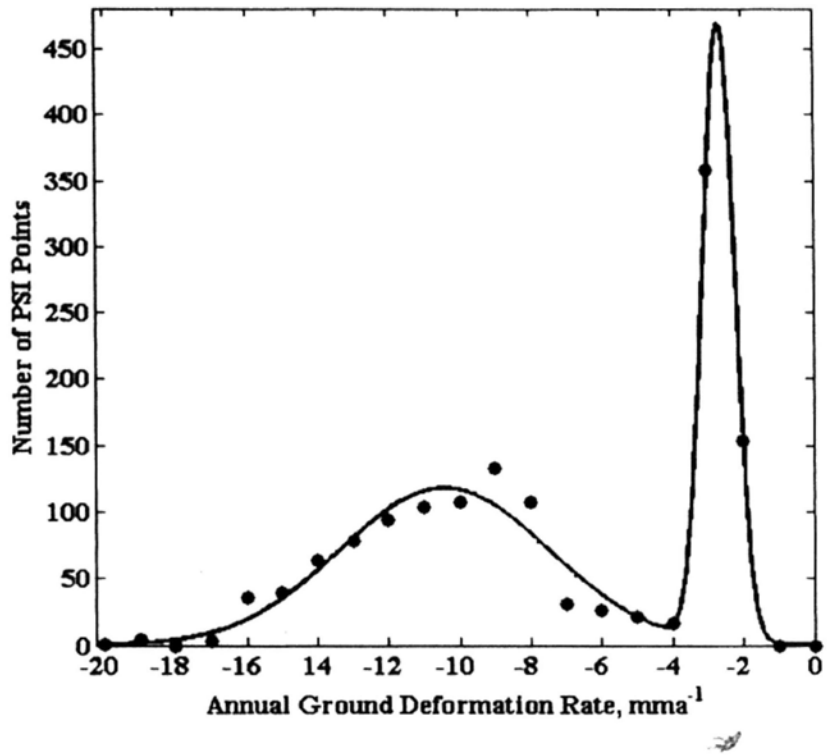

Figure 7.8 Statistical features of ground settlement in HKIA reclaimed foundation. The vertical axis represents the numbers of data points, and the horizontal axis represents the annual ground settlement rates in mma^{-1}. The curve represents a Lorentz distribution function.

As mentioned above, in this study, the ASAR PSI technology is only applied to detect the ground settlement of the reclaimed foundation area of HKIA platform. The foundation is still in residual settlement (*Plant and Oakervee, 1998*). Thus, any positive ground deformation values (ground rising) are physically unreasonable. The simultaneous ground truth data also do not contain any positive values. In the ASAR PSI-detected ground deformation data set, however, there are indeed positive data. The statistical distribution of these positive values is shown in Fig. 7.9. One can see that the data points

follow a Lorentz distribution (7.4) consisting of two normal (Gaussian) distributions. The peak of the first normal distribution is located at 2 mma^{-1}, and that of the second is located at 8 mma^{-1}.

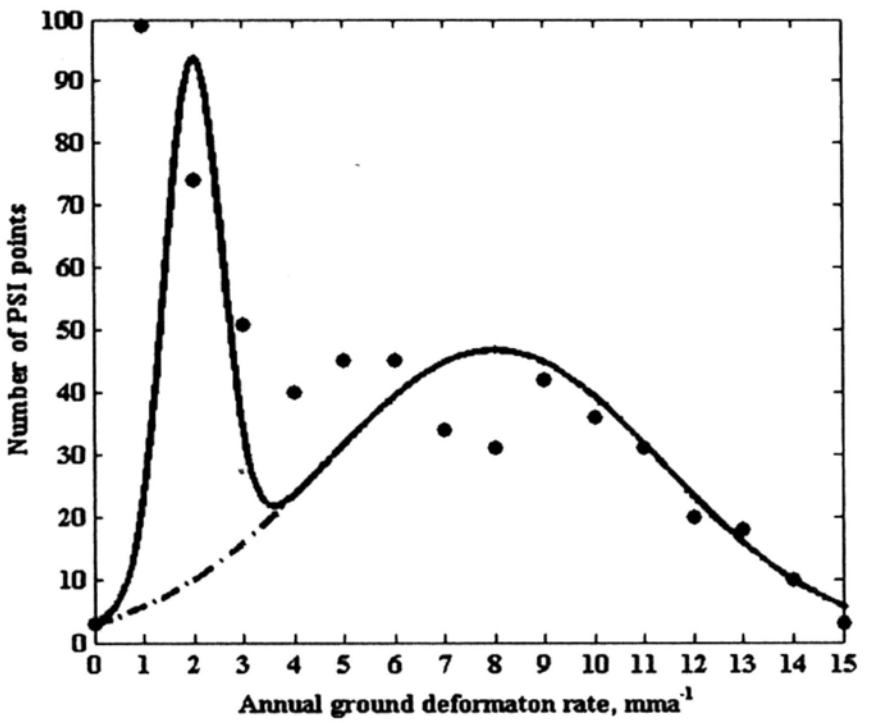

Figure 7.9 Statistical distribution of positive ground deformation values in the ASAR PSI-detected ground deformation data set. The curve represents a Lorentz distribution function. The dashed line represents a normal distribution.

In order to analyze these unreasonable data points, I draw a scatter plot of ground deformation rate value and coherence value. The scatter plot is shown below.

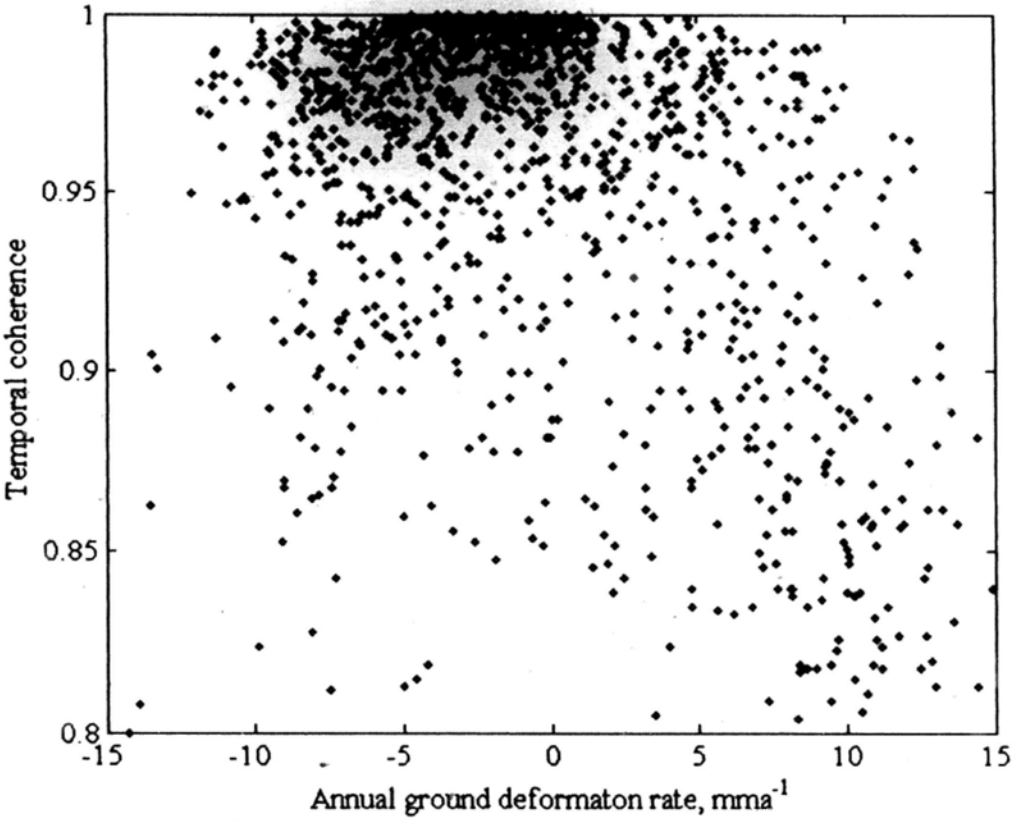

Figure 7.10 A scatter plot of ground deformation rate value and coherence value.

The data points, with which temporal coherence values are lower than 0.95, and annual ground deformation rate value are greater than 8 mma^{-1}, are selected. These points are drawn on a geographical map. I find that the most points are distributed at the airport Midfield, which is under construction. Thus, I believe that these unreasonable positive values may be caused by some unknown or uncertain processes. Therefore, I discard them for further analysis.

Figure 7.11 Locations of data points with lower temporal coherence and greater annual ground deformation rate value.

7.7 Mapping and spatial distribution feature analysis

Fig. 7.12 shows a distribution map of the ASAR PSI-detected residual settlement rate over HKIA reclaimed foundation. I have corrected the data using the empirical correction models. According to the PSI point density of different settlement categories, the HKIA reclaimed foundation can generally be divided into sub-areas as shown in Fig. 7.13. There are three relatively stable sub-areas marked by G1, G2, and G3, respectively. G1 contains the Passenger Terminal Building area. G2 contains a major part of the Southern Runway area. There are four continuous settlement sub-areas marked by R1, R2,

R3, and R4, respectively. The largest one, R1, is located at the Midfield of the airport. Other three sub-areas are distributed at the western and southern boundaries.

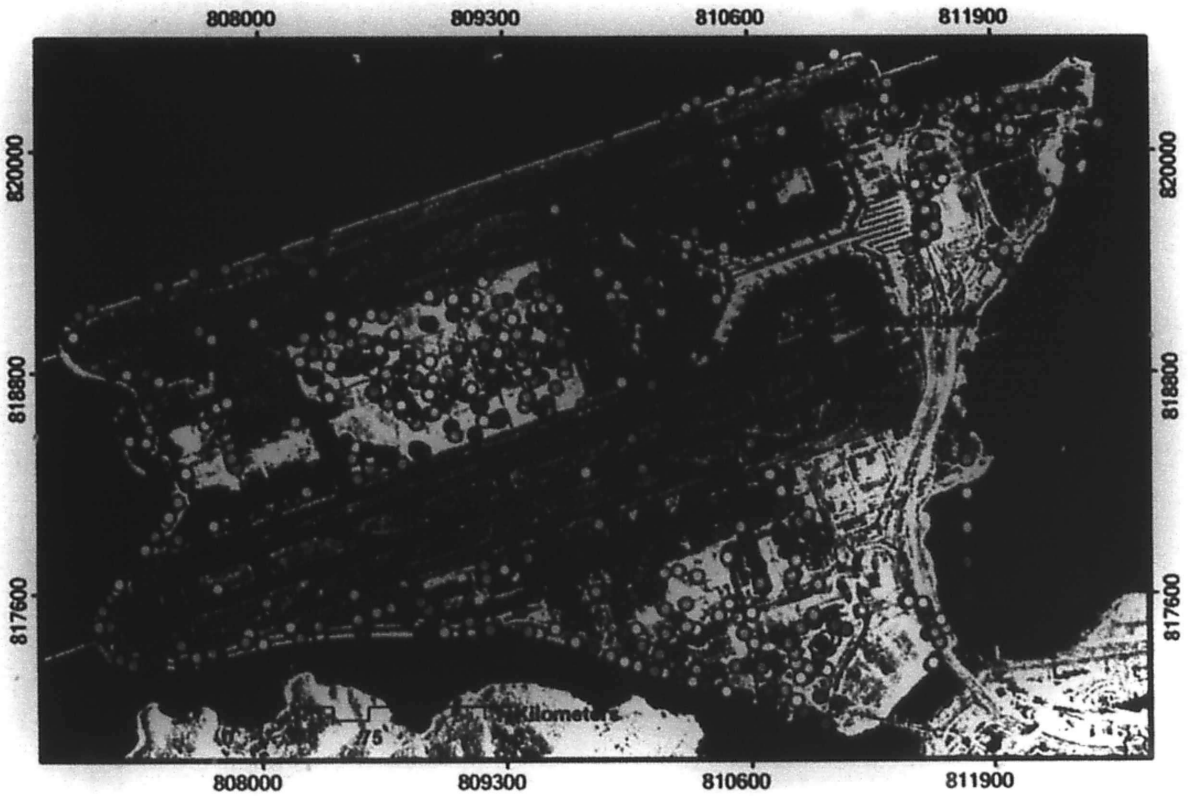

Figure 7.12 A spatial distribution map of ASAR PSI points. Color codes represent the settlement rates.

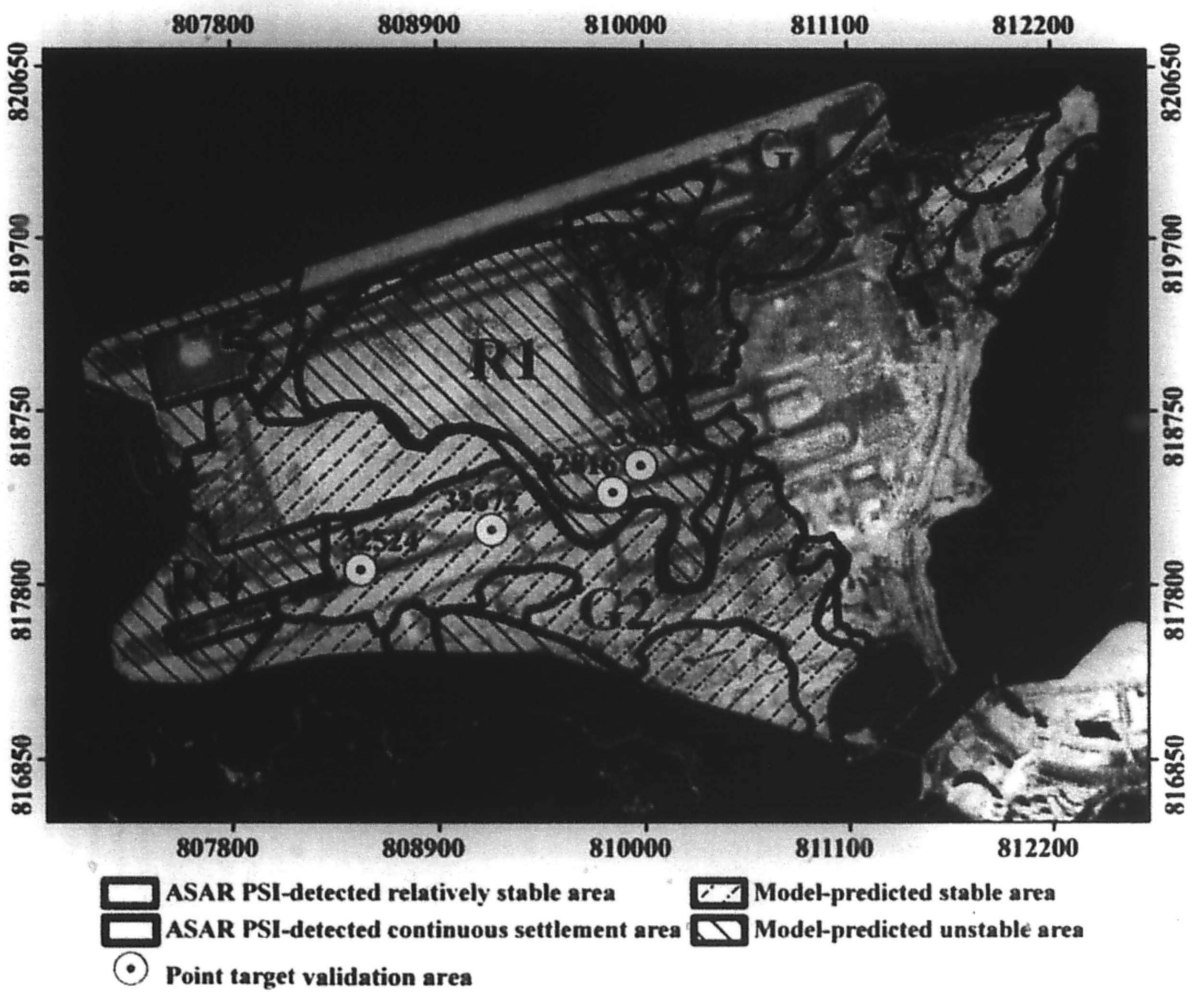

Figure 7.13 General patterns of ASAR PSI-detected ground residual settlement states (enclosed by bold lines) and model-predicted ground settlement states (shadowed areas with boundaries in black). Yellow points show four point targets for the time series analysis.

7.8 Discussion

Like all other measurement technologies, PSI methods also generate errors in their results. It is believed that the reasons or mechanisms to cause the errors are quite complicated, so that I could not find any previous publication, which gave a complete analysis or explanation for the reasons. For my dissertation research, the time series data shown in Fig. 7.4 reveal that the ASAR PSI-detected ground deformation values

systematically underestimate the real ground deformation represented by the ground truth data. Assuming that the atmospheric effects have been corrected by the PSI algorithms I used, there are several potential reasons to cause this systematic bias as analyzed as follows.

1) Un-matched measurement positions. Basically, the ASAR PSI-detected ground deformation values and the ground truth data measured by traditional technologies are completely different data sets. It is reasonable for that there are errors or biases between the two. Un-matched measured positions of the two technologies used to derive the ground deformation rate are one of the reasons to cause the errors. In this study, I measured that the distances between the nearest centers of ASAR image pixels and the ground truth measurement points range from 20 m to 100 m. In other words, the two are not exactly matched each other. Therefore, it is expectable that the ground deformation values derived from the two methods would not be always the same.

2) Different spatial resolution. The two technologies have different ground resolution cell sizes. The size of the ASAR resolution cell is about 80 m^2 (12.5 m by 7.8 m), and the resolution of field measurements is a point. Thus, the ASAR-PSI detected ground deformation rate values are the spatially averaged results, which may polish out the contributions of extreme values. As a result, the ASAR-PSI detected ground deformation rate values may overestimate the small deformation and underestimate the large deformation. This may explain the reasons for systematic bases as shown in Figures 7.6a, 7.6b, and 7.7. The biases are related with different properties of the two groups: one

group has the settlement rate amplitude between 0 mma^{-1} and 4 mma^{-1}, which is overestimated; the other group has the settlement rate amplitude > 4 mma^{-1}, which is underestimated.

3) Limited length of time series data. My experiment used 15 images from April 2006 to January 2008. The errors could be deduced with more images.

4) Cycle skip. In radar pulse phase delay calculation, there is an uncertainty of $2k\pi$ (k=1, 2, 3,...). Sometimes this can lead to an aliasing of the results. Topographic error, distribution of temporal and normal baselines, and unknown processing errors are other potential sources which may induce systematic biases.

During the site preparation period of HKIA, residual settlement of reclaimed ground was predicted by various models (Plant et al., 1998a). A comparison of the results obtained by the ASAR PSI technique with model-predicted results is shown in Fig. 7.13. The model-predicted ground deformation categories, i.e., the relatively stable state for settlement rate amplitude < 4 mma^{-1}, and the continuous settlement state for settlement rate amplitude > 4 mma^{-1}, are calculated from predicted residual settlement from January 1997 to January 2040, assuming a linear annual settlement rate. The results are marked as shadowed areas with boundaries in black in the Fig. 7.13. The general shape of R1 is similar to the model-predicted unstable area, but covers more area on the east side and less area on the west and north sides. The shapes of R2, R3, and R4 generated by the two methods are almost the same. The relatively stable areas detected by the ASAR PSI

technique, G1, G2, and G3 agree generally with model-predicted results. But the areas of G1 and G3 are a little smaller than the model-predicted areas. Generally speaking, therefore, ASAR PSI-detected annual ground residual settlement rates over HKIA reclaimed foundation agree well with the model-predicted residual settlement rates.

7.9 Summary

The Hong Kong International Airport was built on a site of 12.5 km^2, of which 75% was reclaimed foundation. Thus, the stability of ground foundation of HKIA is of public concern. This study uses the PSI technique and ASAR images taken from 19 April 2006 to 9 January 2008 to detect ground residual settlement rate over HKIA reclaimed foundation. The major results are summarized as follows.

The time series analysis of PSI-detected ground settlement data and simultaneously measured ground truth data at four point targets indicates that the two data sets show the same trends. At two points the ground subsided quite quickly from March 2006 to March 2007, and then became slow. While the other two points show a continuous subsidence trend. Comparison of ASAR PSI-detected ground deformation data with the ground truth data indicates that ASAR PSI-detected annual ground deformation rates systematically underestimate the real ground deformation values. I derived empirical correction models to correct systematic biases existing in the ASAR PSI results.

The corrected ASAR PSI-detected annual ground settlement rate data follow a Lorentz distribution well, implying that the residual settlement process is dominated by

two modes or categories of settlement rates. The first mode or category covered by the first normal distribution represents a relatively stable state with a maximum annual settlement rate smaller than -4 mma^{-1}. The second mode or category covered by the second normal distribution peaked at -10 mma^{-1} represents a continuous settlement state.

I generate a distribution map of the ASAR PSI-detected residual settlement rate over HKIA reclaimed foundation. The map shows that the HKIA reclaimed foundation can generally be divided into sub-areas. The relatively stable sub-areas contain the Passenger Terminal Building area and a major part of the Southern Runway area. The continuous settlement sub-areas are located at the Midfield of the airport, and the western and southern boundaries.

Comparisons of general patterns of ASAR PSI-detected ground settlement rate distribution with model-predicted ground stabilities indicate that generally ASAR PSI-detected annual ground residual settlement rates over HKIA reclaimed foundation agree well with the model-predicted residual settlement rates.

Chapter 8. Conclusions

A ground subsidence of a rate of 1 cma^{-1} may cause serious damages to the buildings, harbors, underground facilities, roads, railways, tunnels, and airport runways. Thus, detecting the ground deformation and clarifying its fundamental laws are everlasting research topics for the human pursuits. In China many cities and municipalities, in particular coastal megacities including Guangzhou and Hong Kong, are suffering disastrous land subsidence. Besides the natural subsidence, including deformation of soft soil, and Karst geomorphologic collapse, human-induced ground subsidence events associated with the rapid development of industrialization and urbanization appear as an increasing trend. Monitoring the land subsidence can not only help people find out the distributions in both spatial and temporal domains, but also guide people minimize the hazard ahead. Thus, it is significant to monitor the ground subsidence accurately, timely and frequently. This dissertation research aims to use ENVISAT ASAR data received at the Chinese University of Hong Kong Satellite Remote

Sensing Receiving Station and InSAR high-tech technology as a powerful tool for large-scale ground deformation monitoring in Guangzhou and Hong Kong areas. The major contributions of this dissertation research are summarized as follows.

8.1. InSAR interpretation method development

Like all measurement technologies, InSAR measurements also contain errors and biases. These errors or biases should be estimated and corrected as possible before using the results in a practical application. Moreover, suitable methods must be developed to extract specified data and information from InSAR products. For my dissertation research, the following InSAR data interpretation methods have been developed.

Time series analysis. In HKIA ground deformation monitoring research, a time series analysis method is used to validate PSI-detected ground settlement data by comparing with simultaneously measured ground truth data. The results indicate that the two data sets show the same trend, and the magnitudes of PSI-detected ground subsidence and the curve slopes are smaller than the ground truth data. This reveals that there are systematic biases in PSI-detected data against the ground truth. These systematic biases are corrected with empirical correlation models developed later.

Correlation analysis and empirical correction equations. I use a correlation analysis method to determine the systematic biases found in comparison of time series data as described above. An ASAR PSI-detected ground deformation rate data set of HKIA from 2006 to 2008 has been validated against field-measured ground deformation

rate data to estimate the accuracy and potential systematic biases. Two linear functions are used to fit the data. From the linear functions, empirical correction equations for the ASAR PSI-detected ground settlement rate are derived and used to correct the ASAR PSI-detected ground settlement rate data set for further analysis.

Statistical analysis. The statistical methods are used to analyze the general distribution features of InSAR-derived ground deformation rate data in HKIA ground deformation monitoring research. A Gaussian distribution or normal distribution is used to fit the data points with a fit goodness of 0.8918. The Gaussian distribution shows that the general statistical trend of ground deformation in HKIA is toward subsidence.

Thematic mapping methods. Great value filtering method is developed and used to generate thematic maps of active subsidence zones in Guangzhou urban area. All the four active subsidence zones are distributed on sedimentation boundaries as shown on the local geological map. These results are consistent with natural characteristics of sedimentation boundaries.

A clustering method groups the ASAR-PSI detected point targets into different categories according to their values or signs, then analyzing their spatial distribution features. In the HKIA case, according to the Gaussian distribution curve of the ground deformation rates, the ground deformation rates are further divided into two categories: Category 1, stable state and Category 2, continuous stable state. A distribution map of the two categories of ground stabilities shows that the Passenger Terminal Building area and

the Southern Runway area are in relatively stable state, and the continuous settlement state PSI points are concentrated at the Midfield of the airport.

InSAR interpretation methods developed in my dissertation research have been applied in large-scale ground deformation monitoring in cases study of Guangzhou and Hong Kong International Airport. The major results have been summarized as follows.

8.2. Ground deformation in Guangzhou

The Interferometric Point Target Analysis (IPTA) technique, a PSI technique, is used to investigate ground deformation in the urban areas of Guangzhou city, which is located at the Pearl River Delta in South China. A time series of ENVISAT ASAR images, taken from 19 March 2007 to 12 May 2008, are used to generate ground deformation fields and interpretation maps. The derived ground subsidence data are then compared with reported ground deformation observation results and analyzed in detail. The mechanisms for causing the ground subsidence in Guangzhou urban area are analyzed. This work is also a demonstration study for evaluating the general performance of the applied PSI technique in detecting ground subsidence with limited SAR images. The major results are concluded as follows:

1) A ground deformation rate map of Guangzhou urban area using scattered distribution of point targets is generated with ASAR images acquired in 2007–2008. The maximum subsidence (rise) rate reaches up to -26 to -20 mma^{-1} (16–21 mma^{-1}). These values are 3–5 times larger than the normal ground deformation rate induced solely by

crustal movement, implying that the study area is an active zone for ground deformation. This agrees with the results obtained by previous investigations.

2) Based on the point target map, a contour ground deformation rate map of Guangzhou urban area is generated by an interpolation method. The horizontal (vertical) resolution of the contour map is ~ 100 m (2 mma^{-1}). The contour map shows three major subsidence zones located in the middle-west, the east, and the southwest of the study area, respectively. The maximum subsidence rate reaches -26 mma^{-1}. Between two subsidence zones, there is always a rise zone with a maximum rise rate up to 21 mma^{-1}. The horizontal scale of the subsidence - rise patterns is about 5 km. All the sites of six ground collapse accidents that occurred in 2007–2008 fall within the subsidence areas, qualitatively validating the IPTA results.

3) Ground subsidence and geological conditions along metro-lines in Datansha Island are examined as a case study. The analysis indicates that the local geological conditions, such as limestone Karst geomorphology, as well as silt layers characterized by high water content, high void ratio, high compressibility, low bearing capacity and low shear strength, are natural causes for ground subsidence and ground collapse accidents occurred there. Human activities in the form of underground engineering projects constitute another important cause.

This study gives the quantitative data of ground deformation in the Guangzhou urban area. Although there are not simultaneous leveling data available for a

point-to-point comparison with IPTA ground deformation measurements, the results of case study of Datansha Island indicate that the IPTA-derived ground subsidence rates qualitatively coincide with field observations of ground collapse events. The contour ground deformation rate map of Guangzhou urban area shows alternately distributed patterns of subsidence and rise zones with a horizontal scale of about 5 km. The patterns seem to indicate that they may be caused by the movement of local geological structure.

8.3. Ground subsidence along geological boundaries

From the ground deformation rate maps of Guangzhou generated by ASAR-PSI technology, the areas with a subsidence greater than 10 mma^{-1}, which are defined as active ground subsidence zones, are extracted using a great value filter. Thematic maps of active subsidence zones are generated and further analyzed.

According to the thematic maps of active subsidence zones, the geological structure, the sediment spatial distribution characteristics, over-development, and underground engineering projects are considered as four major mechanisms for inducing the active subsidence zones. Two obvious active subsidence zones are distributed on the two sides of a geological fault running southwest-northeastward. It indicates that the spatial distribution characteristics of active subsidence zones have a close relationship with the geological fault.

Four active subsidence zones, which are distributed on sedimentation boundaries, are found. This implies that the sedimentation boundaries are active subsidence zones.

The major subsidence sub-zones with the densest distribution of active subsidence points are mainly distributed in the old downtown area. Over-development and sedimentation boundaries are probably the major factors for resulting in the ground subsidence. In the case of Datansha Island, as shown in thematic maps of active subsidence zones, the geological structure and underground engineering projects mainly cause the area to be an active subsidence zone.

Thematic maps generated by combining ASAR-PSI detected ground deformation data with geomorphologic data show that active subsidence zones distribution has close relationships with local geological structures, sediment distribution characteristics, density of buildings, and underground engineering projects. The results can serve as useful information for local development planning and decision making.

8.4. Residual settlement at HKIA

This study uses the PSI technique and ASAR images acquired between 19 April 2006 and 9 January 2008 to detect the ground residual settlement rate over reclaimed foundation of HKIA. The major results are summarized as follows.

The time series analysis of PSI-detected ground settlement data and simultaneously measured ground truth data at four reference point targets indicate that the two data sets show the same trend. At two points the ground subsided quite quickly from March 2006 to March 2007, and then became slow. While the other two points show a continuous subsidence trend. Comparison of ASAR PSI-detected ground deformation data with the

ground truth data indicates that ASAR PSI-detected annual ground deformation rates systematically underestimate the real ground deformation values. I derived empirical correction models to correct systematic biases existing in the ASAR PSI results. I find unreasonable positive values of the ASAR PSI-detected annual ground settlement rate, which follow a normal distribution. Most of the unreasonable points are located at the airport Midfield, which is under construction. These unreasonable values are discarded for further analysis.

The corrected ASAR PSI-detected annual ground settlement rate data follow a Lorentz distribution well, implying that the residual settlement process is dominated by two modes or categories of settlement rates. The first mode or category covered by the first normal distribution represents a relatively stable state with a maximum annual settlement rate smaller than -4 mma^{-1}. The second mode or category covered by the second normal distribution peaked at -10 mma^{-1} represents a continuous settlement state.

I generate a distribution map of the ASAR PSI-detected residual settlement rate over HKIA reclaimed foundation and verified it against the ground truth. The map shows that the HKIA reclaimed foundation can generally be divided into sub-areas. The relatively stable sub-areas contain the Passenger Terminal Building area and a major part of the Southern Runway area. The continuous settlement sub-areas are located at the Midfield of the airport, and the western and southern boundaries.

I compared the general patterns of ASAR PSI-detected ground settlement rate

distribution with model-predicted ground stabilities. It indicates that generally ASAR PSI-detected annual ground residual settlement rates over HKIA reclaimed foundation agree well with the model-predicted residual settlement rates.

For the airports that were built on reclaimed foundations like HKIA, monitoring of ground deformation is a serious problem for the airport safety and flight safety. The results of this study indicate that the ASAR PSI technologies may serve as powerful, high resolution, and cost-efficient tools for routing monitoring of airport ground deformation. The data and information generated by this study may help to assess the status of HKIA ground settlement processes and to predict the trend for future development.

References

Amelung, F., D. Galloway, J. Bell, H. Zebker, and R. Laczniak (1999), "Sensing Las Vegas' ups and downs: InSAR reveals structural control of land subsidence and aquifer-system deformation (abstract)," *Geology (AGU)*, vol. 27, no. 6, pp. 483-486.

Askne, J. and H. Nordius (1987), "Estimation of tropospheric delay for microwaves from surface weather data," *Radio Science*, vol. 22, pp. 379-386.

Baby, H., P. Gole, and J. A. Lavergnat (1988), "Model for tropospheric excess path length of radio waves from surface meteorological measurements," *Radio Science*, vol. 22, pp.1023-1038.

Bock, Y. and C. A. Williams (1997), "Integrated satellite interferometry in southern California," *EOS Transactions AGU*, vol. 78, no. 29, pp. 299-300.

Bonforte, A., A. Ferreti, C. Prati, G. Puglisi, and F. Rocca (2001), "Calibration of atmospheric effects on SAR interferograms by GPS and local atmosphere models: first results," *Journal of Atmosphere and Solar-Terrestrial Physics*, vol. 63, pp. 1-20.

Buckley, S. M., P. A. Rosen, S. Hensley, and B. D. Tapley (2003), "Land subsidence in Houston, Texas, measured by radar interferometry and constrained by extensometers," *Journal of Geophysical Research*, vol. 108, no. B11, pp.2542.

Bürgmann, R., P. A. Rosen, and E. J. Fielding (2000), "Synthetic aperture radar interferometry to measure earth's surface topography and its deformation," *Annual Review of Earth and Planet Sciences*, vol. 28, pp. 169-209.

Bamler, R. and P. Hartl (1998), "Synthetic aperture radar interferometry," *Inverse Problems*, vol. 14, pp. R1-54.

Carnec, C., D. Massonnet, and C. King (1996), "Two examples of the application of SAR

interferometry to sites of small extent," *Geophysical Research Letters*, vol. 23, pp. 3579-3582.

Colesanti, C., A. Ferretti, F. Novali, C. Prati, and F. Rocca (2003), "SAR monitoring of progressive and seasonal ground deformation using the permanent scatterers technique," *IEEE Transactions on Geoscience and Remote Sensing*, vol. 41, no. 7, pp. 1685–1701.

Crosetto, M., C. C. Tscherning, B. Crippa, and M. Castillo (2002), "Subsidence monitoring using SAR interferometry: Reduction of the atmospheric effects using stochastic filtering," *Geophysical Research Letters*, vol. 29, no. 9, pp. 1312.

Crosetto, M., A. Arnaud, J. Duro, E. Biescas, and M. Agudo (2003), "Deformation monitoring using remotely sensed radar interferometric data," in *11th FIG Symposium on Deformation Measurements*, Santorini, Greece, 2003, pp. 1-8.

Crosetto, M., M. Agudo, R. Capes, and S. Marsh (2007a), "GMES Terrafirma: Validation of PSI for users: Results of the Provence inter-comparison," in *Proceedings of the ENVISAT/ERS Symposium*, Montreux, Switzerland, 2007, pp. 1-10 (cdrom).

Crosetto, M., M. Agudo, D. Raucoules, B. Bourgine, M. de Michele, G. Le Cozannet, C. Bremmer, J. G. Veldkamp, D. Tragheim, L. Bateson, and M. Engdahl (2007b), "Validation of Persistent Scatterers Interferometry over a mining test site: Results of the PSIC4 project," in *Proceedings of the ENVISAT/ERS Symposium*, Montreux, Switzerland, pp. 1-9 (cdrom).

Cumming, I. G. and F. H.-C. Wong (2005), *Digital processing of Synthetic Aperture Radar data*, Boston, MA, USA: Artech House, pp. 11-12.

Curlander, J. C. and R. N. McDonough (1991), *Synthetic Aperture Radar Systems and Signal Processing*, 1st edition, Malden, MA, USA: Wiley-Interscience, pp. 1-100.

Cutrona, L. J., W. E. Vivian, E. N. Leith, and G. O. Hall (1961), "A high resolution radar

combat surveillance system," *IRE Transactions on Military Electronics, MIL-5*, pp. 127-131.

Dehls, J. (2006), *Permanent Scatterer InSAR processing: Forsmark*, Swedish Nuclear Fuel and Waste Management Co. (SKB) report 2006, viewed online at http://www.skb.se/upload/publications/pdf/ R-06-56webb.pdf.

Delacourt, C., P. Briole, and J. Achache (1998), "Tropospheric corrections of SAR interferograms with strong topography, Application to Etna," *Geophysical Research Letters*, vol. 25, no. 15, pp. 2849-2852.

Ding, X. L., G. X. Liu, Z. W. Li, Z. L. Li, and Y. Q. Chen (2004), "Ground subsidence monitoring in Hong Kong with satellite SAR interferometry," *Photogrammetric Engineering and Remote Sensing*, 70, 10, pp. 1151-1156.

Elachi, C. (1982), "Radar images of the Earth," *Scientific American*, vol. 271, pp. 54-61.

Elachi, C. (1988), *Spaceborne radar remote sensing: applications and techniques*, New York, USA: IEEE Press, pp. 26, 38-39.

Elachi, C., T. Bicknell, R. L. Jordan, and C. Wu (1982), "Spaceborne Synthetic-Aperture imaging radars: applications, techniques and technology," in *Proceedings of IEEE*, vol. 70, pp. 1174-1209.

Elachi, C., J. B. Cimino, and M. Settle (1986), "Overview of the Shuttle Imaging Radar-B preliminary science results," *Science*, vol. 286, pp. 1511-1516.

Emardson, T. R., M. Simons, and F. H. Webb (2003), "Neutral atmospheric delay in interferometric synthetic aperture radar applications: statistical description and mitigation," *Journal of Geophysical Research*, vol. 108, no. B5, pp. 2231.

European Space Agency, *ASAR Product Handbook*, Issue 1.1 (2002), http://envisat.esa.int/ handbooks/asar/CNTR.htm, pp. 1-543.

Fa, X., and Y. Huang, (1995), "Geological hazard and geological environment in Guangdong province," *Journal of Natural Disasters*, vol. 4, pp. 83–91.

Fang, L. (2005a), "City environment geology problem of Guangzhou," *Earth and Environment*, vol. 33, no. 21, pp. 614-615.

Fang, L. (2005b), "Karst geology in Guangzhou metro, *Earth and Environment*," vol. 33, no. 4, pp. 89–91.

Ferretti, A., C. Prati, and F. Rocca (1999), "Multibaseline InSAR DEM reconstruction: The wavelet approach," *IEEE Transactions on Geoscience and Remote Sensing*, vol. 37, no. 2, pp. 705-715.

Ferretti, A., C. Prati, and F. Rocca (2000), "Nonlinear subsidence rate estimation using permanent scatterers in differential SAR interferometry," *IEEE Transactions On Geoscience and Remote Sensing*, vol. 38, no. 5, pp. 2202-2212.

Ferretti, A., C. Prati, and F. Rocca (2001), "Permanent scatterers in SAR interferometry," *IEEE Transactions On Geoscience and Remote Sensing*, vol. 39, no. 1, pp. 8-20.

Ferretti, A., G. Savio, R. Barzaqhi, A. Borqhi, S. Musazzi, F. Novali, C. Prati, and F. Rocca (2007a), "Submillimeter accuracy of InSAR time series: Experimental validation," *IEEE Transactions on Geoscience and Remote Sensing*, vol. 45, no. 5, pp. 1142-1153.

Ferretti, A., A. Monti-Guarnieri, C. Prati, F. Rocca, and D.Massonnet (2007b), *InSAR principles: Guidelines for SAR Interferometry processing and interpretation*, the Netherlands: *ESA Publications*, pp. 1-135.

Fielding, E. J., R. G. Blom, and R. M. Goldstein (1998), "Rapid subsidence over oil fields measured by SAR," *Geophysical Research Letters*, vol. 25, no. 17, pp. 3215-3218.

Fruneau, B., J. Achache, and C. Delacourt (1996), "Observation and modeling of the Saint-Etienne-de-Tinéé landslide using SAR interferometry," *Tectonophysics*, vol. 265, pp.181-190.

Fu, L.-L. and B. Holt (1982), *Seasat Views Oceans and Sea Ice with Synthetic Aperture Radar,* JPL Publication, pp. 81-120,.

Gabriel, A. K., R. M. Goldstein, and H. A. Zebker (1989), "Mapping small elevation changes over large areas: Differential radar interferometry," *Journal of Geophysical Research*, vol. 94, no. B7, pp. 9183-9191 .

Gamma Remote Sensing, GAMMA Softeware Documentation, (2006), http://www.gamma-rs.ch/gamma.html, pp. 1-16.

Gatelli, F., A. M. Guarnieri, F. Parizzi, P. Pasquali, C. Prati, and F. Rocca (1994), "The wavenumber shift in SAR interferometry," *IEEE Transactions on Geoscience and Remote Sensing*, vol. 32, no. 4, pp. 855-865.

Ge, L., S. Han, and C. Rizos (2000), "The double interpolation and double prediction (DIDP) approach for InSAR and GPS integration," in *19th International Society of Photogrammetry and Remote Sensing Congress & Exhibition*, Amsterdam, Holland, pp. 205-212.

Ge, L., H. Chang, and C. Rizos (2007), "Mine subsidence monitoring using multi-source satellite SAR images," *Photogrammetric engineering and remote sensing*, vol. 73, no. 3, pp. 259-266.

Goldstein, R. M. and H. A. Zebker (1987), "Interferometric radar measurement of ocean

surface currents," *Nature*, vol. 328, pp. 707-709.

Goldstein, R. M. (1995), "Atmopsheric limitations to repeat-track radar interferometry," *Geophysical Research Letters*, vol. 22, no. 18, pp. 1-16.

Graham, L. C. (1974), "Synthetic interferometer radar for topographic mapping," *Proceedings of the IEEE*, vol. 62, pp. 763-768.

Gumen, A. M. and I. G. Kissin (1995), "Hydrogeological effects of contemporaneous crustal movements and their vibroseismic initiation," *Physics of the Solid Earth*, vol. 31, no. 4, pp. 315–324.

Hanssen, R. F. (1998), "Atmospheric heterogeneities in ERS tandem SAR interferometry," *Delft Institute for Earth-Oriented Space Research (DEOS) Rep. No. 98.1*, pp. 1-7.

Hanssen, R. F. (2001), *Radar Interferometry, Data Interpretation and Error Analysis*, 1st edition, Dordrecht, The Netherlands: Kluwer, pp. 1-328.

He, Q., X. Ye, Z. Li, and W. Liu (2006), "The status and prevention strategy of land subsidence in China," *Geological Journal of China Universities*, vol. 12, pp.161–168. (In Chinese)

Holzer, T. L., A. I. Johnson (1985), "Land subsidence caused by ground water withdrawal in urban areas," *GeoJournal*, vol. 11, no. 3, pp. 245-255.

Hooper, A., H. Zebker, P. Segall, and B. Kampes (2004), "A new method for measuring deformation on volcanoes and other natural terrains using InSAR persistent scatterers," *Geophysical Research Letters*, vol. 31, no. 23, pp. 1-5.

Hu, R. L., Z. Q. Yue, L. C. Wang, and S. J. Wang (2004), "Review on current status and challenging issues of land subsidence in China," *Engineering Geology in China*, vol. 76,

no. 2, pp. 65-77.

Hutchinson, M. and M. D. Gibbons (2000), "ENVISAT ASAR-Design & Performance with a view to the future," in *RTO SET Symposium on "Space-Based Observation Technology"*, the Island of Samos, Greece, pp. 1-8.

Jónsson, S. (2002), "Modeling volcano and earthquake deformation from satellite radar, interferometric observations," Ph.D. thesis, Department of Geophysics, Stanford University, Stanford, CA, USA.

Kampes, B. M. (2005), "Displacement parameter estimation using permanent scatterer interferometry," Ph.D. thesis, Delft University of Technology, Delft, The Netherlands.

Kampes, B. M. (2006), *Radar Interferometry: Persistent Scatterer Technique*, 1st edition, Dordrecht, the Netherlands: Springer, pp. 1-211.

Khan, S. A. and H.-G. Scherneck (2003), "The M2 ocean tide loading wave in Alaska: Vertical and horizontal displacements, modeled and observed," *Journal of Geodesy*, vol. 77, no. 3-4, pp. 117-127.

Klees, R. and D. Massonnet (1998), "Deformation measurements using SAR interferometry: Potential and limitations," *Geologie en Mijnbouw*, vol. 77, no. 22, pp. 161-176.

Kovaly, J. (1976), *Synthetic Aperture Radar*, 1st edition, Boston, MA, USA: Artech House, pp.1-360.

Lanari, R., O. Mora, M. Manunta, J. J. Mallorqui, P. Berardino, and E. Sansosti (2004), "A small-baseline approach for investigating deformations on full-resolution differential SAR interferograms," *IEEE Transactions on Geoscience and Remote Sensing*, vol. 42, no. 7, pp. 1377-1386.

Lee, S., K. Kim, and H. Oh (2006), "Ground subsidence hazard analysis in an abandoned underground coal mine area using probabilistic and logistic regression models," in *Geoscience and Remote Sensing Symposium*, Denver, CO, USA, pp. 1549-1552.

Li, F. K., D. N. Held, J. C. Curlander, and C. Wu (1985), "Doppler parameter estimation for spaceborne synthetic aperture radars," *IEEE Transactions on Geoscience and Remote Sensing*, GE-23, pp. 47-56.

Li, Z. (2005), "Correction of Atmospheric Water Vapour Effects on Repeat-Pass SAR Interferometry using GPS, MODIS and MERIS Data," Ph.D. thesis, Department of Geomatic Engineering, University College London.

Liu, G., X. Ding, Y. Chen, Z. Li, and Z. Li (2001), "Ground settlement of Chek Lap Kok Airport, Hong Kong, detected by satellite synthetic aperture radar interferometry," *Chinese Science Bulletin*, vol. 46, no. 21, pp. 1778-1782.

Liu, G. (2003), "Mapping of Earth Deformation with Satellite SAR Interferometry: A Study of Its Accuracy and Reliability Performances," Ph.D. thesis, Department of Land Surveying and Geo-Informatics, The Hong Kong Polytechnic University, Hong Kong, China.

Liu, H., Y. Wang, J. Liu, Y. Ni, J. Wang, and H. Liang (2005), "Cause mechanism and spatiotemporal distribution of major geological disasters in Guangzhou," *Journal of Natural Disasters*, vol. 14, no. 5, pp. 149–153.

Liu, C. (2006), "Engineering geologic problems of Guangzhou metro line 5 and the countermeasures," *Urban Mass Transit*, vol. 7, pp. 37–39.

Liu, J., H. Liu, and W. Liu (2007), "Study on ground collapse risk evaluation in main urban area of Guangzhou city," *Journal of Disaster Prevention and Mitigation Engineering*, vol. 27, no. 4, pp. 487–492.

Lu, Z., R. Fatland, M. Wyss, S. Li, J. Eichelberger, K. Dean, and J. Freymuller (1997), "Deformation of New Trident volcano measured by ERS-1 SAR interferometry, Katmai National Park, Alaska," *Geophysical Research Letters*, vol. 24, pp. 695-698.

Lyons, S., D. Sandwell (2003), "Fault creep along the southern San Andreas from interferometric synthetic aperture radar, permanent scatterers, and stacking," *Journal of Geophysical Research*, vol. 108, no. B1, pp. 2047-2070.

MacDonald, H. C. (1969), "Geologic evaluation of radar imagery from Darien Province, Panama," *Modern Geology*, vol. 1, pp. 1-63.

Madsen, S. N. (1989), "Estimating the Doppler centroid of SAR data," *IEEE Transactions on Aerospace and Electronic Systems*, vol. 25, pp. 134-140.

Mangiarotti, S., A. Cazenave, L. Soudarin, and J. F. Cretaux (2001), "Annual vertical crustal motions predicted from surface mass redistribution and observed by space geodesy," *Journal of Geophysical Research*, vol. 106, no. B3, pp. 4277–4291.

Massonnet, D., M. Rossi, C. Carmona, F. Adragna, G. Peltzer, K. Feigl, and T. Rabaute (1993a), "The displacement field of the Landers earthquake mapped by radar interferometry," *Nature*, vol. 364, pp. 138-142.

Massonnet, D. and T. Rabaute (1993b), "Radar interferometry: limits and potential," *IEEE Transactions on Geoscience and Remote Sensing*, vol. 31, pp. 455-464.

Massonnet, D., and K.L. Feigl (1998), "Radar interferometry and its application to changes in the earth's surface," *Reviews of Geophysics*, vol. 36, pp. 1-60.

Massonnet, D., K. L. Feigl, M. Rossi, and F. Adragna (1994), "Radar inteferometric mapping of deformation in the year after the Landers earthquake," *Nature*, vol. 369, pp. 227-230.

Massonnet, D. and K. L. Feigl (1995a), "Discrimination of geophysical phenomena in satellite radar interferograms," *Geophysical Research Letters*, vol. 22, no. 12, pp. 1537-1540.

Massonnet, D., H. Vadon, and C. Carmona (1995b), "ERS-1 internal clock drift measured by interferometry," *IEEE Transactions on Geoscience and Remote Sensing*, vol. 33, pp. 401-408.

McFadden, T. and C. Siebe (1986), *Cold Regions Engineering*, 1st edition, New York, USA: ASCE Press, pp. 118-133.

Mizouo, M. (1967), "Modes of secular vertical movements of the Earth crust Part 1," *Bulletin of the Earthquake Research Institute*, vol. 45, pp. 1019-1090.

Mora, O., J. J. Mallorqui, and A. Broquetas (2003), "Linear and nonlinear terrain deformation maps from a reduced set of interferometric SAR images," *IEEE Transactions on Geoscience and Remote Sensing*, vol. 41, no. 10, pp. 2243-2253.

Owen, S., P. Segall, J. Freymueller, A. Miklius, R. Denlinger, T. Arandottir, M. Sako, and R. Burgmann (1995), "Rapid deformation of the south flank of Kliauea volcano, Hawaii," *Science*, vol. 267, pp. 1328-1322.

Peltzer, G. and P. Rosen (1995), "Surface displacement of the 17 May 1993 Eureka Valley, California, earthquake observed by SAR interferometry," *Science*, vol. 268, pp. 1333-1336.

Plant, G. W., C. S. Covil, and R. A. Hughes (1998a), *Site Preparation of the New Hong Kong International Airport*, 1st edition, London, UK: Thomas Telford, pp. 1-527.

Plant, G. W. and D. E. Oakervee (1998b), "Hong Kong International Airport: civil engineering design," *Proceedings of the Institution of Civil Engineers*, 126, 1, pp. 15-19.

Poland, J. F. (1984), *Guidebook to studies of land subsidence due to ground water withdrawal*, The United Nations Educational Scientific and Cultural Organization, pp. 1-16.

Price, E. J. and D. T. Sandwell (1998), "Small–scale deformations associated with the 1992 Landers, California, earthquake mapped by InSAR phase gradients," *Journal of Geophysical Research*, vol. 103, no. B11, pp. 27001-27016.

Raucoules, D., B. Bourgine, M. de Michele, G. Le Cozannet, L. Closset, C. Bremmer, H. Veldkamp, D. Tragheim, L. Bateson, M. Crosetto, M. Agudo, and M. Engdahl (2007), Persistent Scatterer Interferometry independent validation and intercomparison of results, available online at http://earth.esa.int/psic4/PSIC4_D9_final_report.pdf.

Rawson, R. and F. Smith (1974), "Four channel Simultaneous X-L Band Imaging SAR Radar," in *9th International Symposium Remote Sensing of Environment*, University of Michigan, Ann Arbor, MI, USA, pp. 251-270.

Rosen, P. A., S. Hensley, H. A. Zebker, F. H. Webb, and E. J. Fielding (1996), "Surface deformation and coherence measurements of Kilauea Volcano, Hawaii, from SIR-C radar interferometry," *Journal of Geophysical Research*, vol. 101, no. E10, pp. 23109-23125.

Rosen, P. A., S. Hensley, I. R. Joughin, F. K. Li, S. N. Madsen, E. Rodriguez, and R. M. Goldstein (2000), "Synthetic aperture radar interferometry," *Proceedings of The IEEE*, vol. 88, no.3, pp.333-382.

Rosenqvist, A., M. Shimada, N. Ito, and M. Watanabe (2007), "ALOS PALSAR: A pathfinder mission for global-scale monitoring of the environment," *IEEE Transactions on Geoscience and Remote Sensing*, vol. 45, no.11, pp. 3307–3316.

Saastamoinen, J. (1972), "Atmospheric correction for the troposphere and stratosphere in

radio ranging of satellites, in Geophysics monograph 15," in *3rd International Symposium, Use of Artificial Satellite for Geodesy, AGU*, Washington DC, pp. 247-251.

Sandwell, D. T. and E. Price (1997), "Sums and differences of interferograms: Imaging the troposphere," *Eos Transactions AGU*, vol. 78, no. 46, pp. F144.

Sandwell, D. T. and E. J. Price (1998), "Phase gradient approach to stacking interferograms," *Journal of Geophysical Research*, vol. 103, no. B12, pp. 30183-30204.

Sherwin, C. W., J. P. Ruina, and R. D. Rawcliffe (1962), "Some Early Developments in Synthetic Aperture Radar Systems," *IRE Transactions on Military Electronics, MIL-6*, pp. 111-115.

Schaber, G. G., C. Elachi, and T. F. Farr (1980), "Remote Sensing of S.P. Mountain and S. P. Lava Flow in North Central Arizona," *Remote Sensing Envionment*, vol. 9, pp. 149-170.

Shimada, M. (2000), "Correction of the satellite's sate vector and the atmospheric excess path delay in SAR Interferometry – Application to surface deformation detection," *International Geoscience and Remote Sensing Symposium*, vol. 5, pp. 2236-2238.

Shimada, M., M. Minamisawa, and O. Isoguchi (2001), "Correction of atmospheric excess path delay appeared in repeat-pass SAR Interferometry using objective analysis data," *International Geosicence and Remote Sensing Symposium*, vol. 5, pp. 2052-2054.

Shimada, M., O. Isoguchi, T. Tadono, R. Higuchi, and K. Isono, "PALSAR CALVAL summary and update (2007)," *IEEE International Geoscience and Remote Sensing Symposium*, Barcelona, Spain, pp. 3593–3596.

Stevens, N.F. (1999), "Lava Flow Volume and Morphology from ERS synthetic Aperture Radar Interferometry," Ph.D. thesis, The University of Reading, Reading, UK, pp. 7-60.

Stephen, M. (2001), *Earth: Portrait of a Planet*, 1st edition, New York, USA: W.W. Northon, pp. 1-880.

Stramondo, S., M. Chini, S. Salvvi, and C. Bignami (2008), "Ground deformation imagery of the May Sichuan earthquake," *EOS Transactions AGU*, vol. 89, pp. 1–2.

Shu, W. (1998), *The New Hong Kong International Airport*, 1st edition, Hong Kong, China: Felix Leung, pp. 1-15.

Teatini, P., M. Ferronato, G. Gambolati, W. Bertoni, and M. Gonella (2005), "A century of land subsidence in Ravenna," *Environmental Geology*, vol. 47, no. 6, pp. 831-846.

The Ministry of Land and Resources (2007), The People's Republic of China, *Bulletin of Chinese Ecological Environment*, pp.1–47.

Wadge, G., P. W. Webley, I. N. James, R. Bingley, A. Dodson, S. Waugh, T. Veneboer, G. Puglisi, M. Mattia, and D. Baker (2002), "Atmospheric models, GPS and InSAR measurements of the tropospheric water vapour field over Mount Etna," *Geophysical Research Letters*, vol. 29, no. 19, pp. 1-4.

Webley, P. W. (2003), "Atmospheric water vapour correction to InSAR surface motion measurements on mountains: Case study on Mount Etna," PhD thesis, The University of Reading, Reading, UK.

Wegmuller, U. and C. Werner (1997), "Retrieval of vegetation parameters with SAR interferometry," *IEEE Transactions on Geoscience and Remote Sensing*, vol. 35, pp. 18-24.

Wegmuller, U. (2003), "Potential of interferometry point target analysis using small data stacks," in *3rd Int. Workshop on ERS SAR Interferometry 'FRINGE03'*, Frascati, Italy, pp.1-3 (cdrom).

Werner, C., U. Wegmuller, T. Strozzi, and A. Wiesmannn (2003), "Interferometric point target analysis for deformation mapping," *IEEE International Geoscience and Remote Sensing Symposium*, Toulouse, France, pp. 1-3 (cdrom).

Wiley, C. A. (1965), "Pulsed Doppler Radar Methods and Apparatus," United States Patent No. 3,196,436, Filed August 1954.

Williams, S., Y. Bock, and P. Pang (1998), "Integrated satellite interferometry: Tropospheric noise, GPS estimates and implications for interferometric synthetic aperture radar products," *Journal of Geophysical Research*, vol. 103, no. B11, pp. 27051-27067.

Wong, F. and I. G. Cumming (1996), "A combined SAR Doppler centroid estimation scheme based upon signal phase," *IEEE Transactions on Geoscience and Remote Sensing*, vol. 34, pp. 696-707.

Xue, Y., Y. Zhang, S. Ye, J. Wu, Z. Wei, Q. Li, and J. Yu (2006), "Research on the problems of land subsidence in China," *Geological Journal of China Universities*, vol. 12, pp. 153–160.

Zebker, H. A. and R. M. Goldstein (1986), "Topographic mapping from interferometric synthetic aperture radar observations," *Journal of Geophysical Research*, vol. 91, pp. 4993-4999.

Zebker, H. A. and J. Villasenor (1992), "Decorrelation in interferometric radar echoes," *IEEE Transactions on Geoscience and Remote Sensing*, vol. 30, pp. 950-959.

Zebker, H. A., P. A. Rosen, R. M. Goldstein, A. Gabriel, and C. L. Werner (1994), "On the derivation of coseismic displacement fields using differential radar interferometry: the Landers earthquake," *Journal of Geophysical Research*, vol. 99, pp. 19617-19634.

Zebker, H. A., P. A. Rosen, and S. Hensley (1997), "Atmospheric effects in

interferometric synthetic aperture radar surface deformation and topographic maps," *Journal of Geophysical Research*, vol. 102, pp. 7547-7563.

Zerbini, S., M. Negusini, C. Romagnoli, F. Domenichini, B. Richter, and D. Simon (2002), "Multi-parameter continuous observations to detect ground deformation and to study environmental variability impacts," *Global and Planetary Change*, vol. 34, pp. 37-58.

Zhang, J. and P. Wei (2003), "Characteristics of the main geological hazards and their control countermeasures in Guangdong province," *The Chinese Journal of Geological Hazard and Control*, vol. 14, no. 4, pp. 44–48. (In Chinese)

Zhang, A. G. and Z. X. Wei (2005), *Land Subsidence in China*, 1st edition, Shanghai, China: Shanghai Science and Technology Press. (In Chinese)

Zhao, Q., H. Lin, L. Jiang, F. Chen, and S. Cheng (2009a), "A study of ground deformation in Guangzhou urban area with Persistent Scatterer Interferometry," *Sensors*, vol. 9, no. 1, pp. 503-518.

Zhao, Q., H. Lin, Y. Zhang, L. Jiang, F. Chen, and S. Cheng (2009b), "Analysis of active ground subsidence zones in Guangzhou city using ASAR Persistent Scatterer Interferometry," in *2009 Urban Remote Sensing Joint Event*, Shanghai, China, pp. 1-5.

Zhao, Q., H. Lin, H. Zebker, A. Chen, Y. Zhang, L. Jiang, and K. Yeung (2009c), "Detection of Residual Settlement of Reclaimed Foundation at Hong Kong International Airport Using InSAR Technology," *IEEE Transactions on Geoscience and Remote Sensing*, Submitted.

Zhi, B., J. Liang, and Y. Lu (2001), *Impacts of soft soils on urban construction in Pearl River Delta economic zone, in: Soft Soil Engineering*, 1st edition, London, UK: Taylor & Francis Group, pp. 3-11.

Zhou, L., H. Tong, and M. Wang (2006), "Study on the engineering properties and suitable treatment methods of Guangzhou soft soil," Journal of Beijing Jiaotong University, vol. 30, no. 1, pp. 17-21. (In Chinese)

Zhou, C., X. Xu, and S. Szeto (2007), "Population distribution and its change in Guangzhou city," *Chinese Geographical Science*, vol. 8, pp. 193-203. (In Chinese)

Zhou, H., Y. Fang, and C. Yu (2009), "Micro-structure observation and an analysis of Guangzhou soft soil during consolidation process," Chinese Journal of Rock Mechanics and Engineering, vol. 28, pp. 3830-3838. (In Chinese)

http://www.fas.org/spp/guide/russia/earth/almaz.htm

http://www2.jpl.nasa.gov/srtm/

http://www.radarsat2.info/about/mission.asp

http://www.telespazio.it/cosmo.html

http://earth.esa.int/applications/data_util/SARDOCS/

http://envisat.esa.int/object/index.cfm?fobjectid=6293

http://esapub.esrin.esa.it/bulletin/bullet102/Desnos102.pdf

http://www.deos.tudelft.nl/ers/precorbs

http://earth.esa.int/services/pg/pgersorbprc.xml

http://envisat.esa.int/dataproducts/asar/CNTR2-9-3.htm

http://en.wikipedia.org/wiki/Guangzhou

http://news.163.com/08/0301/08/45UG8VE700011229.html

http://news.sina.com.cn/o/2008-01-18/144213285387s.shtml

http://news.sohu.com/20071006/n252487281.shtml

http://news.boxun.com/news/gb/misc/2008/01/200801241131.shtml

http://www.gd.xinhuanet.com/dishi/2008-02/02/content_12388671.htm

http://news.sina.com.cn/c/2009-03-18/012017426289.shtml

http://www.gdemo.gov.cn/yjdt/gdyjdt/200811/t20081106_72196.htm

http://gd.nfdaily.cn/content/2009-04/08/content_5046438.htm

Appendix

Ground deformation and collapse accidents field investigation report in Guangzhou urban area

1. Objective

I use IPTA technique and ASAR images to detect ground deformation in the urban area of Guangzhou city as described in Chapter 5 and 6. A ground deformation rate map of Guangzhou urban area with scattered distribution of point targets is generated with ASAR images acquired in 2007–2008. The maximum subsidence (rise) rate reaches up to -26 to -20 mma^{-1} (16–21 mma^{-1}). These values are 3–5 times larger than the normal ground deformation rate induced solely by crustal movement, implying that the study area is an active zone for ground deformation. The analysis of ground subsidence and geological conditions along metro-lines in Datansha Island indicates that the local geological conditions, such as limestone Karst geomorphology, as well as silt layers characterized by high water content, high void ratio, high compressibility, low bearing capacity and low shear strength, are natural causes for ground subsidence and ground collapse accidents occurring there.

Based on the ground deformation rate maps of the urban area of Guangzhou city, a series thematic map of the active ground subsidence zones are generated to interpret the distribution of active ground subsidence zones. The results show that geological faults, rock distribution, over-development, and underground engineering projects may be four

factors leading to the distribution of the active ground subsidence zones in the study (*Zhao, et al., 2009b*).

Field investigation of geological condition of urban area of Guangzhou city was conducted in March 2009. I mainly investigated the buildings along subway lines which are under-constructing in Yuexiu district. Datansha Island is another major investigation site where 5 ground collapse accidents occurred along the metro line 5 and 6 during 2007 to 2008. My investigation results indicate that geological faults, rock distribution, over-development, and underground engineering projects may be four factors leading to the distribution of the active ground subsidence zones.

2. Duration of field trip

3 days, Mar 27 – 29, 2009.

3. Accompanied by

Prof. ZHANG, yuanzhi

Prof. WANG, Yunpeng (Guangzhou Institute of Geochemistry, Chinese Academy of Sciences)

Prof. Bernard de JONG (Utrecht university)

WANG, Shengxiao

4. Facilities for field investigations

Camera, GPS receiver, Guangzou geological map, Guangzhou map, ASAR-PSI interpretation maps, pens, notebook, cellulose tape, sign pen, sampling bag and files.

5. Investigation contents

Sedimentation boundaries. Four active ground subsidence zones distributed on sedimentation boundaries are found according to the active ground subsidence zones of PSI detected point targets in Guangzhou city. I conducted field investigation at one of the four active ground subsidence zones which is located in the north side of the Pearl River. This active ground subsidence zone is located in Yuexiu district. It is shown in a red rectangle of Fig. 1.

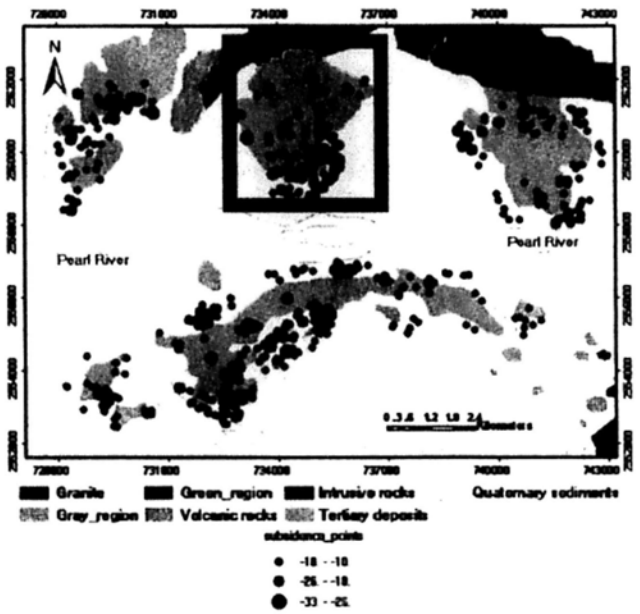

Figure 1. Interpretation map of the relationship between active subsidence zones and the sedimentation boundaries (*Zhao, et al., 2009b*).

Tertiary deposits

Quaternary sediments

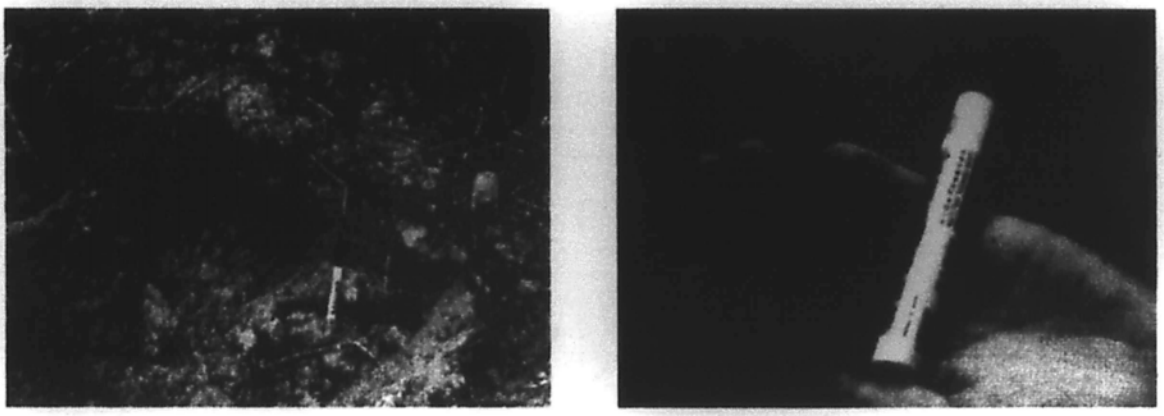

Figure 2. Soil samplings near active subsidence zones.

I sampled two kinds of sediments near active subsidence zones shown in Fig. 2. One is Tertiary deposits, another is Quaternary sediments. The two kinds of sediments are different from water content, void ratio, compressibility, bearing capacity and shear strength.

Underground engineering projects. The spatial distribution of main ground collapse accidents occurring from 2007 to 2009 is shown in Fig. 3. These accidents are mainly distributed along the underground metro-lines around Datansha Island. Table 1 is the ground collapse accidents.

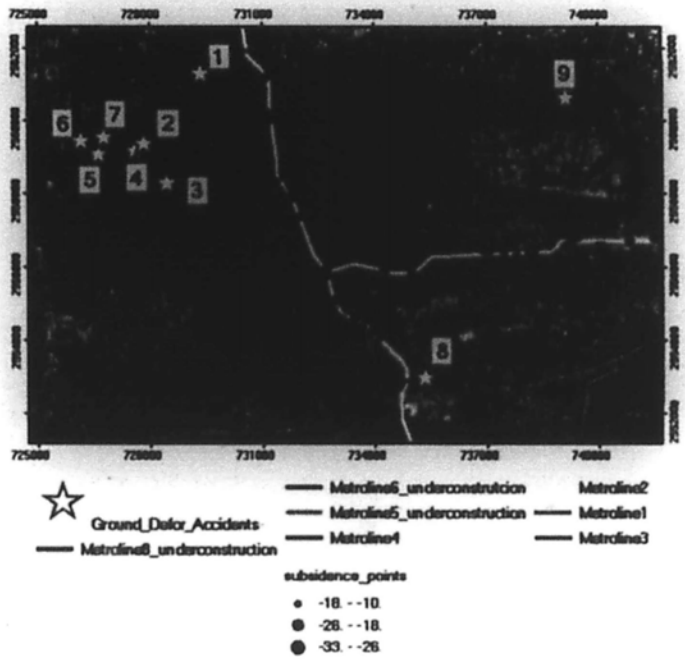

Figure 3. Interpretation map of the relationship between active ground subsidence zones and underground engineering projects (*Zhao, et al., 2009a*).

Table 1. Ground collapse accidents in Guangzhou in 2007-2009 coded from 1 to 9 in Fig. 6.4 (partially referred to (*Zhao, et al., 2009a*)).

Code	Occurrence time	Location	Scope, x×y×z	DR* mma^{-1}
1	Feb 29, 2008	Huanshixi Road, Liwan	3m x 1.5m x 3m	-15 - -10
2	Jan 31, 2008	Zhongshanba Road	small scope 30cm deep	-15 - -10
3	Oct 06, 2007	Duobao Road	300 m^2, ~ 6m deep	-20 - -15
4	Feb 18, 2008	Juncture of	100m^2,	-20 - -15

Code	Occurrence time	Location	Scope, x×y×z	DR* mma^{-1}
		Zhongshanba Rd. Nanan Rd and Huangsha Av, Liwan	deepest site: over 40m	
5	Jan 23-24, 2008	Datansha Island	200-300m^2, >3m deep	-15 - -10
6	Feb 02, 2008	Datansha Island	Observable	-15 - -10
7	Nov 04, 2008	Datansha Island	500 m^2, 100m x 0.2m x 1m	-20 - -15
8	Feb 17, 2009	Juncture of Nanzhou Rd and South Dongxiao Rd, Haizhu	Observable	-15 - -10
9	Mar 04, 2009	Keji Rd, Tianhe	Observable	-15 - -10

Photos (shown in Fig. 4) were taken at the site of ground collapse accident 1. The photos show that the metro-line was under-construction (metro line 5). In Fig. 3, dozens of point targets with great subsidence value (greater than 10 mma^{-1}) are found here.

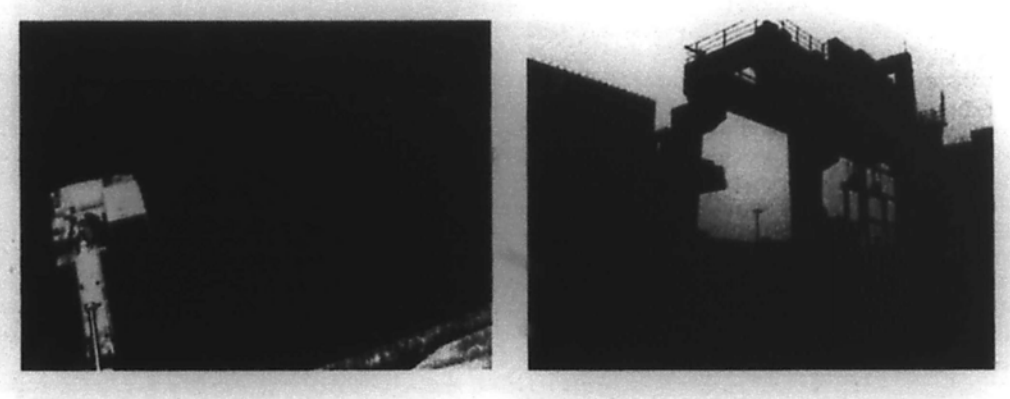

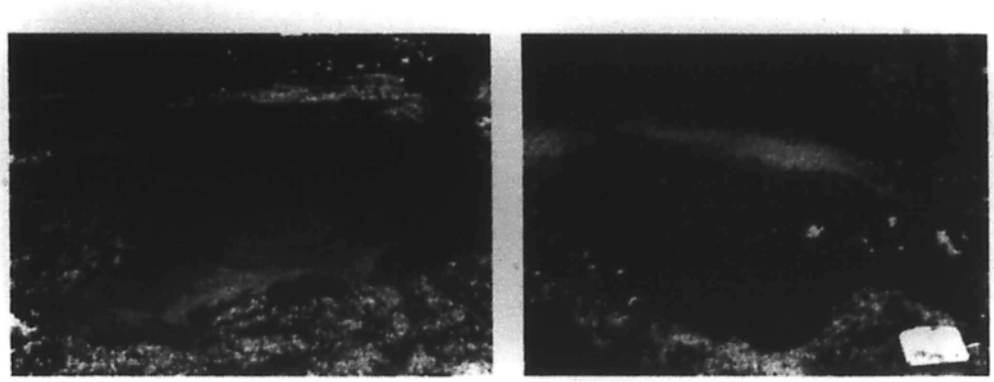

Figure 4. Photos of the site at ground collapse accident 1.

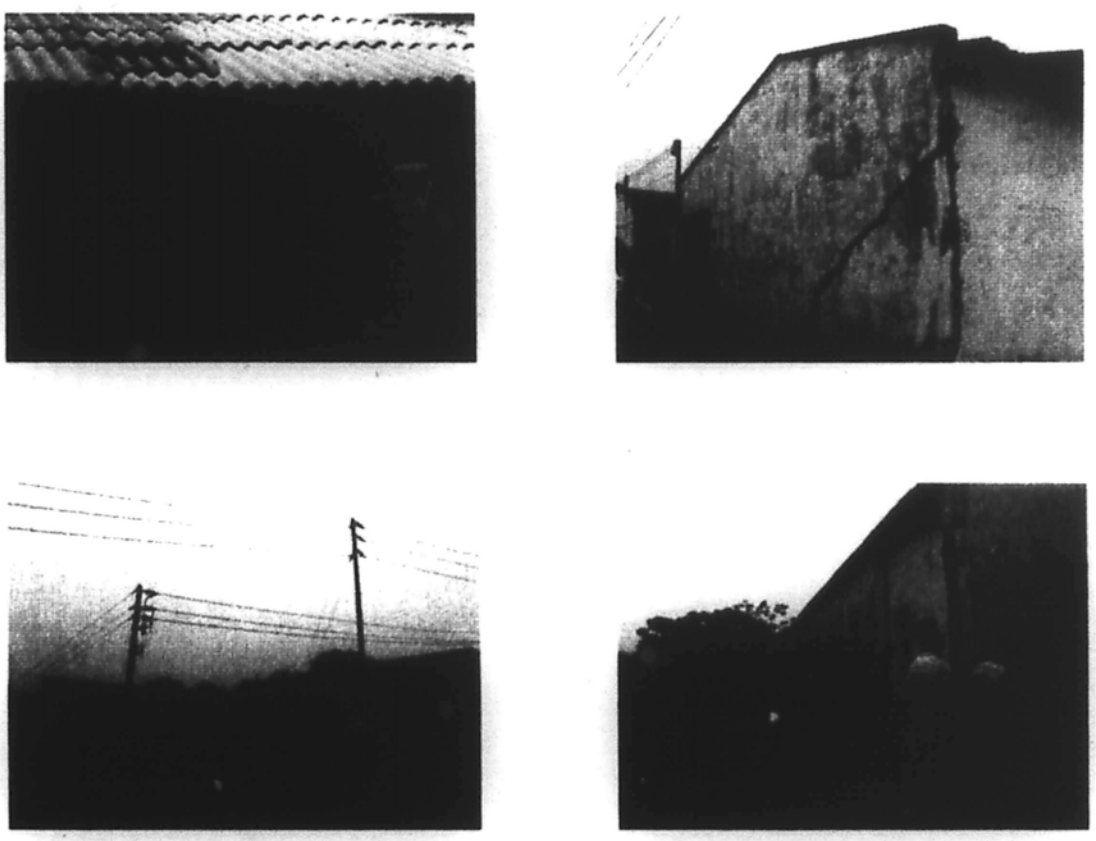

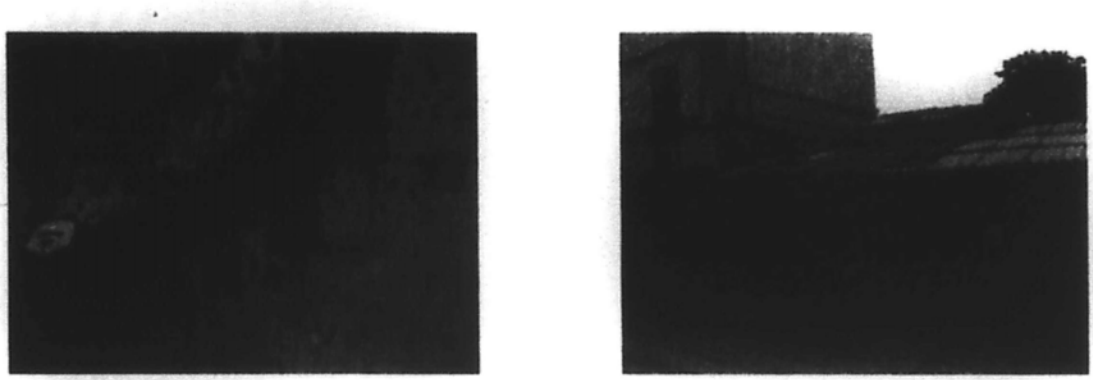

Figure 5. Photos of the site at ground collapse accident 5 and 6.

Photos (shown in Fig. 5) were taken at the site of ground collapse accident 5 and 6. The photos show destroys caused by ground collapse accidents. In Fig. 3, dozens of point targets with great subsidence value (greater than 10 mma^{-1}) are found here.

Subsidence in old downtown. Fig. 6 shows that the active ground subsidence points are mainly distributed in old downtown area. The active ground subsidence zone is in Yuexiu district. Yuexiu district is one of the oldest urban areas in Guangzhou. It is also a traditional commercial centre of Guangzhou city. By the end of 1994, the population density of Yuexiu district has reached to 52.1 thousand/sq km (*Zhou, et al., 2007*). It was the most dentist district.

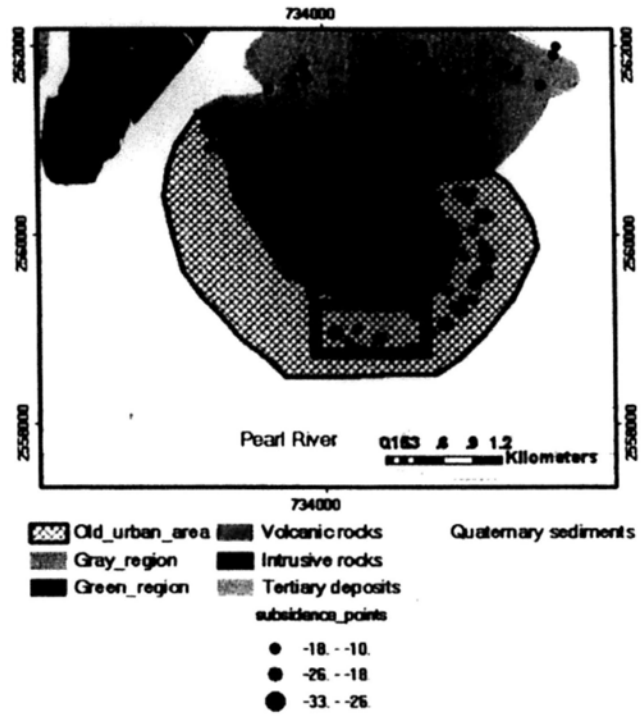

Figure 6. Interpretation map of the relationship between active ground subsidence zones and downtown area (*Zhao, et al., 2009a*).

With the instant development of Yuexiu district, lots of high skyscraper and underground project (shown in Fig. 7) have been constructed or are under-construction. The picture on the right of Fig. 7 shows an entrance of an underground shopping centre. The construction of the underground project was almost finished at that time.

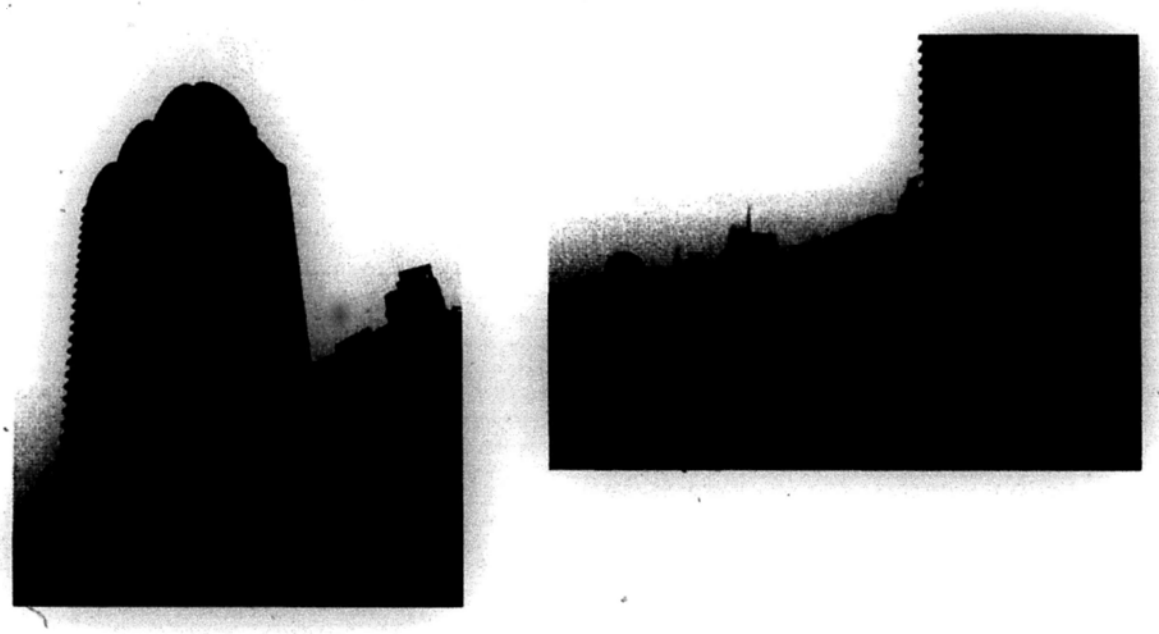

Figure 7. Photos of Yuexiu district.

6. Summary

Based on the ground deformation rate map of the study area, thematic maps of the active ground subsidence zones, and a local geological map of Guangzhou urban area, I conducted a field investigation on ground collapse accidents occurred in Yuexiu and Liwan District of the Guangzhou urban area to interpret the distribution of active ground subsidence zones and related causing factors. Sedimentation boundaries, underground engineering projects, and subsidence in the old downtown, may be major causing factors. Our validation results indicate that the active subsidence zones have close relationship with the causing factors.